First Extraction of the Matter Radius of ^{132}Sn via Proton Elastic Scattering at 200 MeV/nucleon

Yuto Hijikata

Doctoral Dissertation

Department of Physics
Kyoto University

Abstract

The nuclear matter equation of state (EOS) is crucial not only for describing the basic properties of nuclear matter but also for revealing astrophysical phenomena such as the structure of neutronstars and supernova explosions. However, the symmetry energy term in the EOS includes a large uncertainty, especially in the density slope parameter L. The L parameter has a strong correlation with a neutron skin thickness of neutron-rich heavy nuclei. Particularly, ^{132}Sn is highly attractive since it is a doubly magic nucleus and has a larger isospin asymmetry than ^{208}Pb, which will provide a significant insight into the symmetry energy. However, measuring the skin thickness of ^{132}Sn is challenging due to its instability.

To investigate the structure of ^{132}Sn, we performed, for the first time, proton elastic scattering at 196–210 MeV/nucleon at Radio Isotope Beam Factory (RIBF) in RIKEN. Although precise measurement of cross sections of proton elastic scattering over a wide momentum-transfer range can provide accurate density distributions, the experiments had not been conducted due to experimental difficulties in inverse kinematics, such as achieving high excitation-energy resolution and sufficient statistics. To overcome these challenges, we have developed a new beam particle identification method using diamond detectors and low-pressure multi-wire drift chambers (MWDCs), enabling the use of high-intensity beams. In addition, we constructed a solid hydrogen target and a recoil proton detection system, consisting of MWDCs, plastic scintillators, and NaI(Tl) calorimeters. As a result, we successfully measured the cross sections over a momentum-transfer range of 0.80 to 2.1 fm^{-1}.

To deduce the density distributions of ^{132}Sn, we analyzed the experimental data using the relativistic impulse approximation (RIA) calculation with relativistic Love-Franey nucleon-nucleon interactions. The interaction is tuned to reproduce proton elastic scattering data from ^{58}Ni. Using the RIA calculation, we extracted the proton and neutron density distributions in the form of a two-parameter Fermi shape. The extracted densities give a root-mean-square matter radius $\langle r_m^2 \rangle^{1/2} = 4.758^{+0.023}_{-0.024}\,\mathrm{fm}$ and a neutron skin thickness $\Delta r_{np} = 0.178^{+0.037}_{-0.050}\,\mathrm{fm}$.

The obtained cross sections, matter radius, and neutron skin thickness were compared with the state-of-the-art *ab initio* calculations using the in-medium similarity renormalization group method with chiral EFT interactions. The angular distributions and matter radius of the calculation using the $\Delta\mathrm{NNLO_{GO}}$ interaction are most consistent with the experimental results. However, a combined analysis with the charge radius measured by laser spectroscopy reveals that no theoretical calculations, including the *ab initio* and mean-field calculations, can reproduce both charge and matter radii simultaneously. From the viewpoint of isotopic systematics, we found that the matter radius at the magic number $N = 82$ shows a noticeable shrinkage compared with the mean-field calculations, similar to the trend observed in Ca isotopes.

It is well established that the neutron skin thickness of the ^{132}Sn has a strong correlation with the slope parameter of the symmetry energy L, according to predictions by various mean-field models. Using the linear correlation, our result of the neutron skin thickness leads to a relatively smaller L value of $L = 12.0^{+24.3}_{-32.5}$ MeV than those by previous works.

Contents

Chapter 1

Introduction

1.1 Nuclear matter equation of state

The nuclear matter equation of state (EOS) is one of the most fundamental properties of nuclear matter. In the EOS, the binding energy per nucleon E can be expressed as

$$E(\rho,\delta) = E(\rho,0) + S(\rho)\delta^2 + O(\delta^4), \tag{1.1}$$

where $\rho = \rho_n + \rho_p$ is baryon density and $\delta = (\rho_n - \rho_p)/\rho$ is isospin asymmery with neutron density ρ_n and proton density ρ_p. The $E_0(\rho) \equiv E(\rho,0)$ is the binding energy of the isospin symmetric nuclear matter, and the $S(\rho)$ is the so-called symmetry energy. There are no odd-order terms because of the assumption of isospin symmetry in nuclear forces.

The EOS of the symmetric nuclear matter $E_0(\rho)$ can be expressed around the nuclear saturation density ρ_0 as

$$E_0(\rho) = E_{\mathrm{sat}} + \frac{K_0}{2}\epsilon^2 + \frac{K_0}{6}\epsilon^3, \tag{1.2}$$

$$K_0 = 9\rho_0^2 \frac{\partial^2 E_0(\rho)}{\partial^2 \rho}\bigg|_{\rho=\rho_0}, \tag{1.3}$$

where $\epsilon \equiv (\rho - \rho_0)/3\rho_0$. The binding energy at the saturation density E_{sat} is known to be $\approx 16\,\mathrm{MeV}$. The K_0 is the so-called incomprehensibility of symmetric nuclear matter, which is well known to have a strong correlation with the isoscalar giant monopole resonance (ISGMR). For instance, K_0 has been constrained to $240 \pm 20\,\mathrm{MeV}$ by the ISGMR of ^{208}Pb [1]. Figure 1.1 shows the typical predictions for the EOS of the symmetric nuclear matter ($\delta = 0$) and pure neutron matter ($\delta = 1$) based on the microscopic *ab initio* calculations and phenomenological approaches.

1.2 Symmetry energy and neutron skin thickness

The symmetry energy $S(\rho)$ characterizes asymmetric nuclear matter and is essential for understanding astrophysical phenomena such as neutron-star structure, supernova explosions, and neutron-star mergers. The landmark observation of a gravitational wave from

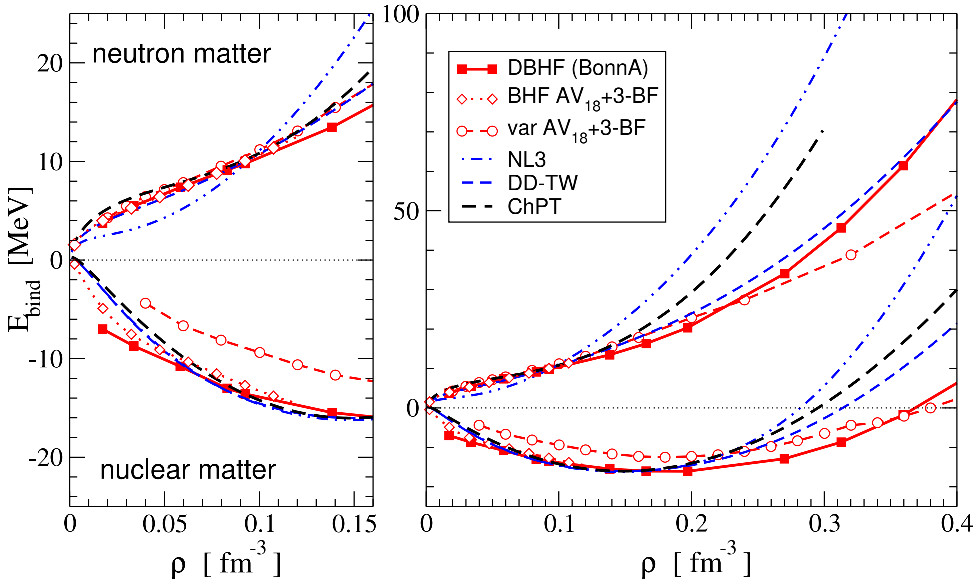

Figure 1.1: EOS of nuclear matter and pure neutron matter calculated by the Dirac-Buuckner-Hartree-Fock using Born A interaction, non-relativistic Buuckner-Hartree-Fock and various calculations using AV_{18} interaction with three-body forces, relativistic mean-field functionals NL3 and DD-TW, and chiral-perturbation theory ChPT. Taken from [2].

the neutron-star merger by the LIGO and VIRGO collaborations in 2017 (GW170817) further emphasized its importance [3]. $S(\rho)$ can be expressed around the saturation density ρ_0 as

$$S(\rho) = J + L\epsilon + \frac{K_{\mathrm{sym}}}{2}\epsilon^2 + O(\epsilon^3), \tag{1.4}$$

$$J = S(\rho_0), \tag{1.5}$$

$$L = 3\rho_0 \left.\frac{\partial S(\rho)}{\partial \rho}\right|_{\rho=\rho_0}, \tag{1.6}$$

$$K_{\mathrm{sym}} = 9\rho_0^2 \left.\frac{\partial^2 S(\rho)}{\partial^2 \rho}\right|_{\rho=\rho_0}. \tag{1.7}$$

The L and K_{sym} are the slope and curvature parameters of the symmetry energy at the saturation density $\rho = \rho_0$, respectively. The L and K_{sym} are related to K_τ as $K_\tau \simeq K_{\mathrm{sym}} - 6L$, where K_τ is an isospin-dependent term of nuclear matter incompressiblity K_A as

$$K_A = K_0 + K_\tau \delta^2 + O(\delta^4). \tag{1.8}$$

The K_τ is investigated by the isotopic dependence of the ISGMR energies of nuclei [1]. The J and L have been investigated by many nuclear physics experiments, such as measurements of masses, isospin diffusions, isovector resonances, isobaric-analog-state energies, and neutron skin thickness. These parameters also have a very strong correlation with the properties of neutron stars, and therefore, they have also been constrained by astrophysical observations. One of the summary works provides the averaged values of $J = 31.7 \pm 3.2\,\mathrm{MeV}$ and $L = 58.7 \pm 28.1\,\mathrm{MeV}$ for both terrestrial experiments and astrophysical observations [4], as shown by Fig. 1.2. The values of L show a broad distribution and depend sensitively on the observables and experimental methods employed.

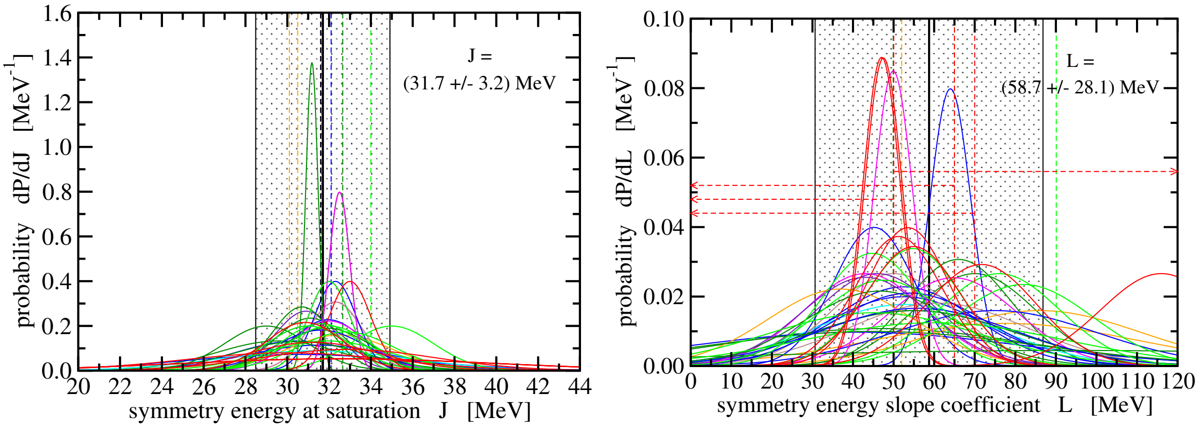

(a) Symmetry energies at saturation J.

(b) Symmetry energy slope parameter L.

Figure 1.2: Probability distributions of the symmetry energy parameters from various studies. Taken from Ref. [4].

One of the most important methods to constrain the L parameter is a measurement of the neutron skin thickness Δr_{np} on the neutron-rich nuclei, especially those that have double magicities. The neutron skin thickness is defined as

$$\Delta r_{np} = r_n - r_p, \tag{1.9}$$

where $r_{n(p)} = \langle r^2_{n(p)} \rangle^{1/2}$ is a root-mean-square (rms) radius of neutron (proton). Both non-relativistic and relativistic mean-field calculations suggest that neutron skin thicknesses of the doubly magic nuclei have strong correlations with the symmetry energy parameters, especially L, as shown in Figs. 1.3 and 1.4.

^{208}Pb is the heaviest stable nucleus with doubly magic numbers. Since its neutron skin thickness is known to have a particularly strong correlation with the symmetry energy parameters, the density and radius have been studied using various probes, such as parity-violating electron scattering [7, 8], isovector giant dipole resonance by inelastic α scattering [9], dipole polarizability α_D measurements [10], pygmy dipole resonance (PDR) [11], antiprotonic atoms [12, 13, 14], Pion photoproduction [15], and proton elastic scattering [16, 17, 18]. The extracted skin thicknesses by several studies are summarized in Table 1.1 and widely spread. Since the uncertainties in the results, including the model errors, are not insignificant, strong constraints cannot be placed on the L parameter.

In such situations, the neutron skin thicknesses of unstable nuclei, especially double magic nuclei such as ^{132}Sn, ^{52,54}Ca, have attracted considerable attention, because they are known to be more strongly correlated with the L parameter than those of stable nuclei.

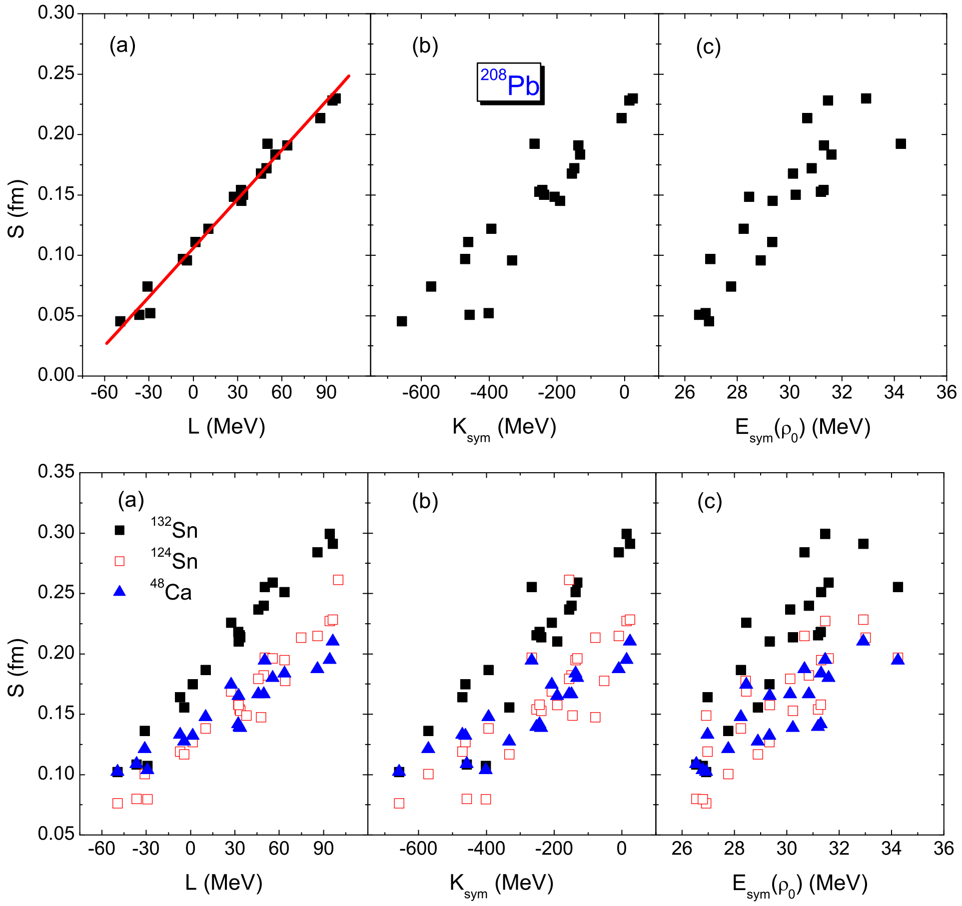

Figure 1.3: Neutron skin thickness $S = \Delta r_{np}$ of ^{208}Pb, ^{124,132}Sn, and ^{48}Ca as a function of (a) L, (b) $K_{\rm sym}$, and (c) $E_{\rm sym}(\rho_0) = J$ for 21 sets of Skyrome interaction parameters. Taken from Ref. [5].

Table 1.1: Experimental values of neutron skin thickness Δr_{np} of ^{208}Pb with indications whether model uncertainties are included.

Experiment	Δr_{np} of ^{208}Pb [fm]	model error
^{208}Pb(p,p) [18]	$0.211^{+0.054}_{-0.063}$	○
PREX-II [8]	0.283(71)	○
α_D [10]	$0.156^{+0.025}_{-0.021}$	×
PDR [11]	0.180(35)	×
$\bar{p}$-atom X-ray I [13]	$0.16(2)_{\rm stat}(4)_{\rm syst}$	○
$\bar{p}$-atom X-ray II [14]	$0.20(4)_{\rm exp}(5)_{\rm mdl}$	○
Coherent π^0 photoprodocution [15]	$0.15^{+0.03}_{-0.04}$	×

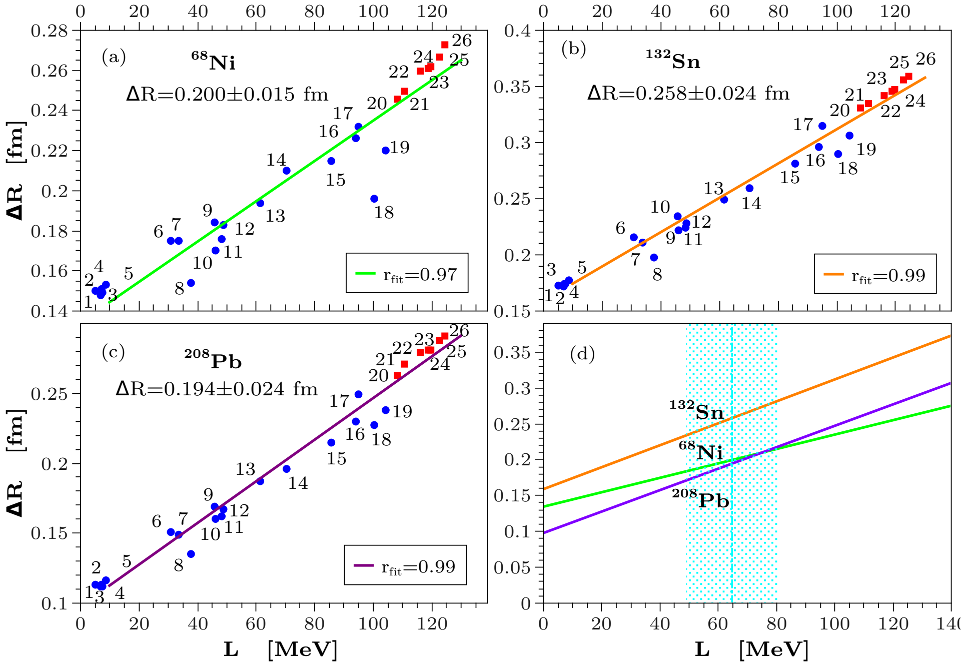

Figure 1.4: Correlations between the neutron skin thickness and the slope parameter L. The blue and red points are Skyrme Hartree-Fock and relativistic mean-field calculations, respectively. Taken from Ref. [6].

Although the neutron numbers of ^{52,54}Ca are not magic numbers found in stable nuclei, evidence of their double magicities has been reported [19, 20]. Measuring the neutron skin thickness of them with a precision comparable to that achieved for stable nuclei would enable tighter constraints on the symmetry energy parameters.

Beyond neutron skin thickness

Conventionally, the EOS properties have been studied mainly through mean-field calculations. Within this framework, however, it is difficult to identify correlations across different models between the symmetry energy parameters and proton or neutron radii. The neutron skin thickness has remained almost the only observable that provides meaningful constraints on the symmetry energy. However, since the neutron skin thickness is a very small quantity, its precise extraction is challenging.

To address this, efforts have focused on extending the measurements to systems with large isospin asymmetry, where the larger skin thicknesses are expected. In parallel, new approaches have been developed to probe the EOS parameters through alternative parameters.

One such approach is the comparison with *ab initio* calculations starting from chiral effective theory (EFT). Thanks to remarkable progress in theoretical approaches and computational technologies, *ab initio* calculations have become applicable to heavy nuclei, including ^{132}Sn and ^{208}Pb. These advances enable a direct examination of nuclear forces derived from chiral EFT through measurements of the size of heavy nuclei. Consequently, measurements of charge radii and matter radii have become highly valuable, extending beyond the traditional reliance on neutron skin thickness alone.

Furthermore, instead of reducing measured density distributions merely to radii, new methods have been developed to extract alternative physical quantities from the distributions. One approach is a two-dimensional (2D) plotting method of isoscalar (IS) density $\rho_{\rm IS}$ and isovector (IV) density $\rho_{\rm IV}$ [21]. Another one is proton density polarization, which is the change in proton distribution induced by excess neutrons in isotopes [22].

The IS and IV densities are defined as

$$\rho_{\rm IS}(r) \equiv \rho_n(r) + \rho_p(r), \tag{1.10}$$

$$\rho_{\rm IV}(r) \equiv \rho_n(r) - \rho_p(r). \tag{1.11}$$

Figure 1.5 present a 2D plot of IS and IV densities of ^{208}Pb. The black curve shows the experimental trajectory, while the colored curves are Skyrme Hartree-Fock (SHF) calculations with SAMi-J families [23]. The dashed line corresponds to the constant asymmetry limit $\rho_{\rm IV} = \rho_{\rm IS}(N-Z)/A$ of the asymmetric nuclear matter. It is noticed that the slopes of the trajectories at the crossing points with the constant asymmetry line have strong correlations with the symmetry energy parameters. For instance, Fig. 1.6 shows the correlation between the L parameter and extracted slopes. By using the correlation for the SHF calculations with SAMi-J parameters and the relativistic mean-field (RMF) calculations with DDME-J parameters, the L value is deduced as

$$L = \begin{cases} 29.5 \pm 6.4\,\mathrm{MeV} \ \text{(SAMi-J)} \\ 36.9 \pm 5.2\,\mathrm{MeV} \ \text{(DDME-J)} \end{cases}. \tag{1.12}$$

Although caution regarding model dependence is required and further investigation will be necessary, the uncertainty is considerably smaller than that obtained through neutron skin thickness, demonstrating the usefulness of this new method.

The proton density polarization (PDP) has recently been proposed as a quantity correlated with the symmetry energy parameters J and L. In Ref. [22], PDP was discussed in the context of the change for ^{48}Ca caused by the eight excess neutrons added to ^{40}Ca. Figure 1.7 shows the difference in $4\pi r^2 \rho_{n(p)}$ between ^{40}Ca and ^{48}Ca calculated with the SAMi-J and DDME-J families [23]. Although the proton number itself does not change, it is found that the proton density distribution is modified by the attraction of the eight additional neutrons. The ratio R of the peak values between the neutron density difference and the proton one exhibits clear correlations with the symmetry energy parameters. Figure 1.8 shows the correlations with L. Since Sn has a longer isotopic chain than Ca, PDP in the Sn isotope is expected to exhibit a stronger correlation with the symmetry energy parameters. This highlights the importance of measuring density distributions of both neutron-rich and proton-rich side Sn isotopes.

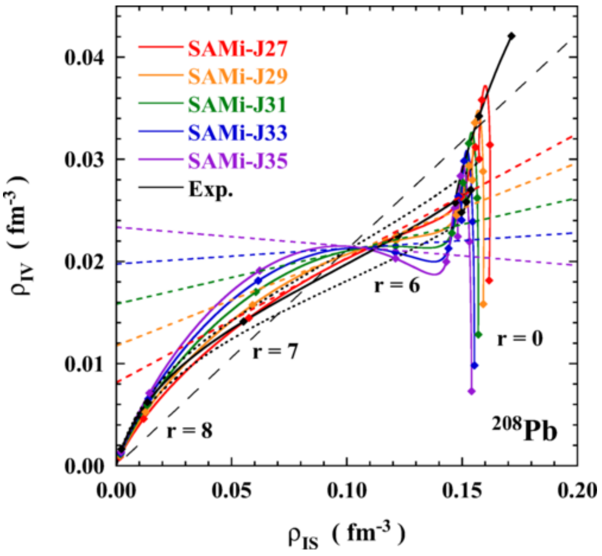

Figure 1.5: Trajectory in a 2D plot of IS and IV densities of ^{208}Pb. The experimental trajectory is given by the black solid curve sandwiched between two dotted lines. The area between the two dotted lines shows the experimental uncertainties. The black solid curve gives the experimental trajectory. The dashed line corresponds to the constant IV density limit $\rho_{\rm IV} = \rho_{\rm IV}(N-Z)/A$. The colored solid curves are calculations with the SAMi-J families [23]. The slopes, shown by the colored dashed lines, are evaluated at the crossing points with the constant IV trajectory. Taken from Ref. [21].

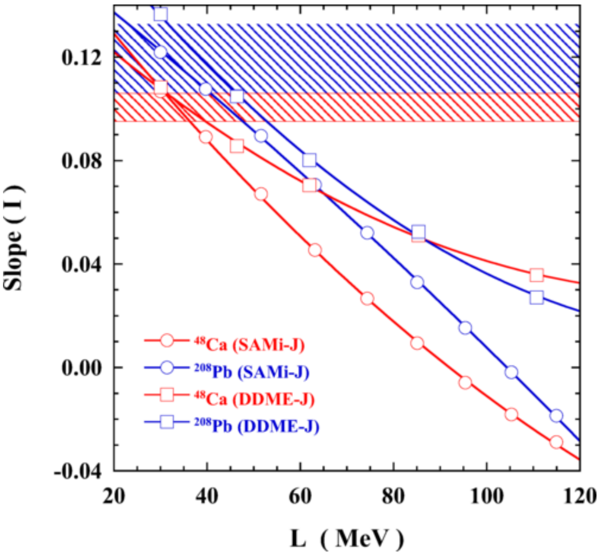

Figure 1.6: Correlation between the symmetry energy parameter L and the slope of the IS-IV density curve. The shaded areas show experimental slopes obtained for ^{48}Ca and ^{208}Pb. The experimental results of ^{48}Ca and ^{208}Pb are taken from Ref. [24] and Ref. [18], respectively. Taken from Ref. [21].

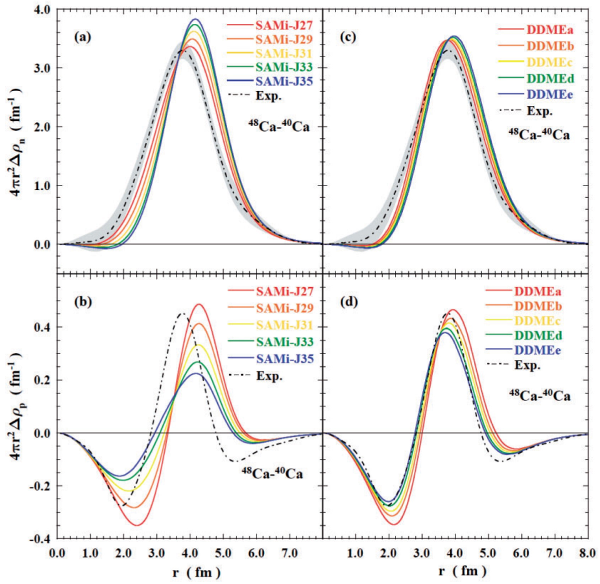

Figure 1.7: Neutron and proton density differences between ^{40}Ca and ^{48}Ca. (a) Neutron with the SAMi-J family, (b) the same for proton, (c) neutron with the DDME-J family, and (d) the same for proton. Taken from Ref. [22].

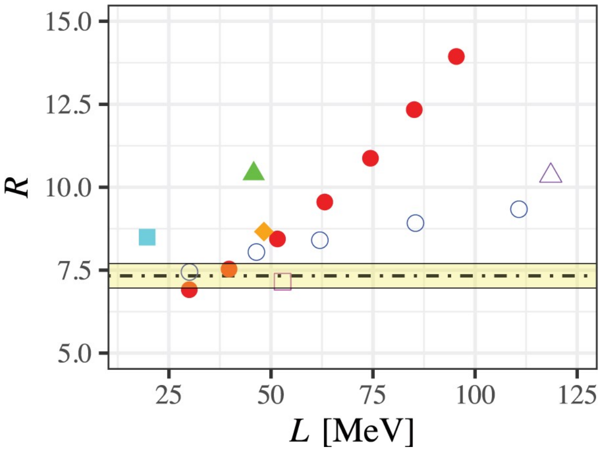

Figure 1.8: Correlations between the PDP peak ratio R and symmetry energy parameter L. Each point shows an SHF or RMF calculation. The yellow band shows the experimental value [24]. Taken from Ref. [22].

1.3 Nucleon density distributions of the stable nuclei

The nucleon density distribution is one of the most fundamental properties of nuclei. Because the neutron-skin thickness is strongly correlated with the nuclear matter EOS, as discussed in the previous section, determining both proton and neutron density distributions is of great importance. However, measuring neutron distributions is particularly challenging and remains the focus of considerable ongoing efforts.

1.3.1 Proton and charge density distributions of the stable nuclei

The proton density distribution ρ_p can be obtained by unfolding the charge density distribution ρ_{ch} with the proton's intrinsic charge distribution. Since the pioneering experiment by Hofstader *et al.* [25], charge distributions of various stable nuclei have been investigated through the electron scattering experiments [26]. The rms charge radii $r_{ch} = \langle r_{ch}^2 \rangle^{1/2}$ have also been accurately determined using isotope shifts by laser spectroscopy and muonic atom X-rays, in addition to the electron scattering [27]. Thanks to its clean reaction mechanism, the electromagnetic probe provides reliable access to extract charge distributions, including information about the internal nuclear structure.

1.3.2 Neutron density distributions of the stable nuclei

It is more challenging to extract neutron density distributions than those for proton density distributions, since electromagnetic probes are insensitive to neutrons. A major alternative approach is parity-violating electron scattering, which probes the weak charge of nucleons [7, 8, 28]. This technique is highly sensitive to neutron distributions because the weak charge of the neutron (≈ -0.99) is significantly larger than that of the proton (≈ 0.07). An important advantage of this method is cleanliness and model independence. Notable examples are the ^{208}Pb radius experiment (PREX) [7], PREX-II [8], and the ^{48}Ca radius experiment (CREX) [28] at the Jefferson Laboratory (JLab). However, a key limitation of the weak probe is its low statistical yield, which restricts measurements to a single momentum transfer and results in large statistical uncertainties. Moreover, the neutron skin thicknesses of ^{48}Ca and ^{208}Pb extracted from CREX and PREX are mutually inconsistent within conventional mean-field theories, as shown in Fig. 1.9.

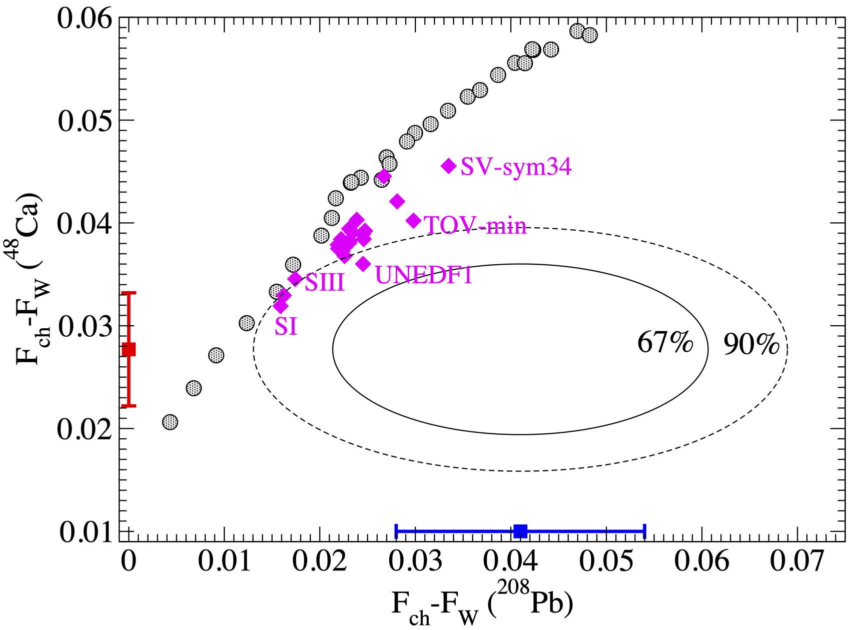

Figure 1.9: Difference between the charge and weak form factors of ^{48}Ca versus that of ^{208}Pb at their respective momentum transfers. The gray circles and magenta diamonds show relativistic and non-relativistic density functionals, respectively. Taken from Ref. [28].

Another approach is hadronic scattering, using probes such as protona [16, 17, 29, 18], α paricles [30], and pions [31]. Although the uncertainty associated with the reaction mechanism–mainly due to the limited knowledge about the nucleon-nucleon (NN) scattering amplitude inside the nuclear medium–must be carefully considered, the large statistics provided by hadronic probes are highly attractive. Consequently, they have been employed in various experiments since the latter half of the 20th century. Because the hadronic probes are sensitive to the isoscalar matter density and therefore lack isospin selectivity, they have primarily been combined with charge density distributions to extract the neutron distributions.

Proton elastic scattering at intermediate energy

Proton elastic scattering is one of the most promising hadronic probes for extracting neutron and matter density distributions. In particular, scattering at intermediate energy of 200–300 MeV, where *NN* interaction is weakest, is well-suited for this purpose, since it provides access not only to the surface but also the interior. This is because the total cross section of the proton–nucleon is relatively small in this energy region, as shown in Fig. 1.10, resulting in a relatively long mean free path inside the nucleus.

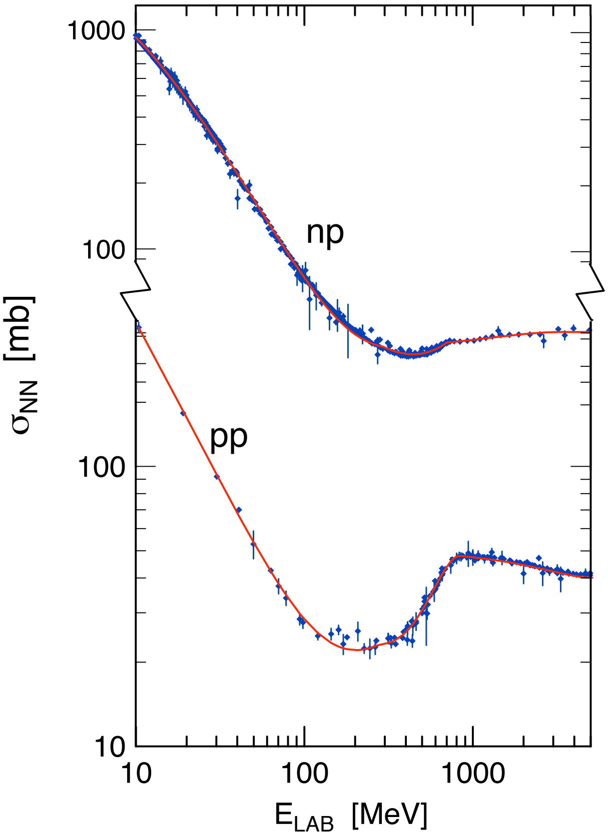

Figure 1.10: Energy dependences of the proton-proton and neutron-proton interactions. Taken from Ref. [32].

Several attempts have been made to extract neutron density distributions of Sn and Pb isotopes from proton elastic scattering measurements at 300 MeV at RCNP [29, 18]. The analysis of these works is based on the relativistic impulse approximation (RIA) models with the relativistic Love-Franey (RLF) interactions. In order to reduce the uncertainties of the NN interactions inside the nuclear matter, a phenomenological medium modification is introduced into the RLF interactions in terms of density-dependent parameters. The modification parameters are calibrated by the proton elastic scattering data of ^{58}Ni, including angular distributions of the cross section $d\sigma/d\Omega$, analyzing power A_y, and spin rotation parameter Q (Fig. 1.11). The reason for using 58Ni is that its proton and neutron density distributions are considered to have almost the same shape both experimentally and theoretically [33, 16, 12, 34]. Because this reaction model framework, medium-modified RIA (mm-RIA), is also used in this work, the details are discussed in Chap. 4.

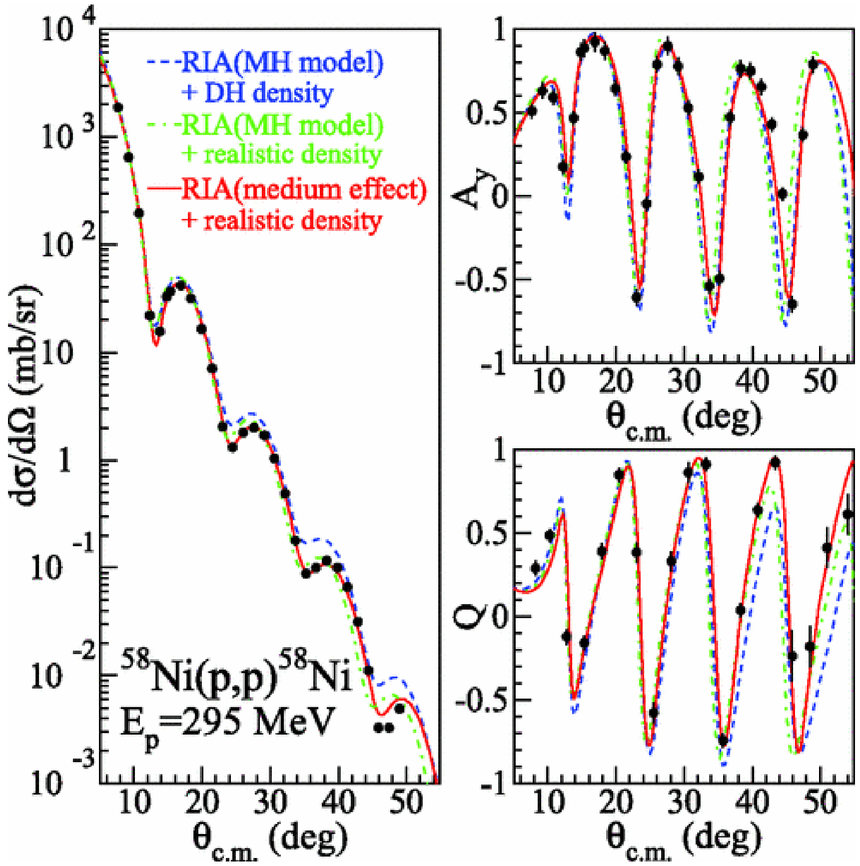

Figure 1.11: Angular distributions of the cross sections, analyzing powers, and spin rotation parameters for proton elastic scattering from ^{58}Ni at 295 MeV. The red line shows the medium-modified RIA calculations. Taken from Ref. [18]

By using the mm-RIA, the neutron density distributions of Sn and Pb isotopes are extracted in the form of model-independent sum-of-Gaussian (SOG) functions by minimizing the χ^2 values of the angular distributions of cross sections and analyzing power, as shown in Fig. 1.12. Figures 1.13a and 1.13b present the extracted densities of Sn and Pb isotopes, respectively. The key point of these studies is that the difficult-to-quantify uncertainties inherent in model-dependent parametrizations, such as two-parameter Fermi

(2pF) or three-parameter Gaussian (3pG), are overcome by employing model-independent functions. Moreover, the uncertainties of the reaction model are also taken into account, thereby ensuring a reliable evaluation of the extracted densities.

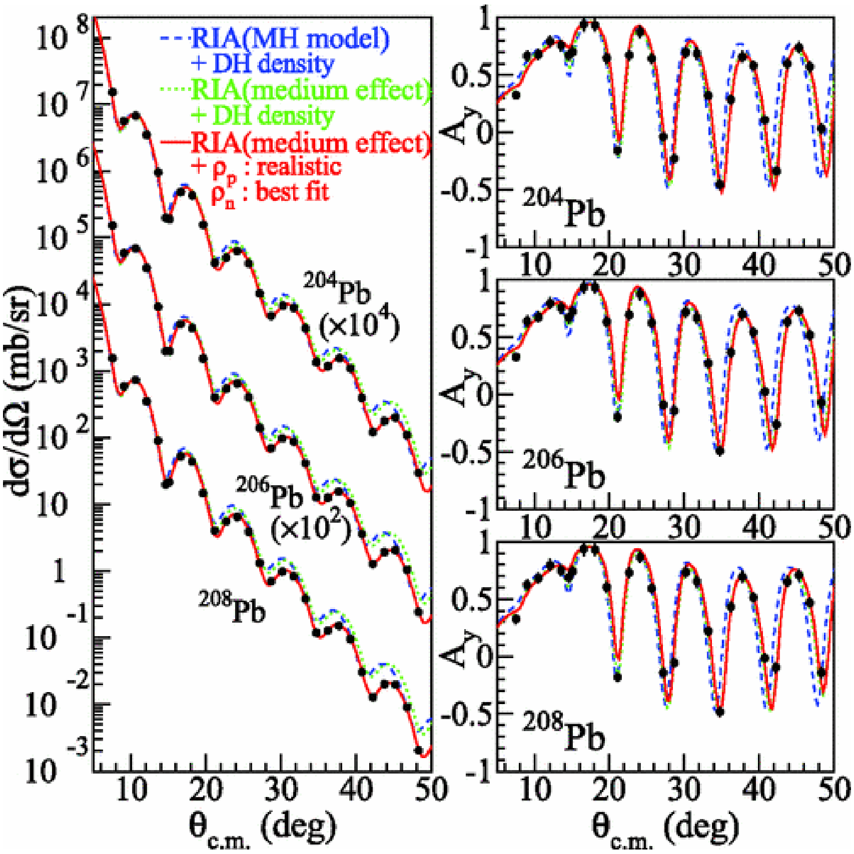

Figure 1.12: Angular distributions of cross sections and analyzing powers for proton elastic scattering from ^{204,206,208}Pb at 295 MeV. Taken from Ref. [18]

1.4 Nucleon density distributions of the unstable nuclei

Recent advances in accelerator technology and radioactive-isotope (RI) production methods have enabled extensive investigations of unstable nuclei, including neutron-rich nuclei with large isospin asymmetry. Particular attention has been drawn to their sizes and density distributions, since they are expected to have large neutron skin structures. However, unlike stable nuclei, RIs cannot be employed as fixed targets, which makes such measurements considerably more challenging.

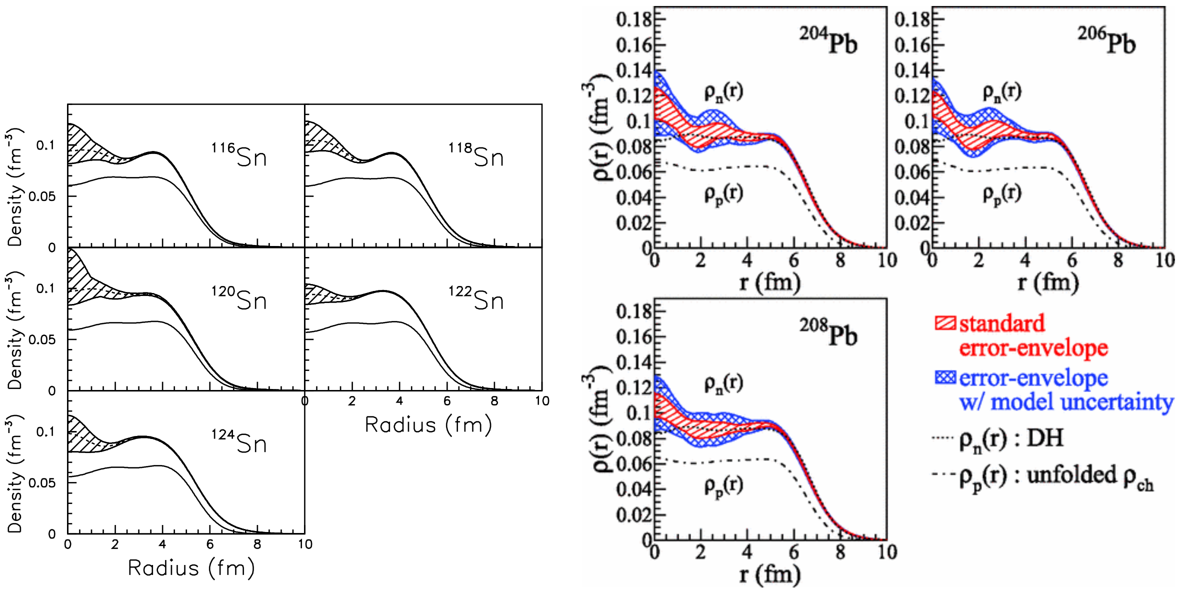

(a) Sn isotopes. Taken from Ref. [29].

(b) Pb isotopes. Taken from Ref. [18].

Figure 1.13: Densit distributions extracted from the proton elastic scattering data at 295 MeV.

1.4.1 Charge density distributions of the unstable nuclei

The isotope-shift measurements by laser spectroscopy can be performed even for short-lived nuclei. Using this method, the charge radius of ^{132}Sn was determined to be 4.7093(76) fm at ISOLDE [35, 27]. In contrast, electron scattering experiments on unstable nuclei are more challenging due to the requirement for RI targets. Recently, however, the first electron scattering measurement on an unstable nucleus, ^{137}Cs, was carried out by the self-confining RI ion target (SCRIT) project at RIKEN [36]. Further extension of this technique to a wider range of nuclei is anticipated in the future. The measurement of charge-changing cross sections σ_{cc} is a relatively recent technique [37, 38, 39]. Although its accuracy is not as high as that of the electromagnetic method, one advantage is that it allows measurements even for nuclei far from the stability line, where isotope-shift measurements are comparatively difficult. Moreover, σ_{cc} can be measured even with low-intensity ion beams, down to a few particles per second.

1.4.2 Neutron density distributions of the unstable nuclei

The methods for extracting neutron density distributions of unstable nuclei are limited mainly by the low luminosity. Neutron distributions have been investigated through matter density distributions and radii measured with the hadronic probes.

Measurement of reaction cross section (σ_R) and interaction cross section (σ_I) is known to be efficient in determining the matter radius since the discovery of the halo structure in ^{11}Li [40]. The advantages of these techniques are that they can be applied even for beams with very low intensity, down to a few particles per second, and the use of cocktail beams allows simultaneous measurements of many isotopes. Conventionally, these methods have been applied mainly to light nuclei, but recently they have been extended to heavier nuclei, including Ca isotopes [39] and Sn isotopes [41]. For heavy nuclei, however, the reaction mechanisms become increasingly complex, and their treatment remains a challenge. It should also be noted that these methods provide access only to the matter radii, while the detailed density distributions cannot be determined.

One of the most remarkable recent results in matter-radius measurements based on interaction-cross-section experiments is the study of Ca isotopes across the $N = 28$ shell closure. Figure 1.14 shows a systematic trend of the matter radii for the Ca isotopes. It was found that the matter distribution exhibits a pronounced shrinkage at $N = 28$ and a subsequent swelling beyond $N = 28$, in close analogy to the behavior of the charge distribution. A key question is whether this behavior is unique to the Ca isotopic chain or if similar features also appear in other isotopes with magic numbers, such as Sn or Pb. The answer has the potential to significantly influence the interpretation of the neutron-skin thicknesses in terms ot the nuclear matter EOS.

Proton elastic scattering in inverse kinematics

Proton elastic scattering in inverse kinematics at intermediate energies is a powerful tool for determining matter density distributions of unstable nuclei.

A notable application of this technique is the measurement using the hydrogen-filled chamber, IKAR, as an active target. Angular distributions were successfully measured for light nuclei such as He [44], Li [45], Be [46], B [47], and C [48] isotopes, which lead to deducing their matter distributions. Another approach involves storing nuclei in a storage ring and measuring their scattering with a hydrogen gas target. A successful example is the EXL (exotic nuclei studied in light-ion induced reactions at storage rings) project using the ESR storage ring at GSI. The collaboration performed the measurement for ^{56}Ni and deduced the matter radius [49]. Similarly, such experiments using the CSRe storage ring at HIRFL-CSR have been carried out for ^{58}Ni [50] and ^{78}Kr [51], though these are stable nuclei. The key achievement of both methods is that they have realized access to the small momentum-transfer region by using thin gas targets.

On the other hand, our groups have used the solid hydrogen target (SHT) for better statistics, which enables us to access up to a large momentum transfer region even for heavy nuclei. We have launched the Elastic Scattering of Protons with RI beams (ESPRI) project and developed the SHT [52] and a recoil proton spectrometer (RPS). This project aims to measure the cross sections of proton elastic scattering from unstable nuclei at intermediate energies (200–300 MeV/nucleon) by missing mass spectroscopy, covering a momentum-transfer range up to $\approx 2.5\,\mathrm{fm}^{-1}$. We have already performed experiments for several unstable nuclei such as ^{6}He [53], ^{9,10,11,16}C [54], ^{20}O, ^{50}Ca, ^{44}Ti, and ^{66,70}Ni.

Furthermore, we have proposed a new method to determine the proton and neutron density distributions separately based on proton elastic scattering. This method is particularly important for unstable neutron-rich nuclei, which are expected to exhibit large neutron skin thicknesses. In this approach, coupled equations for proton and neutron

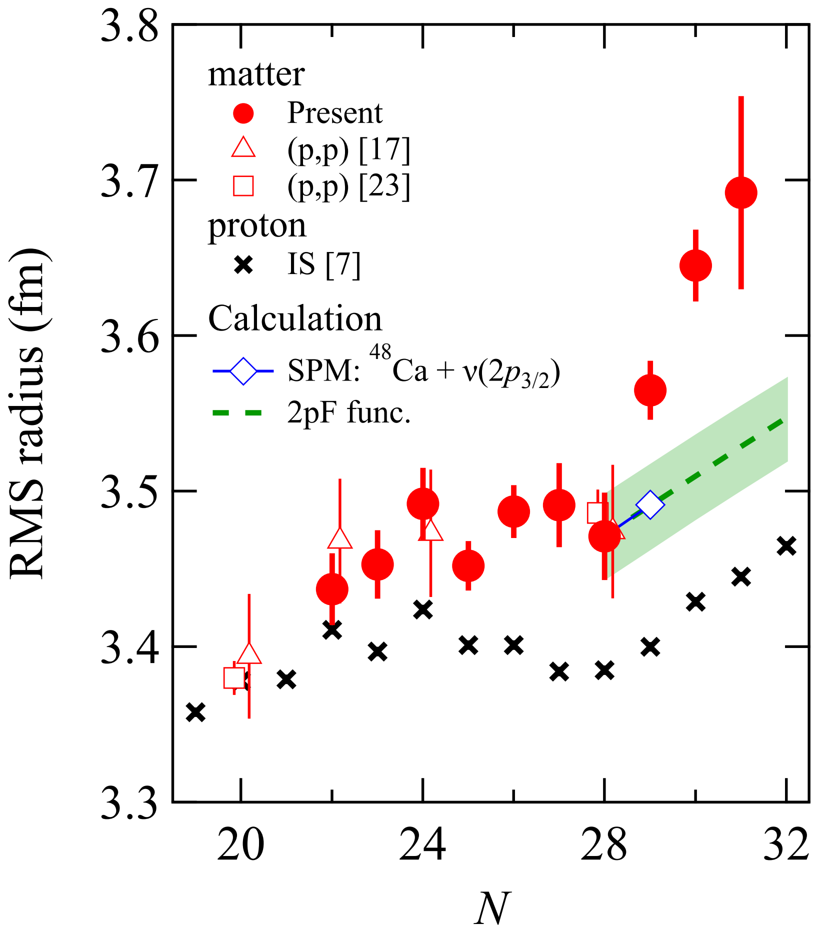

Figure 1.14: Systematic behavior of rms matter radii (red circle) and point-proton radii (black cross) for Ca isotopes. The point-proton radii were measured using the isotope-shift method [42]. Taken from Ref. [43].

form factors can be solved by measuring proton elastic scattering at two significantly different energies in the intermediate-energy region, exploiting the difference in the energy dependences of the proton-proton and proton-neutron interactions, as shown in Fig. 1.10. To confirm this possibility, proton elastic scattering data at 200 and 300 MeV were obtained. Even in the preliminary analysis, the proton and neutron radii determined by this double-energy method are consistent with those obtained using conventional methods, which combine charge density distribution with proton elastic scattering data at a single energy (200 or 300 MeV) [55], as shown in Table 1.2.

Table 1.2: Deduced root-mean-square proton and neutron radii by the three methods: proton elastic scattering at 300 MeV plus chrag density distribution ρ_{ch}, proton elastic scattering at 200 MeV plus chrag density distribution ρ_{ch}, and proton elastic scattering at 200 & 300 MeV. Taken from Ref. [55].

	300 MeV + ρ_{ch}	200 MeV + ρ_{ch}	200 & 300 MeV
r_p [fm]	4.200	4.200	4.21(2)
r_n [fm]	4.285(16)	4.300(22)	4.300(17)

1.5 Purpose of this work

In this thesis, we reported the measurement of proton elastic scattering from ^{132}Sn in inverse kinematics around 200 MeV/nucleon. Since measuring proton elastic scattering from heavy RIs over a wide momentum-transfer range is not straightforward, it had not been accomplished before. However, by developing a new particle-identification method, a solid hydrogen target, and a recoil proton spectrometer, we succeeded in performing such measurements for the first time.

We then tested whether the reaction frameworks used for analyzing proton elastic scattering for stable nuclei also work well for data from nuclei with large isospin asymmetry. Although the proton and neutron density distribution cannot be deduced separately because we analyzed the data only at a single energy, the matter density distribution and radius were extracted, which have not been measured previously. In addition, a combined analysis with the charge radius gave the neutron skin thickness. The PDR experiment on ^{132}Sn [56] represents the only attempt to deduce the neutron skin thickness, but the result highly depends on the model. Therefore, this study plays a significant role in investigating the structure of systems with large isospin asymmetry and in advancing our understanding of the EOS of asymmetric nuclear matter.

Furthermore, thanks to remarkable progress in theoretical approaches and computational technologies, *ab initio* calculations starting from chiral effective theory (EFT) have become applicable to heavy nuclei, including ^{132}Sn and ^{208}Pb [57, 58, 59, 60]. These advances enable a direct examination of nuclear forces derived from chiral EFT through measurements of the size of heavy nuclei, thereby further enhancing the significance of the present study. In this work, we compare density distributions predicted by several *ab* *initio* calculations employing in-medium similarity renormalization group (IMSRG), as well as the angular distributions of proton elastic scattering obtained from the densities via RIA calculations, with the experimental results.

In Chapter 2, the experimental setup is described. In Chapter 3, the details of the data reduction and the obtained crosse sections are described. In Chapter 4, the explanation of the mm-RIA and the results of extracted matter density distributions of ^{132}Sn are shown. In Chapter 5, the angular distributions of cross section and the extracted matter radius are compared with several theoretical calculations. Finally, the summary is given in Chapter 6.

Chapter 2

Experiment

The experiment was performed at the Radio Isotope Beam Factory (RIBF) at RIKEN. Figure 2.1 shows an overview of RIBF. In addition to ^{132}Sn, we performed proton elastic scattering for a stable nucleus, ^{48}Ca, to suppress the systematic uncertainty of the secondary-target thickness and recoil-proton detectors.

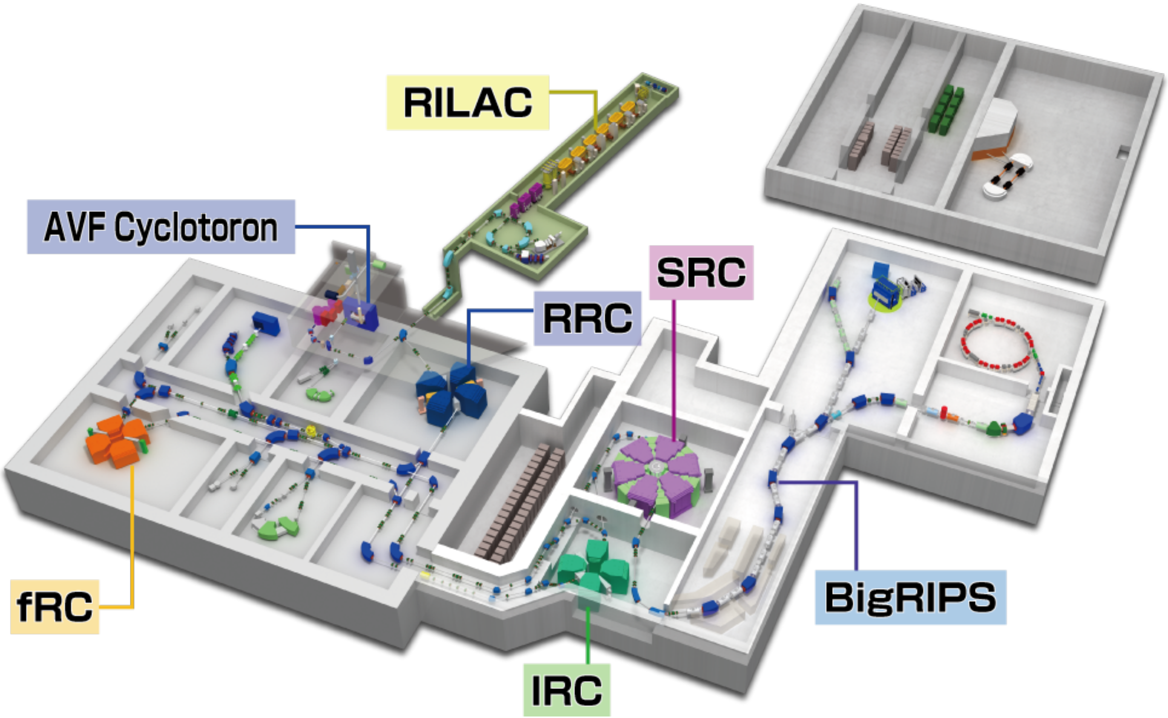

Figure 2.1: Overview of RIBF at RIKEN. Taken from Ref. [61].

2.1 Beam Production

The secondary beam, including ^{132}Sn, was produced via the in-flight fission of ^{238}U. An ^{238}U ion from the superconducting electron cyclotron resonance (SC-ECR) ion source was accelerated to 345 MeV/nucleon with the beam intensity of about 40 particle nA by the RILAC2 injector and four cyclotrons (RRC, fRC, IRC, and SRC), as indicated by the orange line in Fig. 2.2. The accelerated primary ^{238}U beam was bombarded on the 4-mm-thick ^{9}Be target at the achromatic focal plane (F0), and the produced secondary beam was separated and identified by the BigRIPS spectrometer. To produce a beam including ^{48}Ca, a 7-mm-thick ^{9}Be was used.

Figure 2.3 shows the secondary beamline and installed detectors. It should be noted that CNS active target (CAT) detectors [62] were installed at F8 to measure IMSRG in parallel. The beamline detectors at BigRIPS are used for both CAT and ESPRI measurements. This experiment is the first parallel experiment including multiple scattering sites at RIBF.

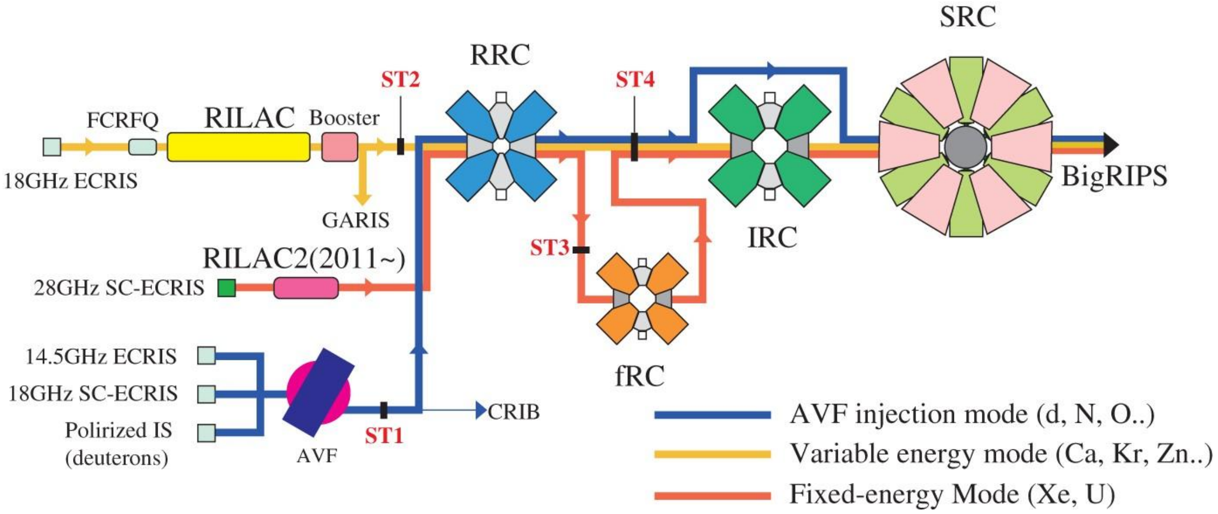

Figure 2.2: Schematic view of the beam acceleration. Taken from Ref. [63].

2.2 BigRIPS Spectrometer

Since the secondary beam has various nuclei, it is required to separate or identify the isotopes. BigRIPS is a superconducting in-flight RI beam separator at RIBF and has seven focal planes (F1–F7), six dipole magnets (D1–D6), and fourteen superconducting triplet quadrupole magnets [64]. The F3 and F7 are momentum achromatic planes, while

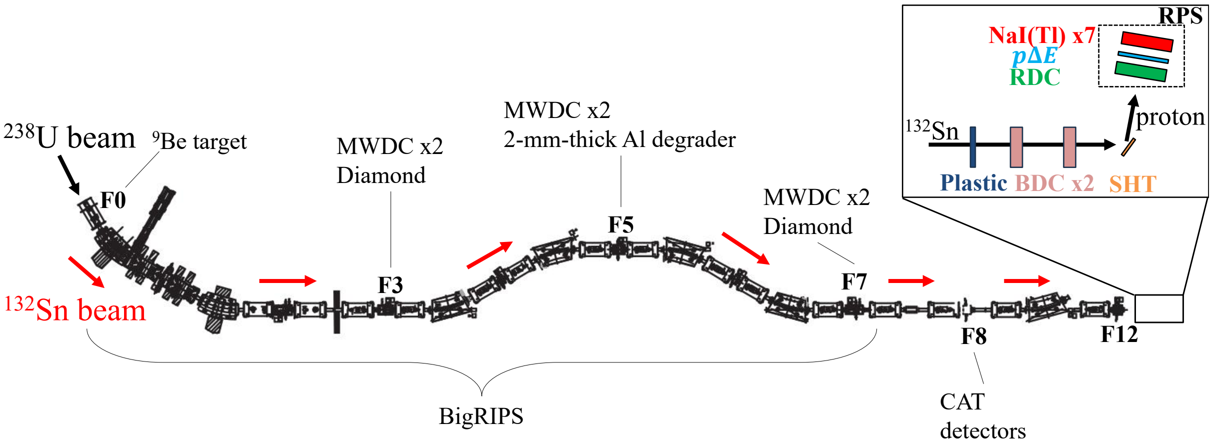

Figure 2.3: The schematic view of the beamline and installed materials.

F1 and F5 are dispersive planes. BigRIPS consists of two stages: the first stage, from F0 to F2, to separate the beam particles, and the second stage, from F3 to F7, to select particles based on their atomic number, charge, mass, and momentum. The wedge-shaped degraders were installed in F1 and F5. In the second stage, the particles are identified event-by-event by installing beamline detectors at the focal planes to measure the $B\rho$ value, the time of flight (TOF), and the energy loss (ΔE). Table 2.1 summarizes the setting of BigRIPS.

At BigRIPS, plastic scintillators, parallel-plate avalanche counters (PPACs) [65], and a multi-sumpling ionization chamber (MUSIC) are used as the standard detectors, and the TOF-$B\rho$-ΔE method is adopted as the conventional PID technique [66]. While these detectors are used during the tuning for the low-intensity beam, they are unsuitable for high-intensity heavy-ion beams exceeding 100 kcps due to radiation damage and low efficiency. Thus, a new PID method called TOF-$B\rho$-$B\rho$ was adopted, using diamond detectors and low-pressure multi-wire drift chambers (LP-MWDCs). The present experiment is the first physics experiment employing the PID method.

2.2.1 TOF-$B\rho$-$B\rho$ method

The secondary cocktail beam was identified using the so-called TOF-$B\rho$-$B\rho$ method [67]. To apply this method, we determined the time of flight between F3 and F7 (TOF_{37}), the magnetic rigidity between F3 and F5 ($B\rho_{35}$), and the magnetic rigidity between F5 and F7 ($B\rho_{57}$). These quantities are related as follows:

$$\mathrm{TOF}_{37} = \frac{L_{35}}{\beta_{35}c} + \frac{L_{57}}{\beta_{57}c}, \tag{2.1}$$

$$\left(\frac{A}{Q}\right)_{35} = \frac{B\rho_{35}}{\beta_{35}\gamma_{35}} \cdot \frac{e}{m_u c}, \tag{2.2}$$

$$\left(\frac{A}{Q}\right)_{57} = \frac{B\rho_{57}}{\beta_{57}\gamma_{57}} \cdot \frac{e}{m_u c}, \tag{2.3}$$

Table 2.1: List of parameter configurations of the BigRIPS.

Aluminum degrader thickness (mm)		
	^{132}Sn	^{48}Ca
F1	3.5	7.0
F5	2.0	5.0

Slit opening area (mm)		
	^{132}Sn	^{48}Ca
F1	±21.4	−30.0, +64.2
F2	±2.0	−3.0, +5.0
F5	±110.0	±110.0
F7	±5.0	−8.0, +10.0

Dipole magnet rigidity (T·m)		
	^{132}Sn	^{48}Ca
D1	7.4500	6.6800
D2	6.7703	6.2275
D3	6.5835	6.1587
D4	6.5835	6.1587
D5	6.0150	5.6831
D6	6.0150	5.6831

with the speed of light c, the atomic mass unit m_u, the elementary charge e, the flight path length L, the Lorentz factor γ, the velocity relative to the speed of light β. The subscripts of "35", "57", and "37" represent the quantities with respect to the F3–F5, F5–F7, and F3–F7, respectively. By assuming the charge state doesn't change at F5,

$$\frac{B\rho_{35}}{B\rho_{57}} = \frac{\beta_{35}\gamma_{35}}{\beta_{57}\gamma_{57}}. \tag{2.4}$$

By solving Eqs. (2.1) and (2.4), β and γ can be obtained. Then, the A/Q can be obtained. The energy loss in the F5 degrader ΔE is expressed by

$$\Delta E = (\gamma_{35} - 1)Am_u - (\gamma_{57} - 1)Am_u. \tag{2.5}$$

On the other hand, the energy loss can also be expressed as the Bethe-Bloch formula $dE/dx \propto Z^2/\beta_{35}^2$. From these formulas and the assumption $Q = Z$, the atomic number Z can be obtained as:

$$Z = C_0 + C_1\Big((\gamma_{35} - \gamma_{57})\beta_{35}^2\Big(\frac{A}{Q}\Big)_{35} + C_2 x_5\Big) \tag{2.6}$$

where C_0, C_1, and C_2 are empirical coefficients, and x_5 is the postion at F5. The last term represents the wedge-shaped effects of the F5 degrader.

The TOF$_{37}$ were measured using the diamond detectors placed at F3 and F7 (F3 & F7 Dia). The $B\rho$ values are determined using the positions measured by the LP-MWDCs placed at F3, F5, and F7. The $B\rho$ is expressed as

$$B\rho = B\rho_0(1 + \delta) \tag{2.7}$$

with the central rigidity $B\rho_0$ and momentum dispersion δ. When transporting the beam from F3 (F5) to F5 (F7), the optical vector changes as

$$\begin{pmatrix} x_i \\ a_i \\ \delta_{ij} \end{pmatrix} = \begin{pmatrix} (x|x)_{ij} & (x|a)_{ij} & (x|\delta)_{ij} \\ (a|x)_{ij} & (a|a)_{ij} & (a|\delta)_{ij} \\ 0 & 0 & 1 \end{pmatrix} \begin{pmatrix} x_j \\ a_j \\ \delta_{ij} \end{pmatrix}, \tag{2.8}$$

$$(i, j) = (3, 5), (5, 7), \tag{2.9}$$

where x_i and a_i are the position and angle at i-th focal plane. We used the ion-optics matrix elements calculated by COSY Infinity in the standard optics mode, provided in Ref. [68], and summarized in Table 2.2. Since $(x|a)$ values are negligible, by solving the (2.8), δ_{ij} is expressed as

$$\delta_{ij} = \frac{x_j - (x|x)_{ij}x_i}{(x|\delta)_{ij}}. \tag{2.10}$$

Therefore, we can obtain the $B\rho$ values by measuring the positions at the focal planes.

Table 2.2: Transfer matrix elements from F3 to F5 and from F5 to F7.

	F3–F5	F5–F7
$(x\|x)$	$0.92025 \times 10^{+0}$	$0.10871 \times 10^{+1}$
$(x\|a)$ [mm/rad]	-0.84647×10^{-9}	0.22471×10^{-8}
$(x\|\delta)$ [mm/%]	$0.31687 \times 10^{+2}$	$-0.34454 \times 10^{+2}$
$(a\|x)$ [rad/mm]	-0.36118×10^{-8}	0.22198×10^{-8}
$(a\|a)$	$0.10867 \times 10^{+1}$	$0.91969 \times 10^{+0}$
$(a\|\delta)$ [rad/%]	-0.70416×10^{-9}	-0.75073×10^{-7}

2.2.2 Detector setup at BigRIPS

Diamond detector

We installed diamond detectors on F3 and F7 to measure the TOF. The signal of the F7 diamond detector was also used for serving the beam trigger. The diamond detectors were developed at the Center for Nuclear Science (CNS), the University of Tokyo. The material was artificially produced using the chemical vapor deposition (CVD) technique, which enables the fabrication of crystals large enough to be used as radiation detectors. Its size and thickness are $30 \times 30\,\mathrm{mm}^2$ and 0.2 mm, respectively. While there is one pad on the anode side, the $28 \times 28\,\mathrm{mm}^2$ cathode is separated into 4 strips at the other side. However, due to issues with the strip readout, only the singlas from the pad electrode were used in the analysis in this work.

The signals were amplified by low-noise current amplifiers (Cividec C2-HV for strips and CAEN A1423B for pads). After discrimination, the signals were recorded by a multi-hit time-to-digital converter (TDC) (CAEN V1290).

Low-pressure multi-wire drift chamber

We installed low-pressure drift chambers (LP-MWDCs) [69] on F3, F5, and F7 to measure the trajectories at each focal plane. The configurations are summarized in Table 2.3. While both vertical and horizontal trajectories are used for the beam tuning, only the horizontal trajectories are used for the analysis.

The signals were Amplifier-Shaper-Discriminator (ASD) boards (Repic, RPA 132), and then the timing signals with the timing-over-threshold (TOT) information were recorded by the multi-hit TDCs (CAEN V1190A).

2.3 Proton elastic scattering in inverse kinematics

Before describing the experimental setup around the secondary target, an outline of the method for measuring proton elastic scattering is provided. To determine the cross section of proton elastic scattering, elastic events should be distinguished from inelastic scattering

Table 2.3: Specifications of MWDCs installed at BigRIPS. The wire positions of the X’ and Y’ planes are shifted by half cells.

F3DC1	
Layer configuration	XX’YY’XX’YY‘
Cell size	$3\times3\,\mathrm{mm}^2$
Effective area	$48\times48\,\mathrm{mm}^2$
Gas	isobutane
F3DC2	
Layer configuration	XX’YY’
Cell size	$5\times5\,\mathrm{mm}^2$
Effective area	$48\times48\,\mathrm{mm}^2$
Gas	isobutane
F5DC1,2	
Layer configuration	XX’UV
Cell size	$5\times5\,\mathrm{mm}^2$
Effective area	$216\times144\,\mathrm{mm}^2$
Gas	isobutane
F7DC1,2	
Layer configuration	XX’YY’XX’YY’
Cell size	$4.8\times5\,\mathrm{mm}^2$
Effective area	$60\times60\,\mathrm{mm}^2$
Gas	isobutane

and other reaction channels based on the reconstructed excitation energy. In this work, missing-mass spectroscopy was employed to extract the excitation energy.

For a two-body reaction, the recoil particle energy T_p can be obtained by solving the following equation:

$$aT_p^2 + bT_p + c = 0, \tag{2.11}$$

$$\begin{cases} a &= (m_b + T_b + m_p)^2 - (2m_b + T_b)T_b \cos^2\theta \\ b &= 2(m_b + T_b + m_p)(m_b E_x + E_x^2/2) - 2(2m_b + T_b)m_p T_b \cos^2\theta \ , \\ c &= (m_b E_x + E_x^2/2)^2 \end{cases}$$

with the physical quantities listed in Table 2.4. Thus, the excitation energy E_x can be deduced by measuring the incident energy T_b, recoil-particle energy T_p, and scattering angle θ. The scattering angle was determined by measuring both beam-particle and recoil-particle angles. While the beam energy was obtained from the position at dispersive focal plane F5, the other quantities were measured around the secondary target.

Table 2.4: Physical quantities of the two-body kinematics.

m_b	mass of beam particle (^{132}Sn)
T_b	incident energy
m_p	mass of target particle (proton)
T_b	kinetic energy of recoil particle (proton)
θ	scattering angle
E_x	excitation energy

2.4 Setup around the secondary target

The secondary beam was transported to the twelfth focal plane (F12), where the secondary target was installed. Figure 2.4 shows a schematic view of the setup around the secondary target. The ^{132}Sn beam was bombarded on the solid hydrogen target (SHT), and recoil protons were detected by the recoil proton spectrometer (RPS). On the upstream of the SHT, a plastic scintillator (F12pla), two beamline low-pressure MWDCs (BDC1 and BDC2) were placed to measure the timing, to track the beam. While two plastic scintillators are installed to identify the ejectile particles on the downstream of the SHT, they did not work stably due to the attenuation of the light yield caused by the high-intensity heavy beam. Thus, the detectors were not used for the analysis in this work.

2.4.1 Beamline detectors at F12

Figure 2.5 shows the side view of the beamline at F12. The F12pla were used to provide the beam timing information, which was used as a start timing of the TOF of the recoil

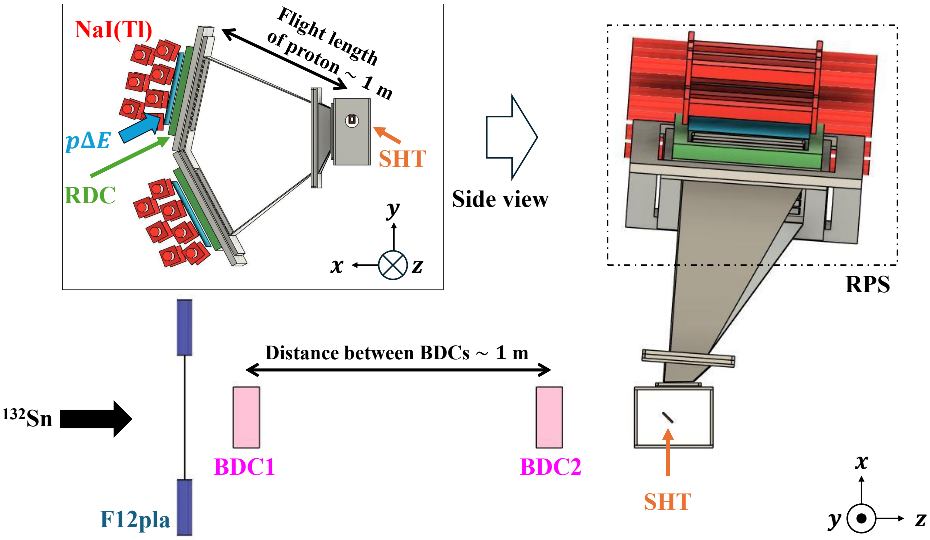

Figure 2.4: Schematic view around the secondary target.

protons, and for the start timing of the drift timing of the BDCs. Figure 2.6 shows the photograph of F12pla. The light output was read out by two photomultiplier-tube (PMT) assemblies (Hamamatsu H2431-50) attached to both sides. The charge and timing of the signals were recorded by a charge-to-digital converter (QDC) (CAEN V792) and a TDC (CAEN V1290), respectively.

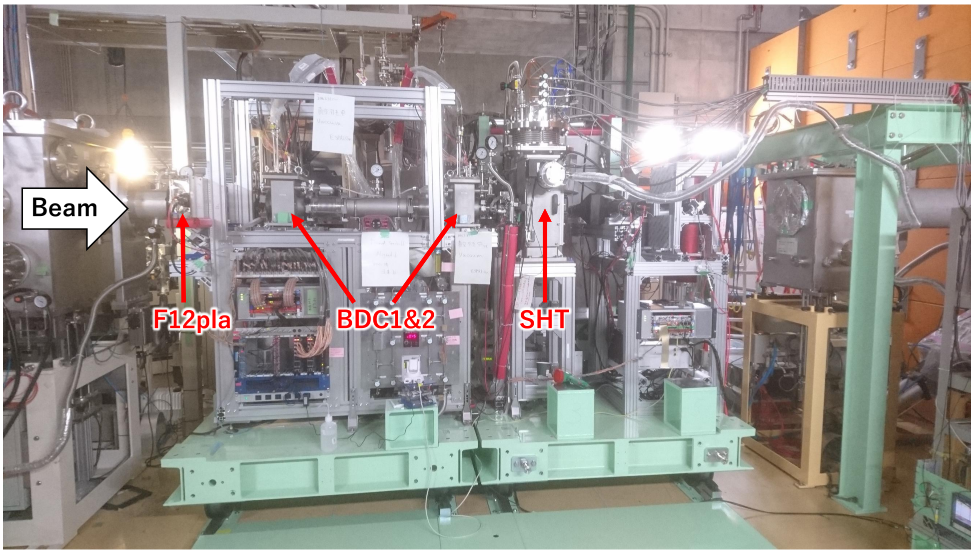

Figure 2.5: Photograph of F12 area.

The two BDCs [70, 71], which had been developed for our ESPRI project, were installed with a distance of about 1 m to measure the beam trajectory. The trajectory gave us the incident angle of the beam and the hit position on the target. The configurations are summarized in Table 2.5. The BDCs were installed in the vacuum chambers and

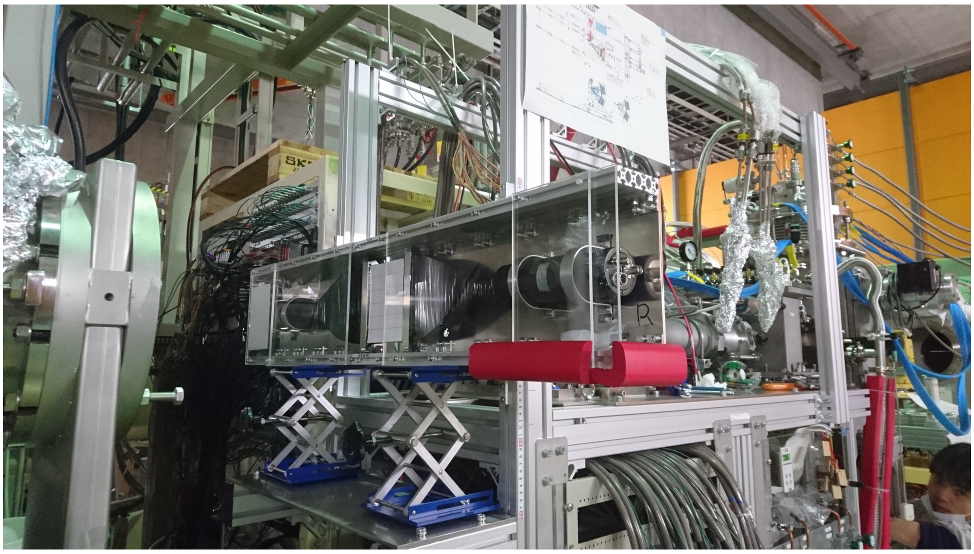

Figure 2.6: Photograph of F12pla.

operated at a low pressure of 67 mbar. The signals were Amplifier-Shaper-Discriminator (ASD) boards (GND GNA-110), and then the timing signals with the TOT information were recorded by the multi-hit TDCs (CAEN V1190A).

Table 2.5: Specification of BDCs. The wire positions of the X’ and Y’ planes are shifted by half cells.

BDC1&2	
Layer configuration	XX’YY’XX’YY‘
Cell size	$5{\times}5\,\mathrm{mm}^2$
Effective area	$77.5{\times}77.5\,\mathrm{mm}^2$
Anode wire	Au-W/Re 16 μmϕ
Cathode wire	Au-Al 80 μmϕ
Gas	CH_4

2.4.2 Solid hydrogen target

We used a solid hydrogen target (SHT) [52] as a proton target. Figures 2.7 and 2.8 show photographs of the SHT system and the produced SHT, respectively. Compared with compound targets such as polyethylene, using a pure hydrogen target effectively suppresses background events originating from other nuclei. The SHT had an elliptical shape with a major axis of 35.4 mm and a minor axis of 20 mm, and a thickness of 1 mm. As shown in Fig. 2.4, the SHT was tilted by 45° to reduce multiple scattering of the recoil protons in the target In this configuration, the effective area corresponded to a 25 mm-diameter circle, and the target thickness along the beamline is about 1.4 mm. This thin target enabled high excitation-energy resolution by minimizing the uncertainty of the reaction point along the beam axis and reducing the multiple scattering of the recoil protons. 6-μm-thick aramid films were used for the windows. The number of protons included in the SHT was evaluated by the cross section of the proton elastic scattering for the ^{48}Ca in the same beam time.

Figure 2.7: Photograph of the SHT system.

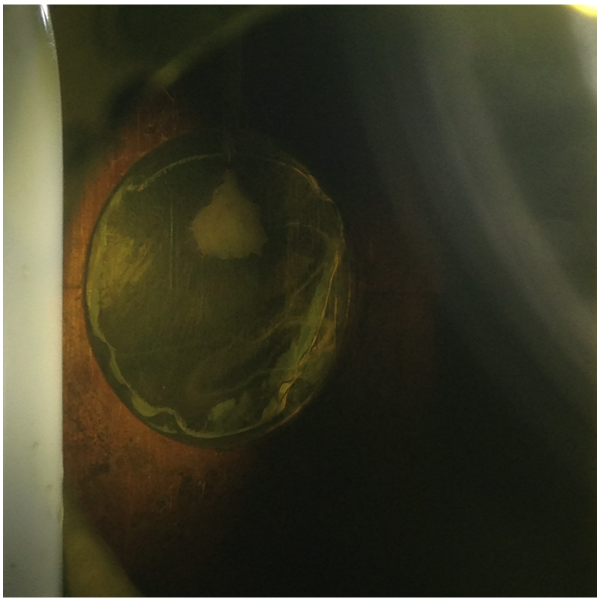

Figure 2.8: Photograph of the produced SHT.

2.4.3 Recoil Proton Spectrometer

Two detector sets for detecting recoil particles were placed at the upper and lower windows of the large vacuum chamber, as shown in Fig. 2.4. Figures 2.9 and 2.10 show side-view photographs of the RPS chamber and the RPS detectors, respectively. Each set consists of an MWDC for recoil-particle tracking (recoil drift chamber; RDC), a plastic scintillator ($p\Delta E$), and seven NaI(Tl) calorimeters. The detector sets were used to identify recoil particles and to measure the kinetic energy and angle of the recoil protons. Because the angular resolution obtained from the RDC tracking was insufficient, the recoil proton angle was determined by combining the hit position on the RDC with the reaction point on the target derived from the BDC tracking. In this work, only the upper-side data were analyzed due to an issue with the lower RDC.

Recoil drift chamber

The RDCs were used for the angles of the recoil protons. The configurations are summarized in Table 2.5. In this work, the first layer of X-plane was excluded from the analysis because of excessive noise. The signals were ASD boards (GND GNA-180), and then the

Figure 2.9: Photograph of the RPS chamber in the side view.

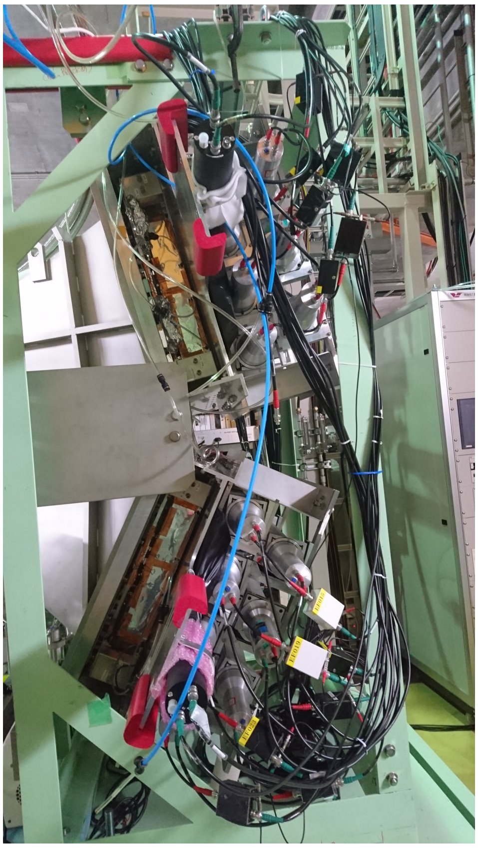

Figure 2.10: Photograph of the RPS detectors: RDCs, $p\Delta E$s, and NaI(Tl) calorimeters.

timing signals were recorded by the multi-hit TDCs (AMSC AMT-VME TDC). The TOT information was not recorded exclusively for the first X-plane.

Table 2.6: Specification of RDCs. The wire positions of the X' and Y' planes are shifted by half cells.

RDC Up&Down	
Layer configuration	XYXYX'Y'X'
Cell size	$14{\times}14\,\mathrm{mm}^2$
Effective area	$436{\times}436\,\mathrm{mm}^2$
anode wire	Au-W/Re 30 μmϕ
cathord wire	Be-Cu 100 μmϕ
Gas	Ar(50%) + C_2H_6 (50%) 1. atm

$p\Delta E$

The plastic scintillator $p\Delta E$ provided the timing and energy loss information of the recoil protons. The effective area and thickness are $440 \times 440\,\mathrm{mm}^2$. The thicknesses were 2.53 mm for upside and 3.09 mm for downside. The light output was read out by two PMT assemblies (Hamamatsu h7195) attached to both sides. The charge and timing of the signals were recorded by a charge-to-digital converter (QDC) (CAEN V792) and a TDC (CAEN V1290), respectively.

NaI(Tl) calorimeter

The NaI(Tl) calorimeter was used to measure the kinetic energy of recoil protons. For the upper set, the detectors are labeled NaI1 through NaI7 from top to bottom. The effective area and thickness are $431.8 \times 45.72\,\mathrm{mm}^2$ and 50.8 mm, respectively. The crystal was hermetically sealed in aluminum frames, and the entrance window had a thickness of 0.1 mm. The signals from the PMTs (Hamamatsu R1307) were first amplified by emitter-follower preamplifiers, then shaped by a pulse-shaping amplifier (CAEN N156B), and finally, the peak heights were recorded using a peak-sensing analog-to-digital converter (PS-ADC, CAEN V785). The calorimeters were tested with proton beams at 20, 40, 60, and 80 MeV [72]. As a typical result, an energy resolution of 0.3% was obtained for the 80 MeV proton beams.

2.5 Data acquisition system

The data acquisition (DAQ) system was based on the RIBFDAQ framework [73] and employed three event builders: BLD, CAT, and ESPRI. Figure 2.11 shows the DAQ diagram. Each builder recorded the data with a common trigger basis, where the common trigger was distributed by the general trigger operator (GTO) module [74]. The trigger logic is described in the following subsection.

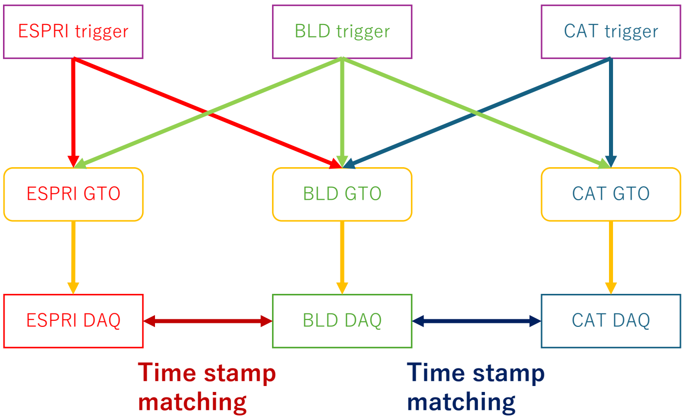

Figure 2.11: DAQ diagram.

Because the beam intensity was high (about 200 kcps) and triggers from the CAT, ESPRI, and BLD detectors were applied, the trigger rate received by the BLD builder was relatively high. Therefore, we introduced a parallel-readout VME DAQ system utilizing mountable controllers (MOCOs) for the BLD readout. This experiment represents the first physics application of MOCOs.

In conventional VME-based readout systems, a single controller typically reads out multiple modules sequentially. By equipping each VME module with a MOCO, parallel readout was achieved, thereby reducing the dead time. Subsequently, the MOCO with parallelized VME (MPV) [75]–integrating MOCOs with a parallel-readout backplane and a dedicated controller–was developed and has since been widely adopted at RIBF.

The data from the ESPRI builder was merged with that from the BLD builder using a time-stamping system [76]. The time stamps were recorded by the logic unit for programmable operation (LUPO) modules [77]. The merging efficiency exceeded 99.9% while all DAQ systems operated properly.

The number of accepted triggers, requested triggers, and other numbers of the detector hits were recorded using VME scalers (Struck Innovative Systeme GmbH SIS3820).

2.5.1 Trigger condition

The beam trigger was generated from the pad signal of the F7Dia, which was downscaled by a factor of 1/10,000. The trigger was mainly used for evaluating the performance of the BLDs as well as for investigating the properties of the beam. Figure 2.12 shows the diagram of the ESPRI trigger, which means the reaction trigger at F12. The trigger was used for the physical analysis. The CAT tigger was not used in this analysis.

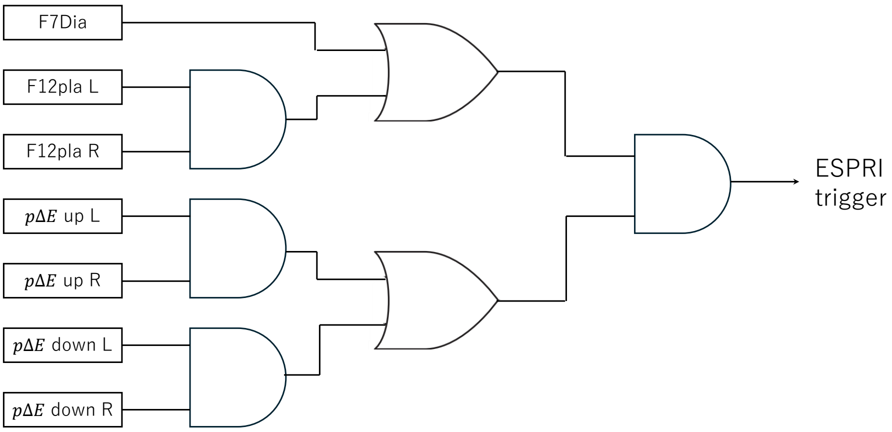

Figure 2.12: Diagram of trigger circuit.

Chapter 3

Data reduction and Results

In this chapter, the data reduction process is described to obtain the angular distribution of the differential cross section $d\sigma/d\Omega$ for proton elastic scattering from ^{132}Sn. Figure 3.1 presents the flowchart of the data reduction.

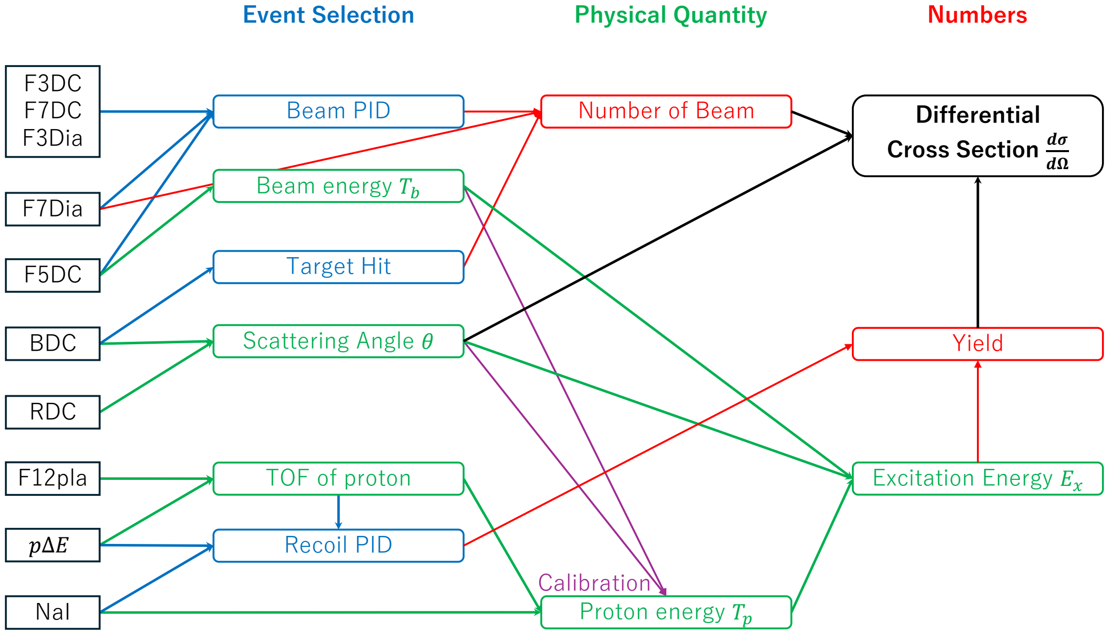

Figure 3.1: Flow chart showing the derivation of differential cross sections.

3.1 Beam analysis

In this section, the analysis of beam particles is presented, using the beam-trigger data.

3.1.1 MWDC

The tracking analysis using the LP-MWDCs placed at F3, F5, and F7, and the BDCs, is described.

First, the drift timing was obtained by subtracting the timing of the reference detector from the measured timing of each MWDC. The reference detectors were F3Dia for F3DC and F5DC, F7Dia for F7DC, and F12pla for the BDCs. The upper panel of Fig. 3.2 shows the typical timing distribution of the first X plane (X1) of BDC1. The drift timing DT was converted into drift length using a space-time conversion (STC) function F_{STC}, defined as

$$F_{\mathrm{STC}}(DT) = \frac{C}{2} \times \frac{\int_{T_{\mathrm{min}}}^{DT} f_t dt}{\int_{T_{\mathrm{min}}}^{T_{\mathrm{max}}} f_t dt}, \tag{3.1}$$

where C denotes a cell size. Here, f_t represents the normalized distribution of the drift times from T_{min} to T_{max}. The lower panel of Fig. 3.2 shows the typical drift length distribution of X1 of BDC1.

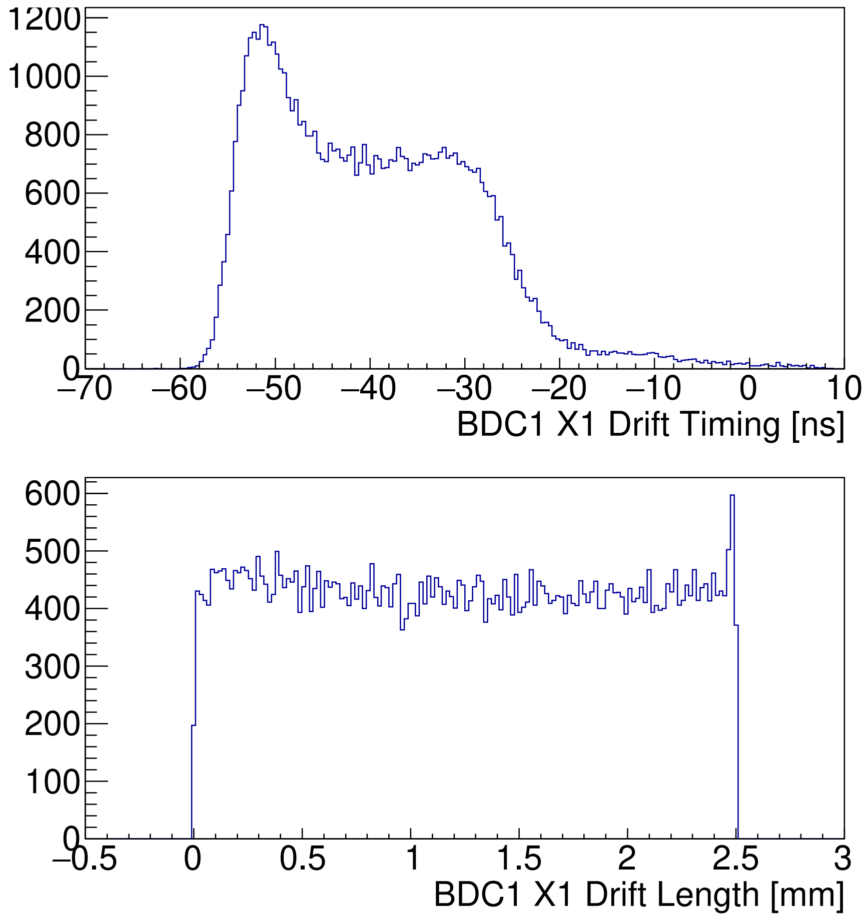

Figure 3.2: (Upper panel) TDC spectrum on X1 plane of BDC1. (Lower panel) Drift length distribution converted from TDC spectrum.

The position X and angle A of a trajectory were determined by minimizing the χ^2, defined as

$$\chi^2 = \sum_i (f(z_i) - x_i - dl_i)^2, \tag{3.2}$$

$$f(z) = X + Az, \tag{3.3}$$

where dl_i, x_i, and z_i denote the obtained drift length, the wire position, and the plane coordinate along with the beam axis of the i-th plane, respectively.

3.1.2 Beam PID

The identification of the beam particles was performed based on TOF-$B\rho$-$B\rho$ method.

Using the measued timings of F3Dia and F7Dia (t_3 and t_7), the time-of-flight between F3 and F7 (TOF_{37}) can be represented as

$$TOF_{37} = t_7 - t_3 - t_{\mathrm{off}}. \tag{3.4}$$

Here, t_{off} is the time offset arising from the signal path difference. As ^{132}Sn can be identified from the plot of the X position of F5 (F5X) versus $t_7 - t_3$, shown in Fig. 3.3, t_{off} was determined such that A/Q of ^{132}Sn is 2.64. Figure 3.4 shows the A/Q spectrum after the t_{off} calibration.

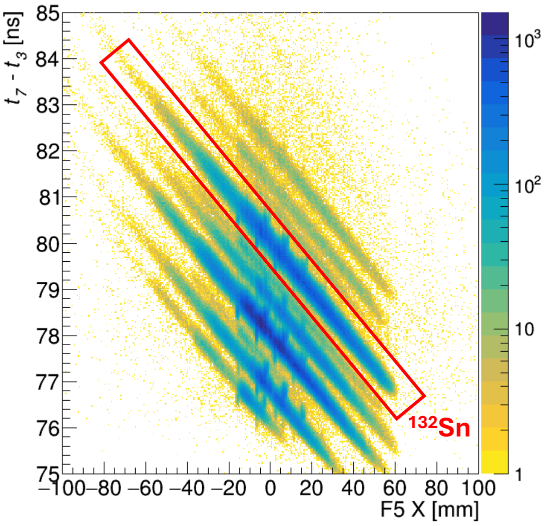

Figure 3.3: 2D histogram of F5X versus $t_7 - t_3$.

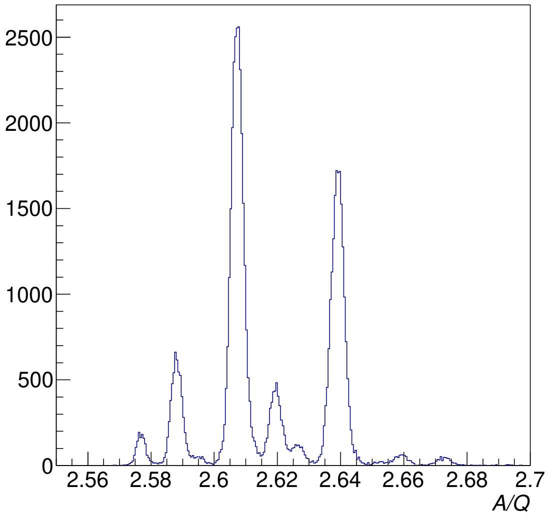

Figure 3.4: A/Q spectrum.

Next, the determination of Z was performed. The coefficient C_2 in Eq. (2.6) was determined from the correlation between F5X and $(\gamma_{35} - \gamma_{57})\beta^2(A/Q)_{35}$ shown in Fig. 3.5. Subsequently, C_0 and C_1 were calibrated using nuclei around $Z = 50$. Figure 3.6 presents the resulting PID plot of the beam particles, where a clear separation was achieved. The resolutions of Z and A/Q for ^{132}Sn were $\Delta Z = 0.237$ and $\Delta(A/Q) = 0.00206$. The events satisfying the following equation with (Z, A/Q) were identified as ^{132}Sn.

$$\sqrt{\left(\frac{Z-50}{\Delta Z}\right)^2 + \left(\frac{A/Q-2.64}{\Delta(A/Q)}\right)^2} \leq 3. \tag{3.5}$$

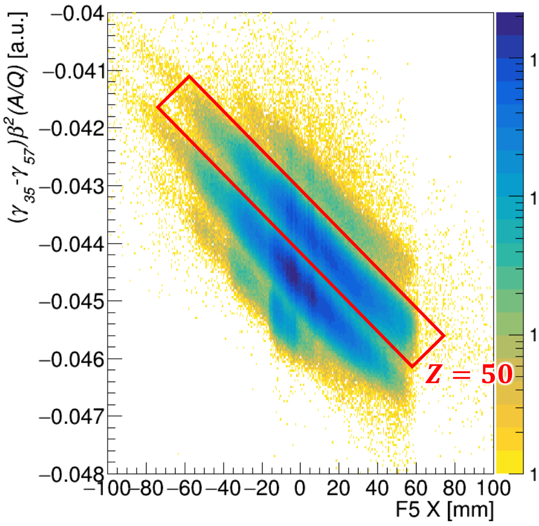

Figure 3.5: 2D histgram of F5X versus $(\gamma_{35} - \gamma_{57})\beta^2(A/Q)_{35}$.

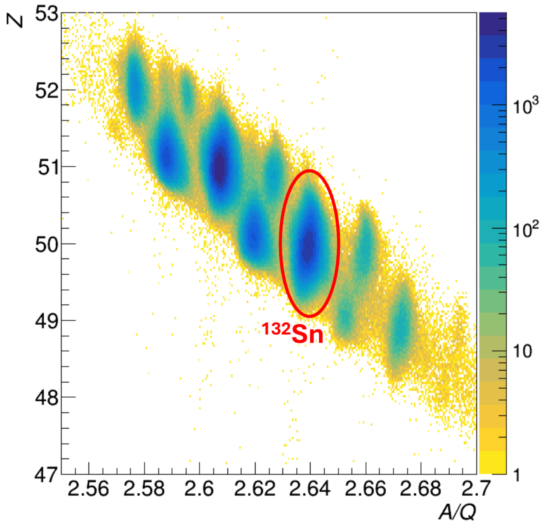

Figure 3.6: Beam PID spectrum: 2D histgram of A/Q versus Z.

3.1.3 Beam energy

The beam energy T_b was determined event-by-event from the horizontal position at the dispersive focal plane F5 (F5X). Using the RI-beam simulator Lise++ [78] for the fragment separator, the correlation between F5X and the beam energy at the center of the SHT was evaluated, taking into account the energy loss in the materials between F5 and the SHT. Figure 3.7 shows the simulated correlations.

In deriving the beam energy distribution, the effect of straggling was taken into account. The energy spread due to the straggling is approximately 0.5%. In addition, to obtain a more accurate distribution, the correlations between F5X and the beam energy were evaluated at positions corresponding 1/6, 3/6, 5/6 of the SHT thickness, and their average was taken. The resulting beam energy distribution is shown in Fig. 3.8.

3.1.4 Beam injection angle and position on the target

The trajectory of the beam incident on the SHT was measured by the two BDCs. The angular resolution and position resolution on the SHT were 0.2 mrad and 0.2 mm (σ),

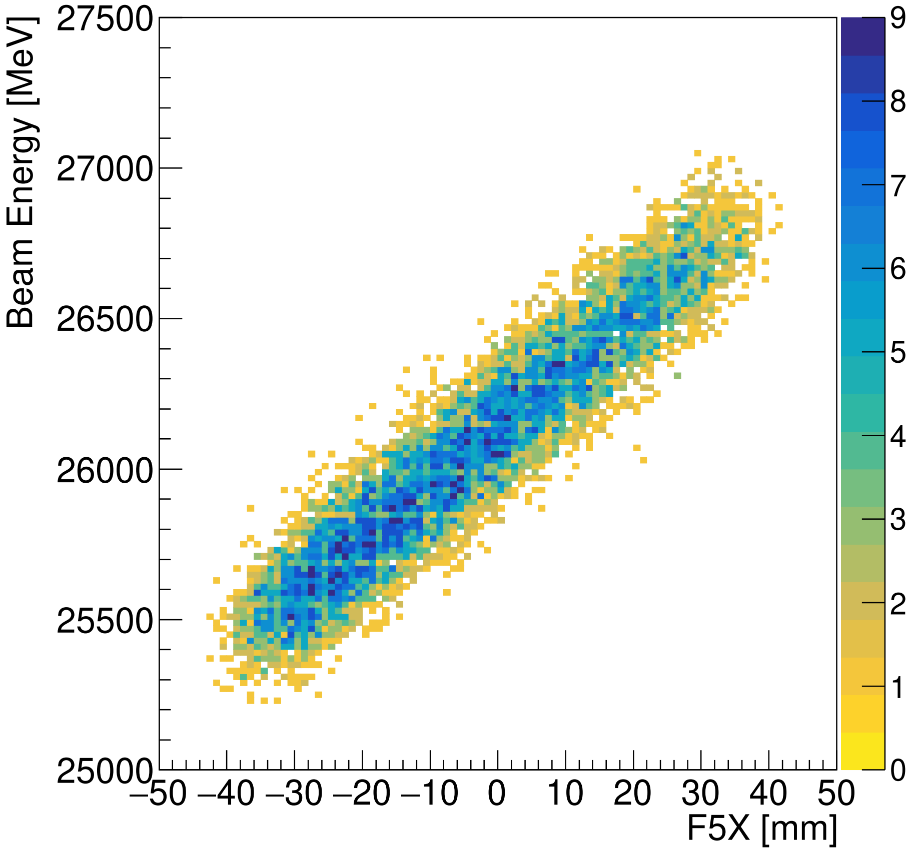

Figure 3.7: Simulated correlation between F5X and beam energy on the SHT by Lise++.

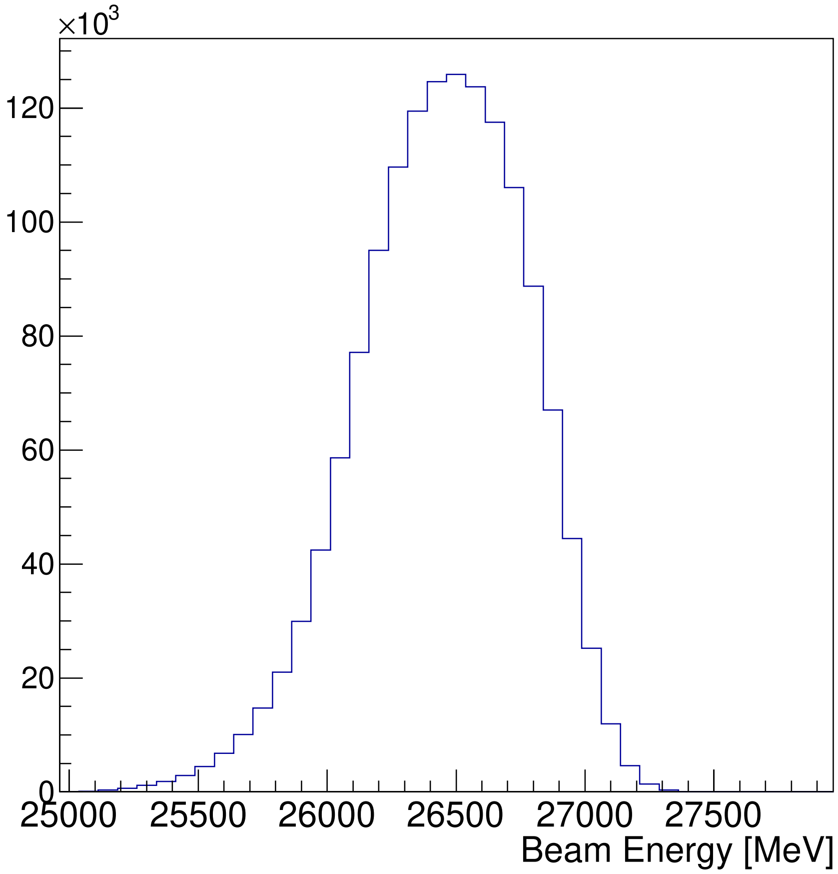

Figure 3.8: Beam energy distribution on the SHT.

respectively. The beam profile at the SHT is shown in Fig. 3.9. In the figure for the recoil trigger, the concentric circular region around ϕ25 mm indicates the edge of the copper frame. In this analysis, events within the ϕ21 mm circle, shown by the black line, were regarded as beam hits on the target.

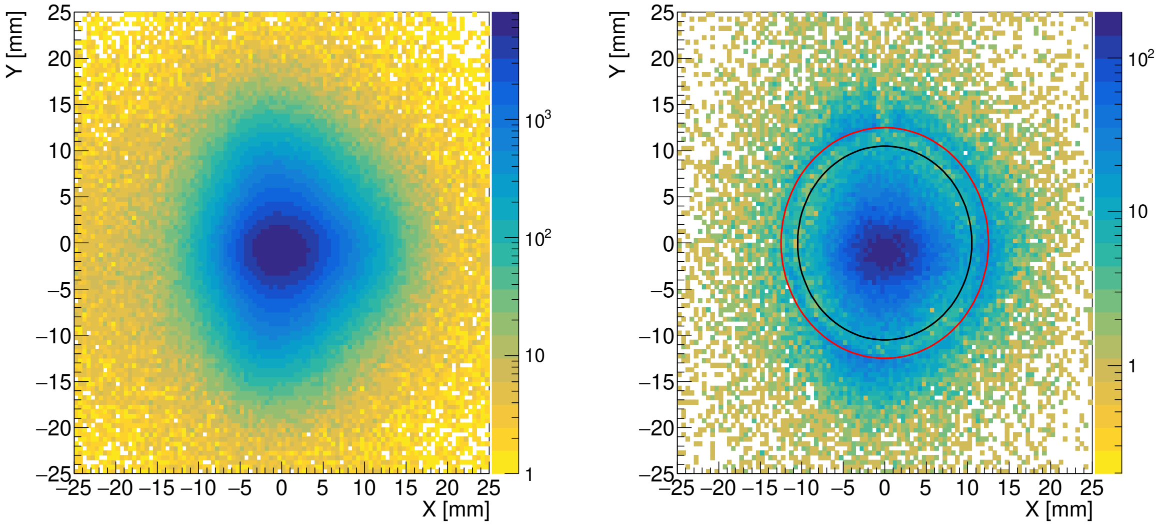

(a) Beam trigger.

(b) Recoil trigger.

Figure 3.9: Beam profile on the target. The red line indicates a ϕ25 circle, corresponding to the SHT size, while the black line indicates the ϕ21 circle, within which events were regarded as beam hits.

3.2 Recoil proton analysis

In this section, the analysis of recoil particles is presented using the recoil-trigger data, focusing on events with the target hit.

3.2.1 Recoil particle identification

The identification of the recoil particles was performed using the correlation between the energy loss in $p\Delta E$ and the TOF from F12pla to $p\Delta E$. In addition, for high-energy particles that penetrated the $p\Delta E$ and stopped in the NaI(Tl) calorimeter, the correlation between the energy loss in $p\Delta E$ and that in the calorimeter was used.

PID by the $p\Delta E$ detector

The PID was performed based on the correlation between the charge of the $p\Delta E$ ($Q_{p\Delta E}$) and the TOF from F12pla to $p\Delta E$ ($t_{p\Delta E} - t_{12}$). The TOF from F12pla to the SHT was assumed to be constant.

Figure 3.10 shows the correlation between $Q_{p\Delta E}$ and $(t_{p\Delta E} - t_{12})$. In the small TOF region (35–45 ns), corresponding to particles penetrating $p\Delta E$, $Q_{p\Delta E}$ follows the relation of $Q_{p\Delta E} \propto \frac{dE}{dx} \propto \frac{Z_r^2}{\beta_r^2}$, where Z_r and β_r denote the atomic number and velocity of the particles, respectively. On the other hand, in the large TOF region (45–60 ns), corresponding to particles stopping in $p\Delta E$, the light yield $Q_{p\Delta E}$ is related to the kinetic energy K_r as

$$\begin{aligned} Q_{p\Delta E} \propto K_r &= \frac{m_r}{\sqrt{1-\beta_r^2}} - m_r \\ &\approx \frac{1}{2} m_r c^2 \beta_r^2, \end{aligned} \tag{3.6}$$

where m_r and c denote the particle mass and the speed of light, respectively. Based on these correlations, the spectrum was fitted with the following function:

$$f_{\mathrm{PI1}}(x) = \begin{cases} p_0 \times f_{\mathrm{low}}(x) & (x \leq p_1) \\ p_0 \times f_{\mathrm{high}}(x) & (x > p_1) \end{cases}, \tag{3.7}$$

$$f_{\mathrm{low}}(x) = \left(\frac{x - p_2}{p_1 - p_2}\right)^2 + p_4(x - p_1), \tag{3.8}$$

$$f_{\mathrm{high}}(x) = \left(\frac{p_1 - p_3}{x - p_3}\right)^2 + p_5(x - p_1)^2, \tag{3.9}$$

where p_i are fitting parameters. The second term in each of Eqs. (3.8), (3.9) represents a correction term. Figure 3.11 shows the spectrum of $Q_{p\Delta E}/f_{\mathrm{PI1}}(t_{p\Delta E} - t_{12})$. The peak around $Q_{p\Delta E}/f_{\mathrm{PI1}}(t_{p\Delta E} - t_{12}) = 1$ corresponds to protons. The fitting with the proton gate in Fig. 3.10 and the proton selection in Fig. 3.11 were iteratively performed until convergence. The red line in Fig 3.10 represents the final function $f_{\mathrm{PI1}}(x)$. From this point forward, events startfying

$$|Q_{p\Delta E}/f_{\mathrm{PI1}}(t_{p\Delta E} - t_{12}) - 1| \leq 0.36 \tag{3.10}$$

are identified as protons. This condition corresponds to the region within 3σ around the peak at $Q_{p\Delta E}/f_{\mathrm{PI1}}(t_{p\Delta E} - t_{12}) = 1$, as determined by fitting the distribution with a Gaussian plus a linear background.

PID for high-energy recoil particle

For high-energy recoil particles, additional identification was performed using the E–ΔE method. Figure 3.12 shows the correlation between $Q_{p\Delta E}$ and the NaI ADC value, ADC_{NaI}. Assuming that energy losses outside $p\Delta E$ are negligible, ADC_{NaI} is related to the energy loss $\Delta E_{p\Delta E}$ inside $p\Delta E$ as follows:

$$\begin{aligned} ADC_{NaI} &\propto E_r - \Delta E_{p\Delta E} \\ &= C \frac{A_r Z_r^2}{\Delta E_{p\Delta E}} - \Delta E_{p\Delta E}, \end{aligned} \tag{3.11}$$

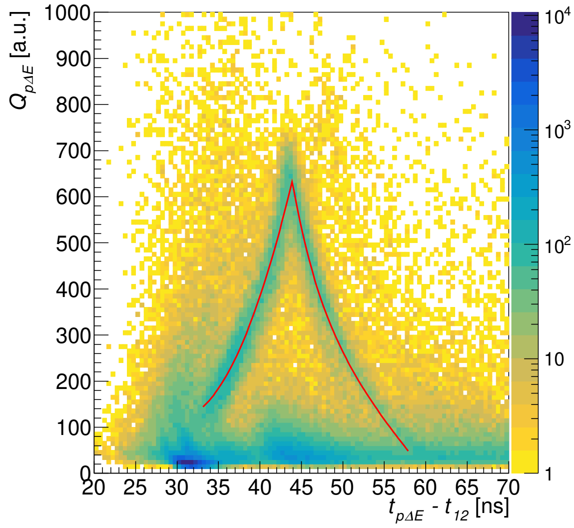

Figure 3.10: PID plot for recoil particles using $t_{p\Delta E} - t_{12}$ and $Q_{p\Delta E}$. The red line shows the fitting function in the form of Eq. (3.7).

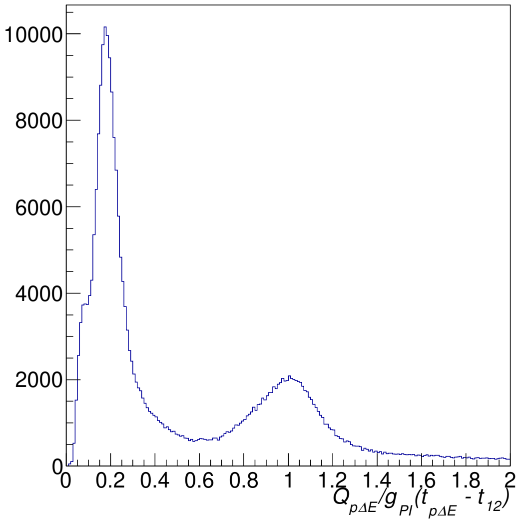

Figure 3.11: Spectrum of the ratio $Q_{\mathrm{p\Delta E}}/f_{\mathrm{PI1}}(t_{p\Delta E} - t_{12})$.

where E_r and A_r denote the particle energy and mass,respectively, and C is a constant. Accordingly, the spectrum was fitted using the following function:

$$f_{\mathrm{PI2}}(x) = \frac{1}{p_3}\Big(\frac{p_0}{p_1 + p_2 x} - (p_1 + p_2 x)\Big), \tag{3.12}$$

where p_i are fitting parameters. Figure 3.13 shows the spectrum of $A_r Z_r^2$, which was caculated using the fitted parameters as

$$A_r Z_r^2 = \frac{1}{p_0}(p_2 ADC_{NaI} + p_1 + p_2 x)(p_1 + p_2 x). \tag{3.13}$$

Events within 3σ around the peak at $A_r Z_r^2 = 1$, determined by fitting the distribution with a Gaussian plus a linear background, were identified as protons.

3.2.2 Scattering angle

The hit position on the RDC was determined by its tracking. The first X plane, being closest to the target and most affected by backgrounds, was excluded from the analysis. While the analysis procedure follows almost the same method described in Sec . 3.1.1, there are mainly two different points. One is that χ^2 is defined as

$$\chi^2 = \sum_i \Big(\frac{f(z_i) - x_i}{1 + A^2} - dl_i\Big)^2, \tag{3.14}$$

$$f(z) = X + Az, \tag{3.15}$$

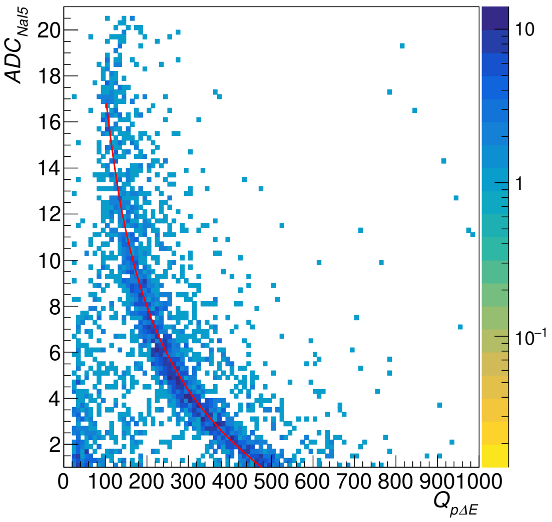

Figure 3.12: PID plot for recoil particles using $Q_{p\Delta E}$ and ADC_{NaI5} The red line shows the fitting function in the form of Eq. (3.12).

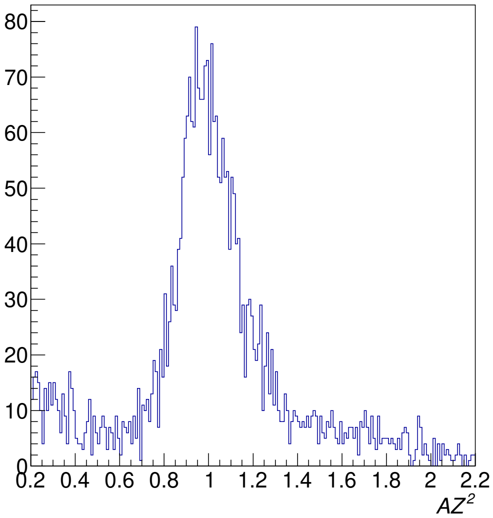

Figure 3.13: $A_r Z_r^2$ spectrum defined as Eq. (3.13).

to account for the effect of the relatively large incident angle with respect to the RDC. The other is that the STC function was iteratively corrected to determine a more precise position, which is described in Appendix B. The position resolution of the RDC was less than $0.2\,\mathrm{mm}(\sigma)$.

From the above analysis of the RDC, the hit position on the RDC $\boldsymbol{r}$ was obtained. Combining $\boldsymbol{r}$ with the target-hit postion $\boldsymbol{t}$, the recoil-proton direction $\vec{r} = (r_x, r_y, r_z)$ was reconstructed as $\vec{r} = \boldsymbol{r} - \boldsymbol{t}$. Furthermore, using the beam direction $\vec{b}$ obtained by the BDCs, the scattering angle of the proton (polar angle θ_{lab} and azimuthal angle ϕ_{lab}) in the laboratory frame was determined as

$$\theta_{\mathrm{lab}} = \arccos\left(\frac{\vec{b}\cdot\vec{p}}{|\vec{b}||\vec{p}|}\right), \tag{3.16}$$

$$\phi_{\mathrm{lab}} = \arctan\left(\frac{r_y}{r_x}\right). \tag{3.17}$$

$$\tag{3.18}$$

3.2.3 Recoil energy calibration and kinematical correlation

In this section, the energy calibration procedure for the recoil proton is described. In the analysis, recoil-trigger data were used, with requirements of the target hit and ^{132}Sn selection. The recoil-proton energy was determined by the TOF for low-energy particles and by the ADC_{NaI} for high-energy particles. The calibration was based on the proton energies T_p[kin] of elastic events, which were deduced from the beam energy T_b and scattering θ_{lab} using the kinematical correlation obtained by solving Eq. (2.11):

$$T_p = \frac{2(2m_b + T_b)m_p T_b \cos^2\theta_{\mathrm{lab}}}{(m_b + T_b + m_p)^2 - (2m_b + T_b)T_b \cos^2\theta_{\mathrm{lab}}}. \tag{3.19}$$

NaI(Tl) calorimeter

The energy calibration of the NaI(Tl) detector was performed individually for each spectrum. Although the detector exhibits position dependence, namely, the measured ADC values vary with the incident position even for the same incident energy [79], no explicit correction for this effect was applied. Consequently, the calibration implicitly includes this position dependence correction. To reduce background contributions, the corresponding region was selected using the RDC. Figure 3.14 shows the correlation between ADC_{NaI} and T_p[kin]. Elastic events were graphically selected and fitted with the following function:

$$f_{Tp}^{\mathrm{NaI}}(x) = p_{1/2}\sqrt{x} + p_0 + p_1 x + p_2 x^2 + p_3 x^3. \tag{3.20}$$

ToF

The calibrated proton TOF (TOF_p) was expressed as

$$TOF_p = (t_{p\Delta E} - t_{12}) - t_{\mathrm{off}}. \tag{3.21}$$

The ideal TOF (TOF_p[kin]), which was calculated from the T_p[kin] and did not include effects such as energy loss inside the target, was given by

$$TOF_p[\mathrm{kin}] = \frac{L_p}{c}\frac{\gamma}{\sqrt{\gamma^2 - 1}}, \tag{3.22}$$
$$\gamma = \left(\frac{T_p[\mathrm{kin}]}{m_p c^2} + 1\right),$$

where L_p is the flight path length determined from the positions at the target and at the RDC. The offset parameter t_{off} was calibrated so that the measured TOF reproduces this ideal TOF. Since t_{off} reflects not only the difference in signal path length but also the effects of energy loss in the target, it is not constant. Figure 3.15 shows the correlation between $(t_{p\Delta E} - t_{12})$ and $t_{\mathrm{off}} = TOF_p[(\mathrm{kin})]$ - $(t_{p\Delta E} - t_{12})$, where elastic events were graphyically selected. In addition, it is required that the absolute value of the excitation energy E_x determined from the NaI(Tl) calorimeters was less than 3 MeV in the region of $(t_{p\Delta E} - t_{12}) < 42$ ns. This spectrum was fitted using a fourth-order polynomial function, which was then used to obtain the proton energy T_p.

Figure 3.16 shows the two-dimensional plots between the scattering angle θ_{lab} and energies of the recoil protons. The proton energies T_p in Fig. 3.16(a) and Fig. 3.16(b) were deduced from the NaI(Tl) calorimeters and the TOF, respectively. The black and red lines are the kinematical correlation of the elastic scattering and inelastic scattering to the first excited state (4.04 MeV) for $T_b = 26730$ MeV.

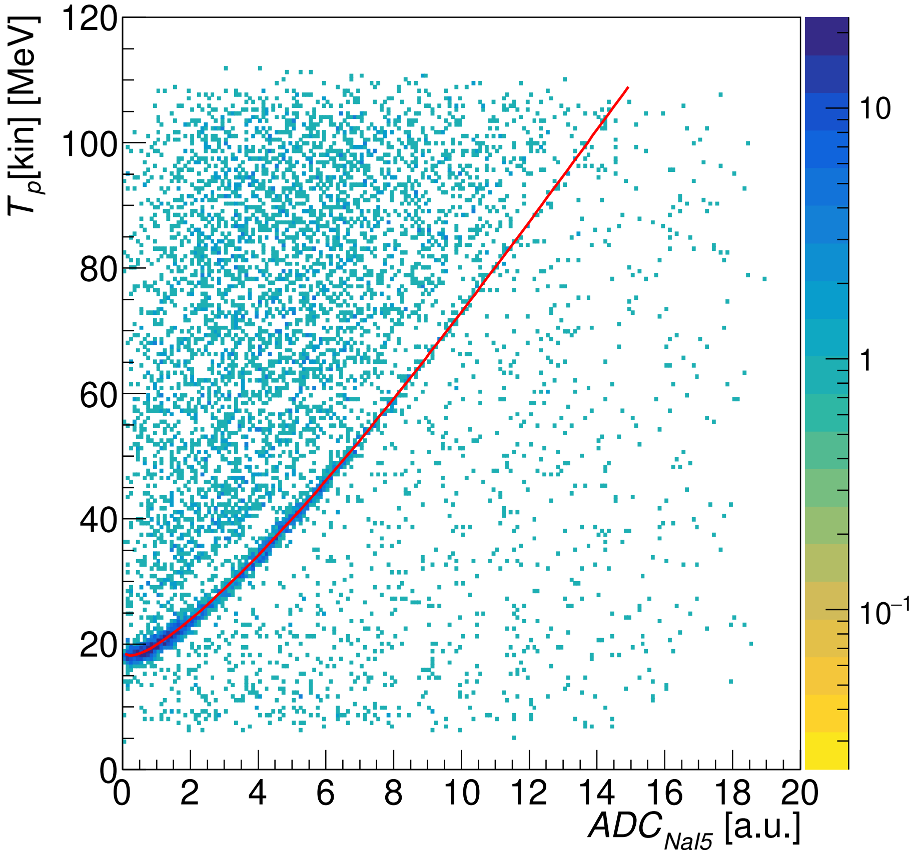

Figure 3.14: 2D specturm of ADC_{NaI5} versus T_p[kin] The red line shows the fitting function in the form of Eq. (3.20).

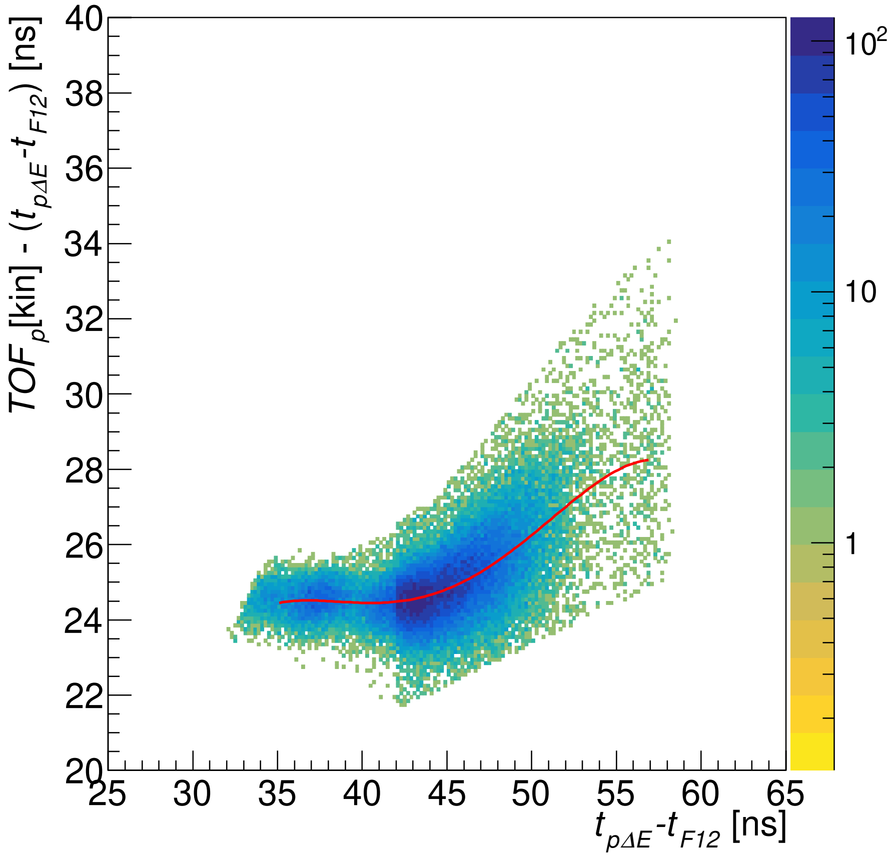

Figure 3.15: 2D spectrum of $(t_{p\Delta E} - t_{12})$ versus $t_{\text{off}} = TOF_p$[kin] - $(t_{p\Delta E} - t_{12})$. In the region of $(t_{p\Delta E} - t_{12}) < 42\,\text{ns}$, the elastic events were selected using the NaI(Tl) calorimeters. The red line shows the fitting function in the form of a fourth-order polynomial function.

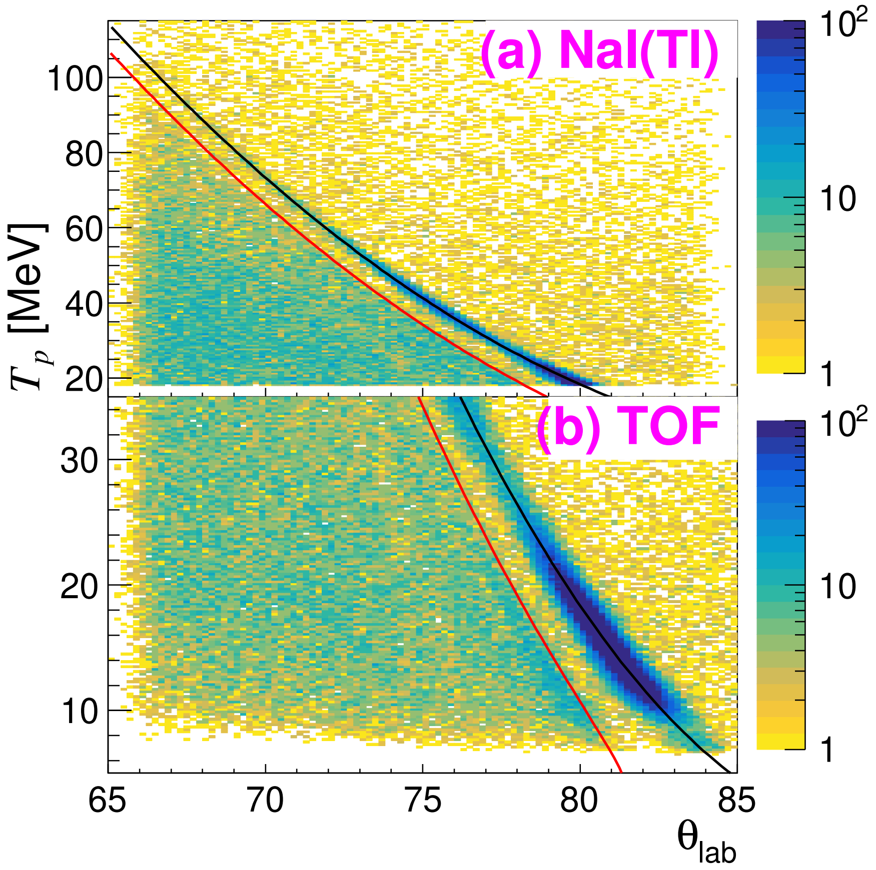

Figure 3.16: Correlation between the angle and energy for recoil protons. The energies are determined using NaI(Tl) calorimeters (top panel) and the TOF (bottom panel), respectively. The black and red lines indicate the kinematical correlation of the elastic scattering and inelastic scattering to the first excited state (4.04 MeV) at $T_b = 26700\,\mathrm{MeV}$.

3.2.4 Conversion to the CM frame

The scattering angle θ_{lab} in the laboratory frame was event-by-event converted to the scattering angle θ_{cm} in center-of-mass (CM) frame by the following equation:

$$\theta_{\mathrm{cm}} = \arcsin \frac{m_p \sqrt{m_p^2 + p_{\mathrm{cm}}^2} \sin 2\theta_{\mathrm{lab}}}{m_p^2 + p_{\mathrm{cm}}^2 \sin^2 \theta_{\mathrm{lab}}}, \tag{3.23}$$

$$p_{\mathrm{cm}} = \sqrt{\frac{(s - m_p^2 - m_b^2) - 4m_b^2 m_p^2}{4s}}, \tag{3.24}$$

$$s = (m_p + m_b)^2 + 2m_p T_b. \tag{3.25}$$

$$\tag{3.26}$$

3.3 Excitation energy and count of elastic events

The excitation energy E_x can be determined from Eq. (2.11), solved for E_x, using T_b, T_p, and θ_{lab} obtained in the previous sections, as follows:

$$E_x = -m_b + \sqrt{m_b^2 - 2(m_b + T_b + m_p) + 2A \cos \theta_{\mathrm{lab}}}, \tag{3.27}$$

$$A = \sqrt{(2m_b + T_b)m_b(2m_p + T_p)m_p}.$$

Figures 3.17 show the correlations between θ_{cm} and E_x, obtained from the ADC of the NaI(Tl) calorimeters and the TOF, respectively. Representative E_x spectra are presented in Figs. 3.18a and 3.18b. The vertical lines at θ_{cm} show the limitation of the acceptance of the RDC, while the slanted lines in the forward region show the limitations by the detection threshold of the NaI(Tl) calorimeters in Fig. 3.17b and by that of $p\Delta E$ in Fig. 3.17a. The peaks around $E_x = 0$ correspond to elastic events. The elastic yields y_i (where i denotes the central scattering angle of each bin) were extracted at every 1-degree step of the scattering angle θ_{cm} in the CM frame, following the procedure described below.

For the TOF analysis, the elastic peak at each angle was fitted with a Gaussian plus a constant function. The yield y_i was obtained by counting the number of events within 3σ of the Gaussian and subtracting the background contribution estimated from the constant term.

For the NaI analysis, the elastic yield was determined for each rod individually. Since the statistics were insufficient to perform fits in every angular bin, the data were grouped into four regions: $\theta_{\mathrm{cm}} < 25°$, $25° < \theta_{\mathrm{cm}} < 30°$, $30° < \theta_{\mathrm{cm}} < 35°$, and $35° < \theta_{\mathrm{cm}}$. In each region, the spectra were fitted with a Gaussian plus a constant function. The yields were then obtained by counting events within 3σ of the Gaussian, while the background contribution was evaluated for each angular bin from the counts in the region $E_x < -3\,\mathrm{MeV}$. Finally, the values from all seven rods were summed to obtain the total yield y_i.

Figure 3.19 shows the distribution of the obtained yields.

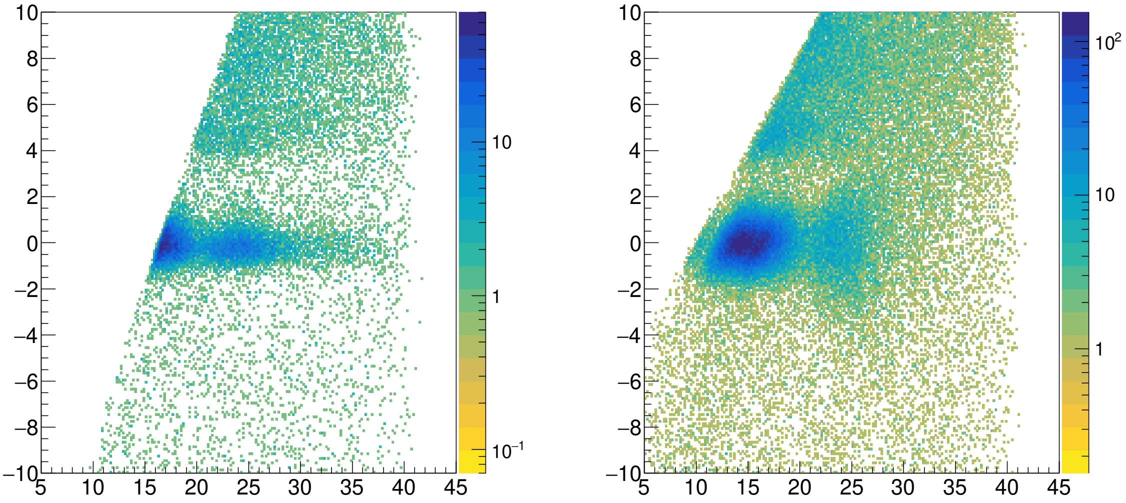

(a) NaI(Tl).

(b) TOF.

Figure 3.17: Angular dependence of the excitation energy.

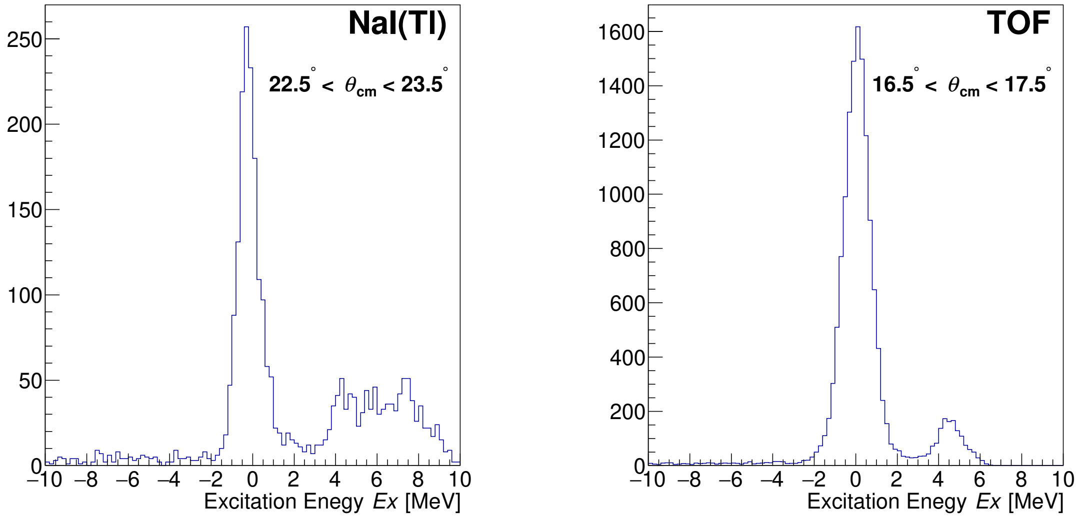

(a) NaI(Tl).

(b) TOF.

Figure 3.18: Typical excitation energy spectrum.

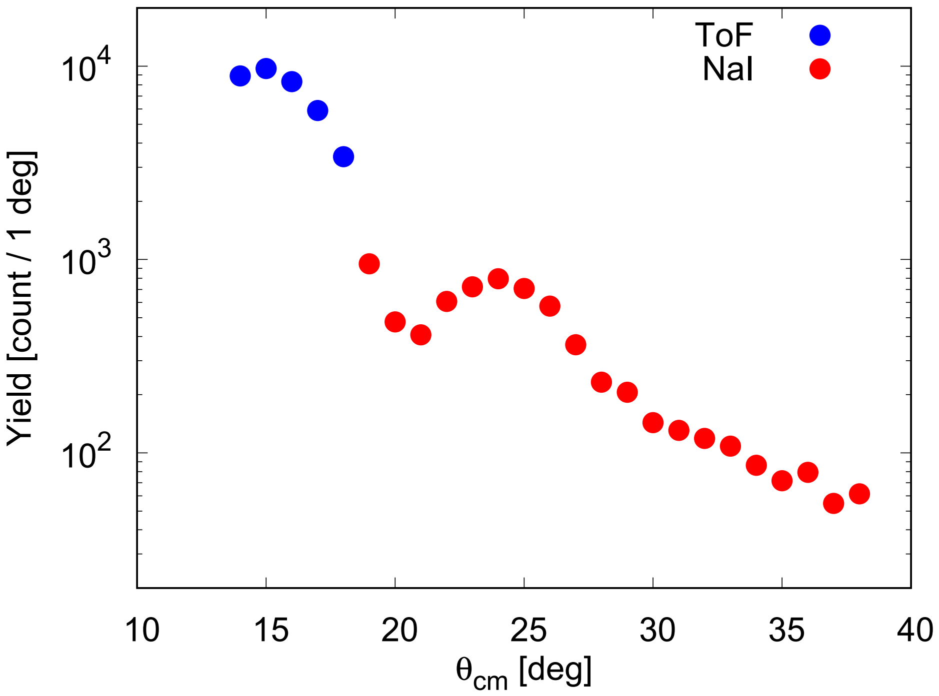

Figure 3.19: Angular dependence of elastic yields. The blue and red points are data using TOF and NaI(Tl) for proton energies, respectively.

3.4 Derivation of differential cross section

The yield y_i can be expressed as

$$y_i = \epsilon_0 I_{\mathrm{beam}} N_{\mathrm{tgt}} \int_{\Delta\Omega_i} d\Omega \epsilon(\theta) \left(\frac{d\sigma}{d\Omega}\right), \tag{3.28}$$

where ϵ_0, I_{beam}, N_{tgt}, $\Delta\Omega$, $\epsilon(\theta)$, and $\frac{d\sigma}{d\Omega}$ denote the angle-independent efficiency, the number of beam particles, the number of target particles, the effective solid angle, the angle-dependent efficiency, and the differential cross section, respectively. The $\epsilon(\theta)$ was assumed to be constant within each angular bin, i.e. $\epsilon(\theta) = \epsilon_i$ for $\theta_i - \Delta\theta/2 < \theta_{\mathrm{cm}} < \theta_i - \Delta\theta/2$, with $\Delta\theta = 1^\circ$. In the experiment, the differential cross section $\frac{d\sigma}{d\Omega}$ for an infinitesimal solid angle cannot be directly determined. Therefore, we evaluated the averaged differential cross section $\overline{(\frac{d\sigma}{d\Omega})}$, defined as

$$\overline{\left(\frac{d\sigma}{d\Omega}\right)}_i = \frac{\int_{\Delta\Omega_i} d\Omega \left(\frac{d\sigma}{d\Omega}\right)}{\int_{\Delta\Omega_i} d\Omega}. \tag{3.29}$$

Assuming that the azimuthal coverage within each angular bin is a constant value $\Delta\phi_i$, the denominator can be expressed as:

$$\begin{aligned}\int_{\Delta\Omega_i} d\Omega &= \int_{\theta_i-\Delta\theta/2}^{\theta_i+\Delta\theta/2} d\theta \sin\theta \int d\phi \\ &\simeq \Delta\phi_i \int_{\theta_i-\Delta\theta/2}^{\theta_i+\Delta\theta/2} d\theta \sin\theta \\ &= \Delta\phi_i \Big(\cos(\theta_i - \Delta\theta/2) - \cos(\theta_i + \Delta\theta/2) \Big). \end{aligned} \tag{3.30}$$

Thus, Eq. (3.28) can be rewriten as:

$$y_i = \epsilon_0 I_{\mathrm{beam}} N_{\mathrm{tgt}} \epsilon_i \Delta\phi_i \Big(\cos(\theta_i - \Delta\theta/2) - \cos(\theta_i + \Delta\theta/2) \Big) \overline{\left(\frac{d\sigma}{d\Omega}\right)_i}. \tag{3.31}$$

In the following sub-sections, we describe the procedures used to evaluate the values of ϵ_0, I_{beam}, N_{tgt}, ϵ_i, and $\Delta\phi_i$, as well as the obtained cross sections.

3.4.1 Angular-independent efficiency ϵ_0

The angular-independent efficiency ϵ_0 consists of three components: the efficiency of the BLDs at F12, the efficiency of the detectors at F3, F5, and F7, and the DAQ efficiency.

- **Efficiency of the BLDs at F12**
  The efficiency of the BLDs (F12pla and BDCs) at F12 was evaluated using the beam-trigger data. The efficiency includes not only intrinsic detector efficiencies but also transmission efficiency from F7 to F12. The evaluated efficiency is 87.5%.

- **Efficiency of the detectors at BigRIPS**
  The efficiency of the detectors at BigRIPS was evaluated using the beam-trigger data. It is defined as the ratio of events in which the beam particles are detected by all detectors and all tracks are successfully reconstructed, to the number of events in which the beam particles hit the SHT. The evaluated value is 90.9%.

- **DAQ efficiency**
  The DAQ efficiency was evaluated by considering not only the ratio of accepted triggers to requested triggers but also the merge efficiency of the BLD-builder data and ESPRI-builder data. The resulting value was 92.2%.

As a result, the angle-independent efficiency ϵ_0 was evaluated to be 72.7%. Table 3.1 summarizes the values used for the evaluation together with ϵ_0.

3.4.2 Effective number of beam I_{beam}

The number of beam particles I_{beam} was evaluated based on the scaler counts of the F7Dia signal used for the beam trigger. In addition, we considered the conditions of the scaler count loss, target hit rate, and purity of ^{132}Sn.

Table 3.1: Values of angle-independent efficiency ϵ_0 and its components.

BLDs at F12	87.5%
Detecros at BigRIPS	90.1%
DAQ	92.2%
Angle-independent efficiency ϵ_0	72.7%

- **Scaler count loss**
  Events that occurred within a very short time interval were lost in the scaler. Since the width of the discriminator signal from F7dia was 17 ns and the averaged beam intensity was 196 kcps, 0.33% of the events were missed.

- **Target hit rate**
  The ratio of events in which the beam particles hit the SHT to those in which trackings were reconstructed using the BDCs was evaluated using the beam-trigger data. As described in Sec. 3.1.4, hits within a ϕ21 mm circle were defined as target hits. The evaluated ratio is 92.5%.

- **Purity of ^{132}Sn**
  The purity of ^{132}Sn was evaluated as the ratio of events that satisfied Eq. (3.5) to those in which all BLD detectors worked well and the beam particles hit the SHT. The resulting value was 27.8%.

As a result, the number of beam particles I_{beam} was evaluated to be 7.94×10^9. Table 3.2 summarizes the values used for the evaluation together with the number of beam particles.

Table 3.2: Number of beam particles (I_{beam}) and values for its calculation.

Counts of F7Dia	3.08×10^{10} [particle]
Scaler count loss	0.33%
Target hit rate	92.5%
Purity of ^{132}Sn	27.8%
Number of beam praticles (I_{beam})	7.94×10^{9} [particle]

3.4.3 Number of target particles N_{tgt}

The number of target particles was evaluated from the cross section of proton elastic scattering from ^{48}Ca. The analysis for ^{48}Ca was performed using almost the same procedure as that for ^{132}Sn. The details of the analysis are described in Appendix C.

The angular distribution of the obtained cross section was compared with a theoretical prediction from a medium-modified relativistic impulse approximation (mm-RIA) calculation with the realistic density [26, 24]. The mm-RIA calculation is explained in Chap.4. The absolute calibration factor was estimated to be 1.13(5), corresponding to a proton number of $6.76(35) \times 10^{21}$ and an STH thickness of 0.88(4) mm. Figure 3.20 shows the mm-RIA calculation for the proton elastic scattering from ^{48}Ca at 224 to 244 MeV, together with the calibrated experimental data.

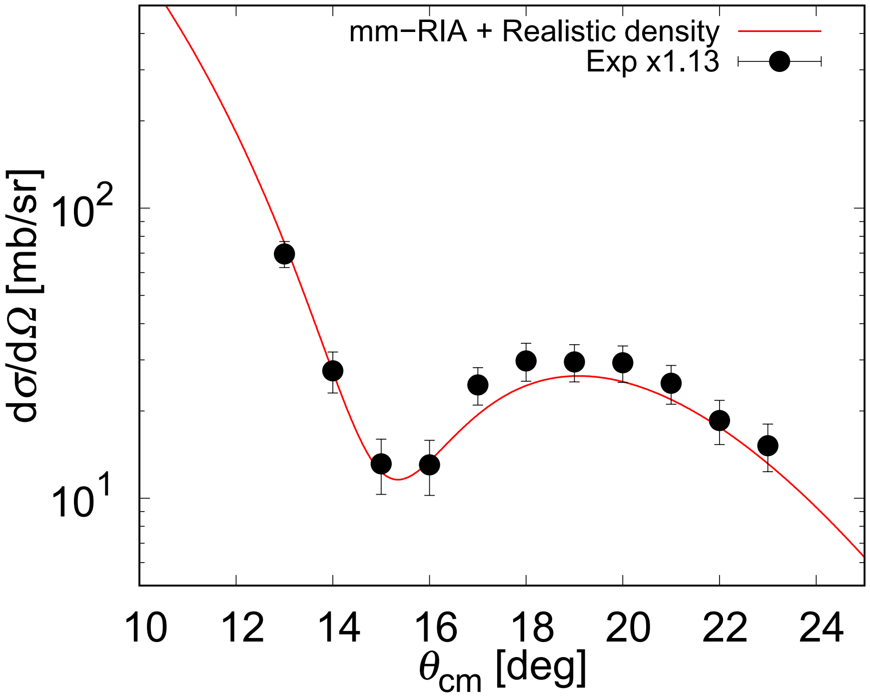

Figure 3.20: Differential cross section for proton elastic scattering from ^{48}Ca. The experimental data points, obtained from calculations based on a target number corresponding to a thickness of $1 \times \sqrt{2}$ mm, were scaled by a calibration factor of 1.13. The red line shows the mm-RIA with the realistic density [26, 24].

3.4.4 Angular-dependent efficiency ϵ_i

The angular-dependent efficiency ϵ_i consists of two components: the RDC efficiency and the reaction loss in the detectors.

- **RDC efficiency**
  The RDC efficiency was evaluated using the event identified as protons. For the evaluation, it was necessary to determine the scattering angle without relying on the RDC. Therefore, the angle was obtained from the time difference between the signals from the left and right PMTs of the $p\Delta E$ detector, $t^R_{p\Delta E}-t^L_{p\Delta E}$. Figure 3.21 shows the correlation between $t^R_{p\Delta E}-t^L_{p\Delta E}$ and the scattering angle $\theta_{\rm lab}$ determined by the RDC, where the spectrum was fitted by a linear function. Using the function, $t^R_{p\Delta E} - t^L_{p\Delta E}$ was converted to the scattering angle $\theta_{\rm lab}$, and the efficiency was evaluated in 1-degree steps of the scattering angle $\theta_{\rm lab}$ in the laboratory frame. Furthermore, the efficiency in 1-degree steps of scattering angle $\theta_{\rm cm}$ in the CM frame was obtained by

linear interpolation, using θ_{lab} converted from θ_{cm} at the average beam energy. The resulting values are shown in Fig. 3.22.

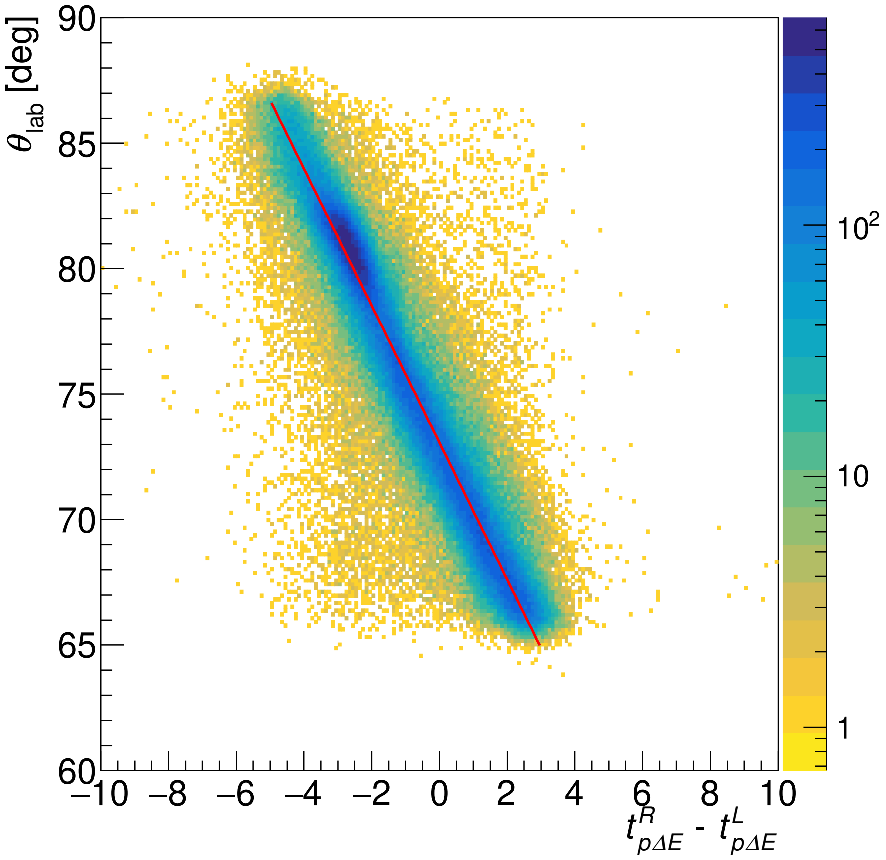

Figure 3.21: Correlation between $t^{R}_{p\Delta E} - t^{L}_{p\Delta E}$ and scattering angele θ_{lab}.

- **Raction loss**
  If a proton undergoes a nuclear reaction before coming to rest, the $p\Delta E$ or NaI(Tl) calorimeters cannot yield a light output corresponding to the proton energy at the reaction point. This effect, known as a reaction loss, becomes increasingly probable at higher energies. The reaction-loss probabilities for $p\Delta E$ and NaI(Tl) calorimeters were evaluated using the values reported in Ref. [80] and Ref. [81], respectively.

3.4.5 Azimuthal coverage $\Delta\phi_i$

The azimuthal coverage $\Delta\phi_i$ was evaluated based on the geometrical configuration of the RPS system, taking the beam profile into account. Since it is difficult to determine the exact hardware positions at the edges, the accepted region was constrained by the positions deduced by the RDC. Although $\Delta\phi_i$ has a position dependence, the values are approximately 0.29 rad for TOF data and approximately 0.18 rad for NaI data.

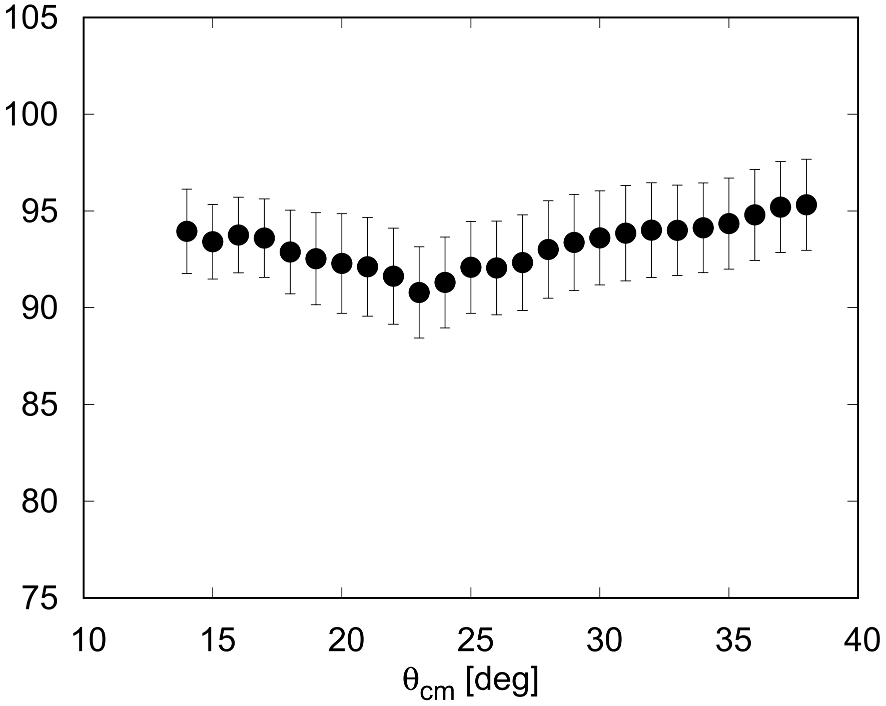

Figure 3.22: Efficiency of RDC.

3.4.6 Result

Figure 3.23 shows the angular distribution of the obtained cross sections over an angular range of $14^\circ < \theta_{\mathrm{cm}} < 38^\circ$, corresponding to a momentum range of 0.80 to $2.1\,\mathrm{fm}^{-1}$. The main components of the errors in the forward and backward regions were the uncertainty of the target number and the statistical uncertainty, respectively. The digital data are listed in Appendix A.

3.4.7 Smearing effect of the scattering angle

It should be noted that the scattering angle was smeared due to angular straggling, mainly caused by the multiple scattering in the SHT. The effect was particularly significant at forward angles in the CM frame. Similar to the beam energy spread, the angular smearing significantly affects the cross section. We calculated the response function f_{ij}^{ang}, defined as the fraction of events with the true reaction angle $\theta^{\mathrm{react.}}$ of the reaction in the i-th bin and the detected scattering angle θ^{det} in the j-th bin. The values of f_{ij}^{ang} larger than 1% are summarized in Table 3.3. In the next section, we use this function when comparing the experimental data with theoretical calculations.

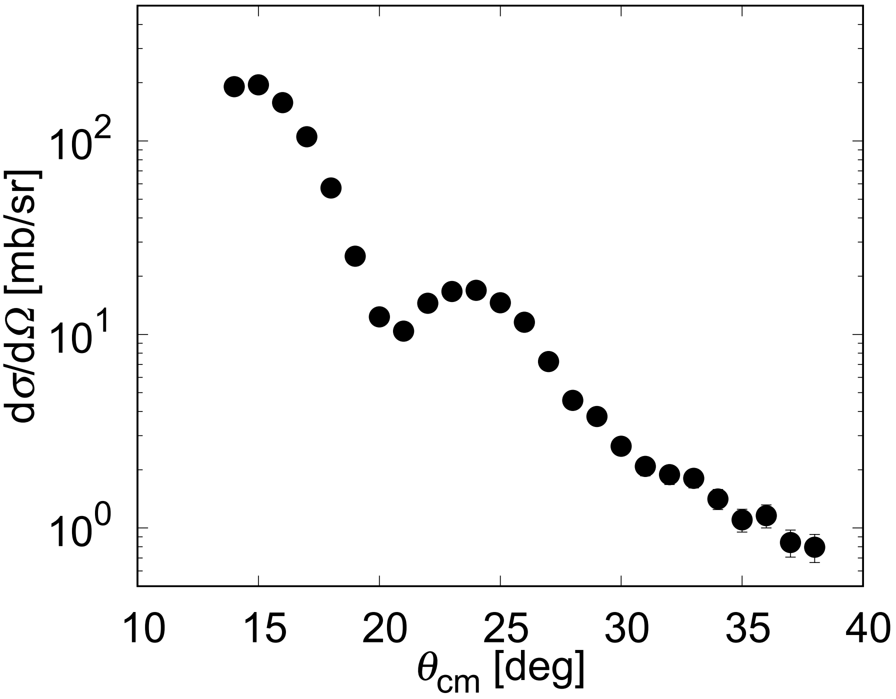

Figure 3.23: Obtained differential cross sections for proton elastic scattering from ^{132}Sn at 196–210 MeV/nucleon.

Table 3.3: Values of the response function f_{ij}^{ang}. $\theta_i^{\mathrm{react.}}$ denotes the central reaction angle of the i-th bin, while $\theta_i^{\mathrm{react.}}$ denotes the central detection angle of the j-th bin.

$\theta_i^{\mathrm{react.}}$	$\theta_j^{\mathrm{det.}}$	f_{ij}^{ang}	$\theta_i^{\mathrm{react.}}$	$\theta_j^{\mathrm{det.}}$	f_{ij}^{ang}
13	12	0.077	22	22	1.000
13	13	0.846	23	23	1.000
13	14	0.077	24	24	1.000
14	13	0.050	25	25	1.000
14	14	0.899	26	26	1.000
14	15	0.050	27	27	1.000
15	14	0.031	28	28	1.000
15	15	0.939	29	29	1.000
15	16	0.031	30	30	1.000
16	15	0.018	31	31	1.000
16	16	0.965	32	32	1.000
16	17	0.018	33	33	1.000
17	17	0.981	34	34	1.000
18	18	0.991	35	35	1.000
19	19	0.996	36	36	1.000
20	20	0.998	37	37	1.000
21	21	0.999	38	38	1.000

Chapter 4

Analysis

Our analysis is based on the framework of the relativistic impulse approximation (RIA) with relativistic Love-Franey (RLF) interactions [82], which was formulated by Murdock and Horowitz [83].

4.1 Relativistic impulse approximation

One of the notable achievements in the application of the RIA to nucleon-nucleus scattering was made by McNeil, Ray, and Wallace [84, 85]. The McNeil-Ray-Wallace (MRW) model involves two important steps. First, the nucleon-nucleon (NN) scattering amplitude $\mathcal{F}$ is represented in terms of five Lorentz covariants, so-called Fermi invariant Dirac matrices as

$$\mathcal{F} = \mathcal{F}^S + \mathcal{F}^V \gamma^{\mu}_{(0)} \gamma_{(1)\mu} + \mathcal{F}^{PS} \gamma^5_{(0)} \gamma^5_{(1)} + \mathcal{F}^T \sigma^{\mu\nu}_{(0)} \gamma_{(1)\mu\nu} + \mathcal{F}^A \gamma^5_{(0)} \gamma^{\mu}_{(0)} \gamma^5_{(1)} \gamma_{(1)\mu}, \tag{4.1}$$

where $\mathcal{F}^S$, $\mathcal{F}^V$, $\mathcal{F}^{PS}$, $\mathcal{F}^T$, $\mathcal{F}^A$ denote the scalar, vector, tensor, pseudoscalar, and axial vector amplitudes, and subscripts (0) and (1) represent the incident and struck nucleons, respectively. The amplitude was then folded with densities of target nuclei to provide a first-order $t\rho$ potential.

Murdock-Horowitz model

Murdock and Horowitz developed the RIA model [83] based on the MRW models by introducing the relativistic Love-Franey (RLF) interaction [82]. In the Murdock-Horowitz (MH) model, the NN scattering amplitude is modelled as arising from the first Born approximation for the exchange of a set of mesons. Since each scattering amplitude $\mathcal{F}^L$ ($L = S, V, PS, T,$ or A) in Eq. (4.1) is a function of the momentum transfer q, and laboratory energy E, Eq. (4.1) can be written as

$$\mathcal{F} = \sum_L \mathcal{F}^L(q, E) \lambda^L_{(0)} \cdot \lambda^L_{(1)}, \tag{4.2}$$

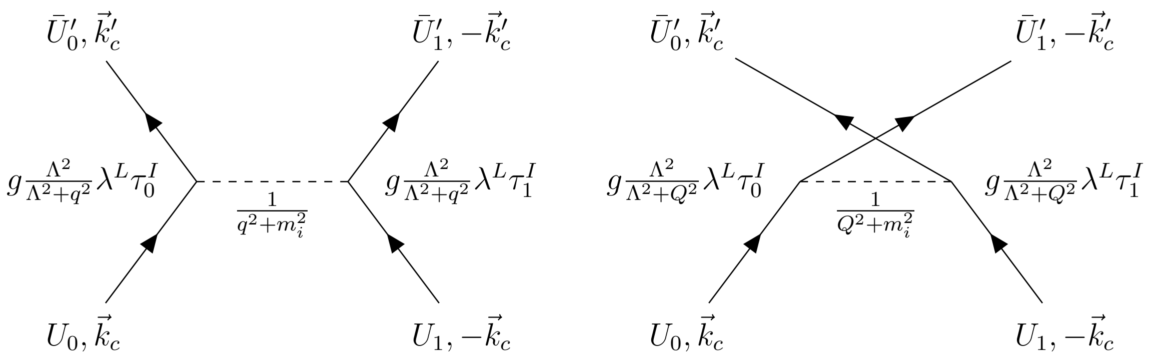

(a) Direct (b) Exchange

Figure 4.1: Meson exchange diagram for the RLF model.

where the $\lambda^L_{(i)}$ stand for Dirac operators for the Lorentz type. In this model, direct and exchange terms are separately included, and their Feynman diagrams are shown in Fig. 4.1.

Each scattering $\mathcal{F}^L$ can be witten as:

$$\mathcal{F}^L(q,E) = i\frac{M^2}{2E_c k_c}\Big[F_D(q) + F_X(q)\Big], \tag{4.3}$$

$$F^L_D(q) \equiv \sum_i \delta_{L,L(i)}\{\boldsymbol{\tau}_0\cdot\boldsymbol{\tau}_1\}^{I_i} f^i(q), \tag{4.4}$$

$$F^L_X(Q) \equiv (-1)^T \sum_i B_{L(i),L}\{\boldsymbol{\tau}_0\cdot\boldsymbol{\tau}_1\}^{I_i} f^i(Q), \tag{4.5}$$

$$f^i(q) \equiv \frac{g_i^2}{\boldsymbol{q}^2+m_i^2}\left(\frac{\Lambda_i^2}{\Lambda_i^2+\boldsymbol{q}^2}\right)^2 - i\frac{\overline{g}_i^2}{\boldsymbol{q}^2+\overline{m}_i^2}\left(\frac{\overline{\Lambda}_i^2}{\overline{\Lambda}_i^2+\boldsymbol{q}^2}\right)^2. \tag{4.6}$$

Here, D and X denote the direct and exchange terms, q and Q are direct and exchange momentum transfers, and T is the total isospin of the two-nucleon state. I_i, g_i, m_i, and Λ_i are the isospin, coupling constant, mass, and cutoff parameter of the i-th meson, respectively. $B_{L,L'}$ is the (L, L') component of the Fietz trasformation matrix as:

$$B_{L,L'} = \frac{\mathrm{tr}(\lambda^L\lambda^{L'}\lambda^L\lambda^{L'})}{\Big[\mathrm{tr}(\lambda^L\lambda^{L'})\Big]^2} \tag{4.7}$$

$$= \frac{1}{8}\begin{pmatrix} 2 & 2 & 1 & -2 & 2 \\ 8 & -4 & 0 & -4 & -8 \\ 24 & 0 & -4 & 0 & 24 \\ -8 & -4 & 0 & -4 & 8 \\ 2 & -2 & 1 & 2 & 2 \end{pmatrix}\begin{pmatrix} S \\ V \\ T \\ A \\ PS \end{pmatrix}. \tag{4.8}$$

Furthermore, to give meaningful results at low energies, the pseudoscalar term in

Eq. (4.1) is replaced by the pseudovector term as

$$\mathcal{F}^{PS}\gamma^5_{(0)}\gamma^5_{(1)} \to -\mathcal{F}^{PV}\frac{q\gamma^5_{(0)}}{2M}\frac{q\gamma^5_{(1)}}{2M}. \tag{4.9}$$

The first-order Dirac optical potential for the spherical nuclei can be obtained by folding the NN amplitude $\mathcal{F}^L$ with the target

$$U^L(r,E) = U^L_D(r,E) + U^L_X(r,E), \tag{4.10}$$

$$U^L_D(r,E) \equiv -\frac{4\pi ip}{M}\int d\boldsymbol{r'}\rho'^L(\boldsymbol{r})\tilde{t}^L_D(|\boldsymbol{r'}-\boldsymbol{r}|,E), \tag{4.11}$$

$$U^X_D(r,E) \equiv -\frac{4\pi ip}{M}\int d\boldsymbol{r'}\rho'^L(\boldsymbol{r},\boldsymbol{r'})\tilde{t}^L_X(|\boldsymbol{r'}-\boldsymbol{r}|,E)j_0(p|\boldsymbol{r'}-\boldsymbol{r}|), \tag{4.12}$$

$$t^L(\boldsymbol{q},E) \equiv \frac{iM^2}{2E_c k_c}F^L_{D,X}(\boldsymbol{q}), \tag{4.13}$$

$$\tilde{t}^L_{D,X}(|\boldsymbol{r}|,E) = \int\frac{d\boldsymbol{q}}{(2\pi)^3}t^L_{D,X}(q,E)e^{-i\boldsymbol{q}\cdot\boldsymbol{r}}, \tag{4.14}$$

where j_n is a n-th order spherical Bessel function. For the nonlocal densities $\rho^L(\boldsymbol{r},\boldsymbol{r'})$ are approxaimatd using the local density $\rho^L(\boldsymbol{r})$ as

$$\rho^L(\boldsymbol{r},\boldsymbol{r'}) \approx \rho^L((\boldsymbol{r}+\boldsymbol{r'})/2)\frac{3}{|\boldsymbol{r'}-\boldsymbol{r}|k_F}j_1(|\boldsymbol{r'}-\boldsymbol{r}|k_F), \tag{4.15}$$

where k_F is related to the baryon (vector) density by $\rho^V((\boldsymbol{r}+\boldsymbol{r'})/2) = 2k_f^3/3\pi^2$.

For a spin-zero particle, only the scalar, vector, and tensor densities are nonzero. In addition, the tensor contribution is found to be negligible. Therefore, the optical potential U_{opt} can be expressed as

$$U_{\text{opt}} \simeq U^S + \gamma^0 U^V. \tag{4.16}$$

The MRW model assumes that the NN amplitude between projectile and target is unmodified by the surrounding nucleons. While this assumption is valid at high energies ($\gtrsim$1 GeV), it is necessary to correct the optical potentials for medium modifications from Pauli blocking for intermediate energies (≈200–300 MeV). These effects are incorporated through a "Pauli blocking factor" $a(E)$ with a local-density approximation, as follows:

$$U^L(r,E) \to \left[1 - a(E)\left(\frac{\rho^V(r)}{\rho_0}\right)^{2/3}\right]U^L(r,E), \tag{4.17}$$

where $\rho_0 = 0.1934\,\text{fm}^{-3}$.

The blue line in Fig. 4.2 is the MH-model calculation with Dirac-Hartree (DH) density [86] of ^{132}Sn. Although the calculation reproduces the oscillation pattern at around the second diffraction peak ($\theta_{\text{cm}} \approx 24°$), the amplitude of the second and third peaks deviates considerably from the experimental results.

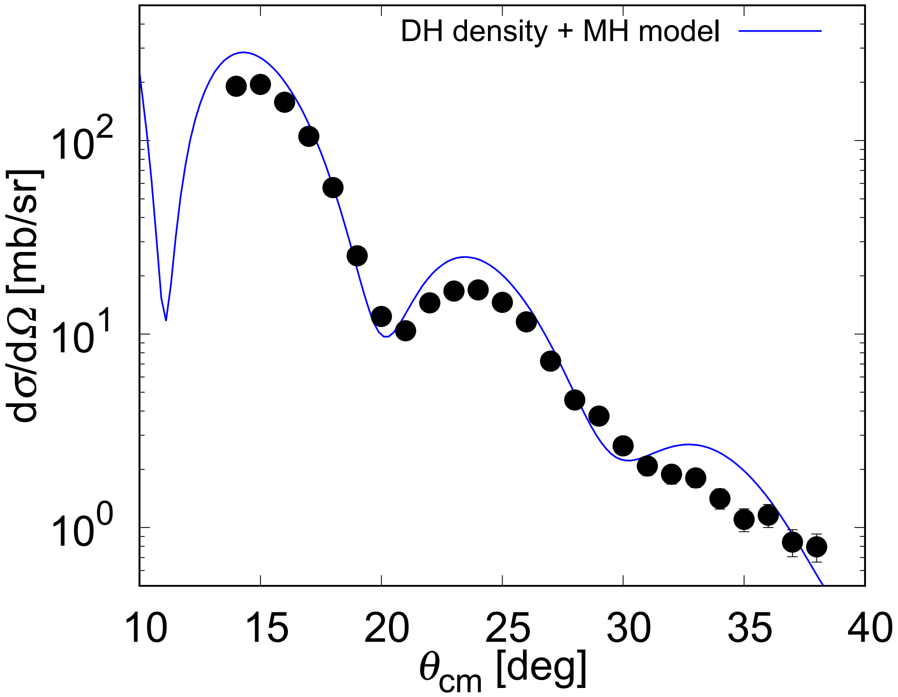

Figure 4.2: RIA calculation formulated by Murdock-Horowitz with the Dirac-Hartree density.

4.1.1 Scalar and vector density distributions

In the RIA calculations, both the scalar density ρ^S and the vector density ρ^V are required. Since the vector density corresponds to the baryon density ρ, it can be normalised by the baryon number. In contrast, the scalar density does not have an analogous normalisation condition, making it difficult to extract directly from the experimental data. In the MH model, they used the nuclear matter approximation, in which the scalar density ρ^S is desicribed in the form of the vector density ρ^V as

$$\rho^S(r) \approx \Big(1 - \frac{3}{10}\frac{k_F^2}{M^{*2}}\Big)\rho^V(r), \tag{4.18}$$

where k_F and M^* are the local Fermi momentum and the effective mass, respectively. However, according to DH densities for heavy nuclei, the ratio of scalar to vector densities has an almost constant value of 0.96, as reported in Ref. [87, 29]. Therefore, in this work, we adopted this assumption $\rho^S = 0.96\rho^V$ when extracting the density from the experimental results or when using theoretical densities in which the scalar density cannot be obtained.

4.1.2 Coulomb potential

In the MH-model, the Coulomb potential is calculated by assuming a uniform spherical charge density distribution with radius $r_0 A^{1/3}$, where $r_0 \approx 1.25\,\mathrm{fm}$. Since the Coulomb potential was found to affect the scattering observables, especially at high momentum, the charge density ρ_{ch} is obtained by folding the baryon density with the intrinsic charge distributions of the proton and neutron as

$$\rho_{ch}(\boldsymbol{r}) = \int d\boldsymbol{r'} \rho_p(\boldsymbol{r'}) \rho^p_{ch} + \int d\boldsymbol{r'} \rho_n(\boldsymbol{r'}) \rho^n_{ch}, \tag{4.19}$$

where $\rho_{p(n)}$ denotes the point proton (neutron) density distributions, and $\rho^{p(n)}_{ch}$ represents the intrinsic charge distribution of the single proton (neutron). The charge form factor $F_{ch}(q)$, with q being the momentum transfer, is defined as the Fourier transform of the charge density $\rho_{ch}(r)$, and is obtained by applying the Fourier transform to Eq. (4.19) as follows:

$$F_{ch}(q) \simeq F_p(q) G^p_E(q^2) + F_n(q) G^n_E(q^2), \tag{4.20}$$

where $F_{p(n)}$ is the Fourier transform of the point proton (neutron) density distribution. The functions $G^p_E(q^2)$ and $G^n_E(q^2)$ are Sachs electric form factors of the proton and neutron [88], taken in the following froms [89]:

$$G^p_E(q^2) = \left(1 + \frac{q^2}{12} R^2_p\right)^{-2}, \tag{4.21}$$

$$G^n_E(q^2) = \left(\frac{q^2 R^2_n/6}{1 + q^2/M^2}\right) G^p_E(q^2), \tag{4.22}$$

where $R^2_{p(n)}$ is the mean-square charge radius of the single proton (neutron). In this paper, R_p and R^2_n are taken as 0.84075(64) fm [90] and $-0.1155(17)\,\text{fm}^2$ [91], respectively.

4.2 Medium modification

While the Pauli blocking factor $a(E)$ is introduced in Eq. (4.17), the MH-model calculation cannot fully reproduce the experimental data. In our previous works [87, 29, 18], a medium-modified RIA (mm-RIA) calculation was developed, in which a phenomenological modification is incorporated into the RLF NN interactions to take medium effects, such as Pauli blocking, vacuum polarisation [92, 93], multi-step process [94], and partial restoration of chiral symmetry [95], into account. The modification is made by introducing the density-dependent parameters into the coupling constants and masses of σ and ω mesons as

$$\begin{aligned} g^2_i, \overline{g}^2_i \quad &\rightarrow \frac{g^2_i}{1 + a_i \rho(r)/\rho_0}, \frac{\overline{g}^2_i}{1 + \overline{a}_i \rho(r)/\rho_0}, &(4.23)\\ m_i, \overline{m}_i \quad &\rightarrow m_i \left[1 + b_i \frac{\rho(r)}{\rho_0}\right], \overline{m}_i \left[1 + \overline{b}_i \frac{\rho(r)}{\rho_0}\right], &(4.24)\\ i \quad &= \sigma, \omega, \end{aligned}$$

where g_i, $\overline{g}_i$, m_i, and $\overline{m}_i$ are the coupling constants and masses of σ and ω mesons for real and imaginary amplitudes, respectively. The medium-modified parameters a_i, $\overline{a}_i$, b_i,

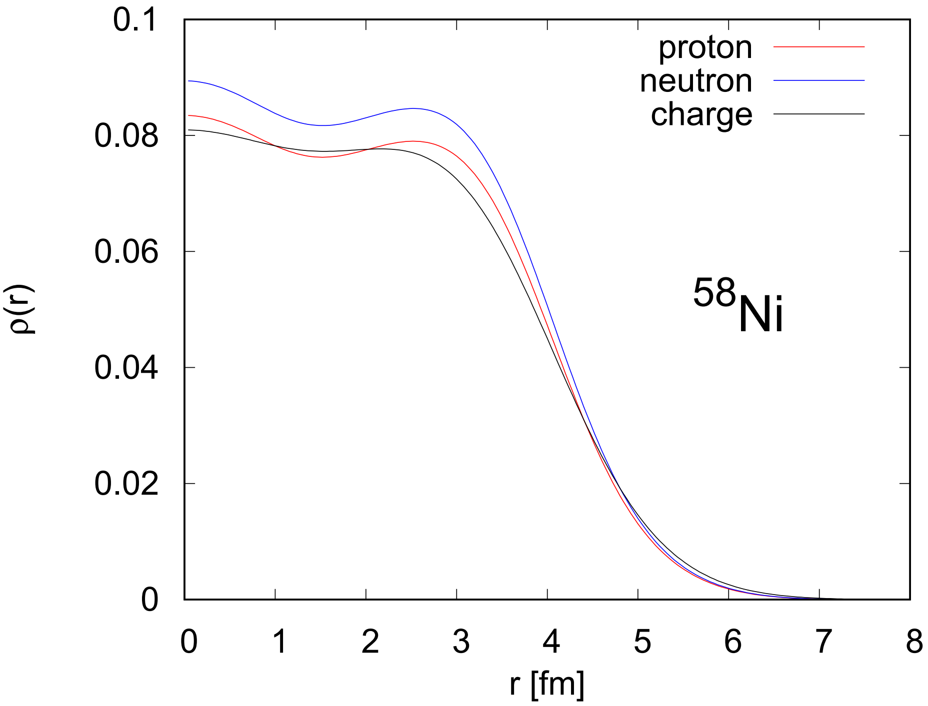

Figure 4.3: Density distributions of ^{58}Ni. Charge density is taken from Ref. [26]. Proton density was obtained by unfolding the charge density, and neutron density is assumed to be the same shape as the proton density ($\rho_n(r) = (N/Z)\rho_p(r)$).

$\overline{b}_i$ are calibrated to reproduce the polarized proton elastic scattering data from ^{58}Ni at 200 MeV. Since the modification has a universal form of density terms, the parameters calibrated with a real nucleus can be applied to other nuclei.

4.2.1 Calibration of the medium effect parameters

The parameters a_i, $\overline{a}_i$, b_i, and $\overline{b}_i$ were calibrated using polarized proton elsatic scattering data for ^{58}Ni. The reason that we have chosen ^{58}Ni is that the neutron density distribution can be assumed to be the same as the proton density distribution ($\rho_n(r) = (N/Z)\rho_p(r)$) because the neutron radius of ^{58}Ni is predicted to be almost the same as the proton radius by many mean-field calculations [96, 97, 12, 98, 34]. The proton and neutron densities of ^{58}Ni were obtained by unfolding the sum-of-Gaussian (SOG) charge density distribution [26], as shown in Fig. 4.3.

In the previous mm-RIA analysis for proton elastic scattering at 300 MeV [29, 18, 54], the number of parameters was reduced to four by assuming the same modification for the real and imaginary parts ($a_i = \overline{a}_i$, $b_i = \overline{b}_i$). However, full eight-parameter modifications were used to improve the reproducibility of the angular distribution of the scattering observables for the analysis of the 200 MeV data. The validity of the analysis at 200 MeV has been confirmed, since the analysis of ^{90}Zr data at 200 MeV yields a density distribution and a radius consistent with those obtained at 300 MeV [55].

Table 4.1: Best-fit medium-effect parameters in Eqs. (4.24), (4.25)

i	σ	ω
a_i	0.0210	0.1965
$\overline{a}_i$	2.0467	1.1549
b_i	0.0326	-0.0224
$\overline{b}_i$	-0.0799	-0.0501

The medium-effect parameters were calibrated by fitting the experimental data of cross sections $d\sigma/d\Omega$, analyzing powers A_y, and spin rotation parameters Q to minimise the chi-square (χ^2) value, which is given by

$$\chi^2 = \sum_i (y_i^{\mathrm{exp}} - y^{\mathrm{theo}})_i^2/\Delta y_i^2, \tag{4.25}$$

where y^{exp}, y^{theo}, and Δy_i^2 are the experimental data, error, and the calculated result, respectively. The data of the cross sections and analyzing power were taken from Ref. [55], and that of the spin rotation parameter was taken from Ref. [99]. These experiments were performed at the Research Center for Nuclear Physics (RCNP), University of Osaka. The best-fit parameters are summarised in Table 4.1. The values of $\overline{a}_i$ are relatively larger than the parameters obtained in the previous work [18], which was based on the four-parameter fit. In general, the Pauli blocking effect on proton elastic scattering at relatively low energy ($\lesssim 200\,\mathrm{MeV}$) is known to reduce the scalar and vector potential, particularly their imaginary parts [83, 100]. Therefore, the large values obtained here are likely to reflect this effect.

The red line in Fig. 4.4 is the mm-RIA calculation using the calibrated parameters with the realistic densities deduced from the charge density distribution, which is in better agreement with the experimental data than the original MH-model calculations (blue line). It should be noted that the mm-RIA does not well reproduce the experimental data of the spin rotation parameter. This discrepancy is possibly due to the use of the incorrect beam energy. Since the beam energy in the measurement of the spin rotation parameter was not precisely determined, it may differ from that in the measurement of the cross section and analyzing power. Therefore, future experiments with well-known beam energy, in which all three observables are measured simultaneously, are expected to improve the calibration accuracy.

4.3 Extraction of the matter density distribution

The black line in Fig 4.5 presents the calculation of the mm-RIA with the DH density, which well reproduces the experimental data compared with the MH-model calculation with the DH density (blue line).

Using the mm-RIA with the calibrated medium-effect parameters, we extracted the density distributions of ^{132}Sn. In previous analysis for stable nuclei [29, 18], proton density distributions were obtained by unfolding the charge density distributions measured

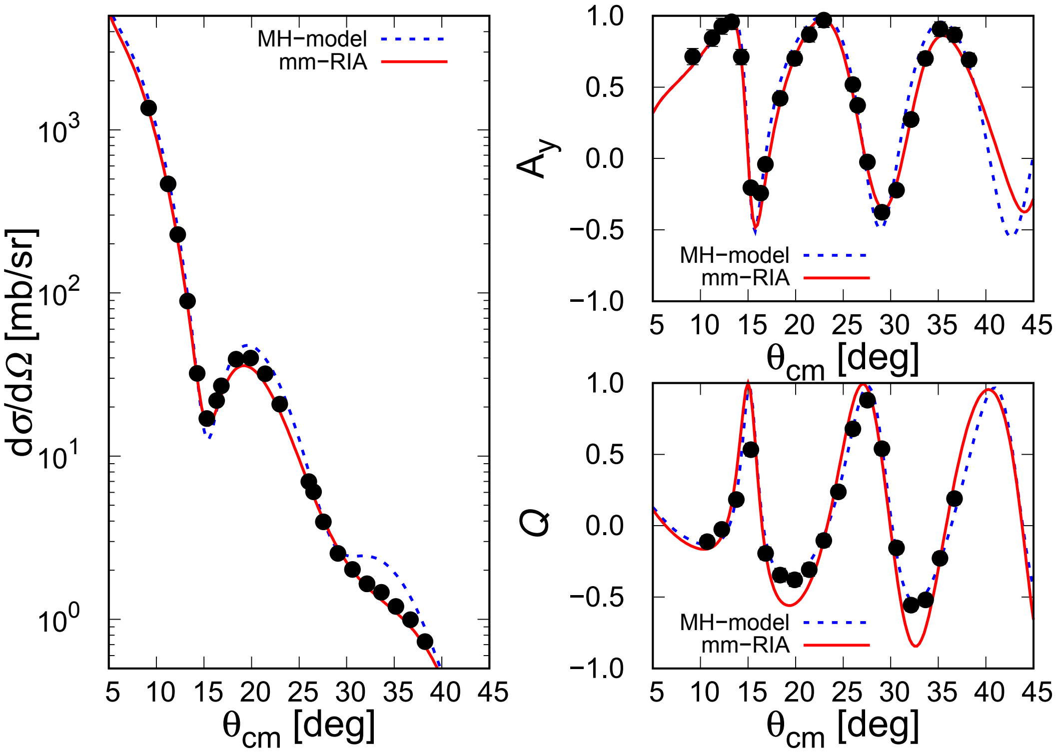

Figure 4.4: Angular distributions of differential cross sections, analyzing powers, and spin rotation parameters. The experimental data of differential cross sections and analyzing powers are taken from Ref. [55], while those of spin rotation parameters are taken from Ref. [99]. The blue dashed and red solid lines are the original MH-model calculation with DH density, and the mm-RIA calculation using the best-fit parameter with the realistic density, respectively.

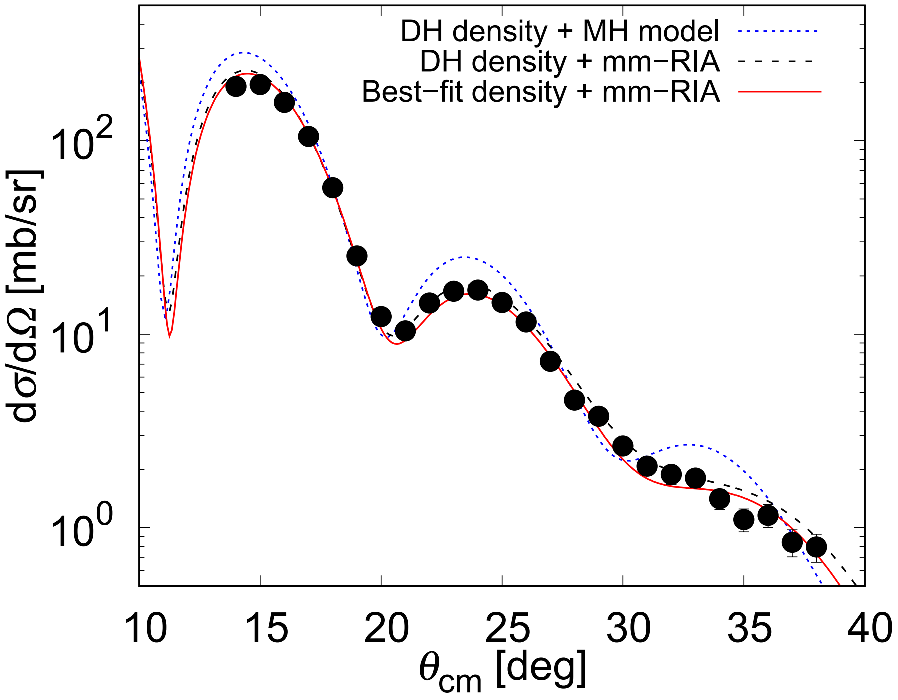

Figure 4.5: The mm-RIA calculation with the DH density and the best-fit density are shown as the black dashed and red solid lines, respectively. The blue dotted line shows the MH-model calculation with the DH density.

via electron scattering. However, the charge density distribution of ^{132}Sn has not been measured. Consequently, we developed and employed a new method in which the proton density distribution is constrained by the charge radius.

The proton and neutron density distributions were modelled with the two-parameter Fermi (2pF) functions:

$$\rho_i(r) = \frac{n_i}{1+\exp[(r-c_i)/z_i]}, \tag{4.26}$$

$$i = p, n, \tag{4.27}$$

where half-density radius c_i and diffuseness z_i are free parameters, and constant density n_i is a normalisation coefficient adjusted to conserve the number of protons and neutrons:

$$\int \rho_i(r) d\boldsymbol{r} = N_i, \tag{4.28}$$

$$N_p = Z, N_n = N. \tag{4.29}$$

$$\tag{4.30}$$

The matter density distribution ρ_m is simply given by the sum of the proton and neutron density distributions: $\rho_m(r) = \rho_p(r) + \rho_n(r)$. The mean-square radii $\langle r_i^2 \rangle$ are calculated as

$$\langle r_i^2 \rangle = \frac{1}{N_i} \int d\boldsymbol{r} \rho_i(r) r^2, \tag{4.31}$$

$$i = p, n, m, ch, \tag{4.32}$$

$$\tag{4.33}$$

where $N_m = A$ and $N_{ch} = Z$.

We constrained the c_p and z_p to reproduce the known value of the rms charge radius, $\langle r_{ch}^2 \rangle^{1/2} = 4.7093(76)$ fm as determined from the isotope-shift measurement using laser spectroscopy [35, 27]. The rms proton radius $\langle r_p^2 \rangle^{1/2}$ is related to the charge radius $\langle r_{ch}^2 \rangle^{1/2}$ by

$$\langle r_p^2 \rangle \simeq \langle r_{ch}^2 \rangle - R_p^2 - \frac{N}{Z} R_n^2. \tag{4.34}$$

Accordingly, the parameters c_p and a_p were constrained such that the condition $4.6463 < \langle r_p^2 \rangle^{1/2} < 4.6617$ fm was always satisfied.

The parameters c_i and a_i were searched to minimise the χ^2 defined by Eq. (4.25) for the cross section. The y_i^{theo} were given by

$$\left(\frac{d\sigma}{d\Omega}\right) = \sum_j f_j^{\text{beam}} \left(\frac{d\sigma}{d\Omega}\right)\Bigg|_{T_b = T_b^j}, \tag{4.35}$$

$$\overline{\left(\frac{d\sigma}{d\Omega}\right)_i} = \int_{\theta_i - \Delta\theta}^{\theta_i + \Delta\theta} d\theta \left(\frac{d\sigma}{d\Omega}\right), \tag{4.36}$$

$$y_i^{\text{theo}} = \sum_j f_{ij}^{\text{ang}} \overline{\left(\frac{d\sigma}{d\Omega}\right)_j}, \tag{4.37}$$

Table 4.2: Minimum χ^2 value and best-fit 2pF parameters.

χ^2_{min}/ndf	c_p [fm]	z_p [fm]	c_n [fm]	z_n [fm]
38.0/22	$5.632^{+0.076}_{-0.119}$	$0.430^{+0.063}_{-0.044}$	$5.581^{+0.066}_{-0.068}$	$0.576^{+0.033}_{-0.037}$

Table 4.3: Obtained root-mean-square radii and neutron skin thickness of ^{132}Sn.

$\langle r_p^2\rangle^{1/2}$ [fm]	$\langle r_n^2\rangle^{1/2}$ [fm]	$\langle r_m^2\rangle^{1/2}$ [fm]	Δr_{np} [fm]
$4.646^{+0.015}_{-0.000}$	$4.785^{+0.037}_{-0.039}$	$4.758^{+0.023}_{-0.024}$	$0.178^{+0.037}_{-0.050}$

where f_j^{beam} is the fraction of the beam energy of T_b^j and are obtained from Fig. 3.8. It is confirmed that a beam energy step size ($T_b^{j+1} - T_b^j$) of 2 MeV provides sufficient precision. The method for deriving f_{ij}^{ang} is given in Sec 3.4.7.

The red line in Fig. 4.5 shows the calculation of the mm-RIA with the best-fit density, which is in good agreement with the experimental data. The reduced minimum χ^2 (χ^2_{min}) value, namely divided by the number of degree-of-freedom $ndf = 22$, is approximately 1.7.

The standard errors of the parameter and the rms radii can be estimated from the increase of $\Delta\chi^2$ corresponding to one standard deviation from the χ^2_{min}, expressed as

$$\chi^2 \leq \chi^2_{\text{min}} + \Delta\chi^2. \tag{4.38}$$

Here, $\Delta\chi^2$ obeys the χ^2 probability density function for multiple parameters. In the present case, $\Delta\chi^2 \approx 3.5$, since the number of effective free parameters can be regarded as three, given the four fitting parameters (c_p, a_p, c_n, and a_m) subject to one constraint (Eq. (4.34)). The best-fit parameters with the errors are summarised in Table 4.2. The solid lines in Fig. 4.6 show the best-fit density distributions for protons (red), neutrons (blue), and matter (black). The bands surrounding the lines represent the error envelope of the distributions, determined by the minimum and maximum values among all possible distributions satisfying Eq. (4.38). The proton band has the nodes around 4.5 and 6.0 fm, caused by the radial constraint of Eq. (4.34). The reason why the matter band around the surface is narrower than that of protons or neutrons is considered to be that proton elastic scattering is inherently sensitive to the isoscalar density, especially around the surface region.

The obtained rms radii and neutron skin thickness Δr_{np} are summarized in Table 4.3. The error of the proton radius fully encompasses the constrained region derived from Eq. (4.34), and the best-fit value lies close to its minimum. The rms matter radius was deduced for the first time in this work.

4.3.1 Absolute factor

The absolute factor of the differential cross sections is highly sensitive to the extracted matter radius. This sensitivity was confirmed by extracting matter radii from the abso-

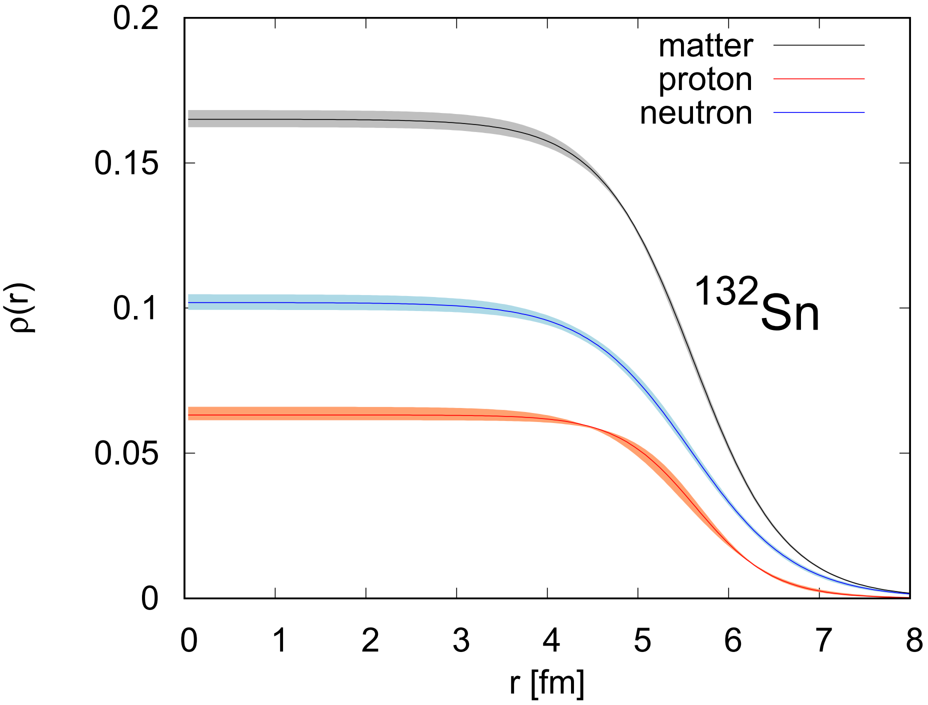

Figure 4.6: Extracted density distributions of proton (red), neutron (blue), and matter (black). The bands surrounding the lines represent the error envelope of the distributions estimated by Eq. (4.38).

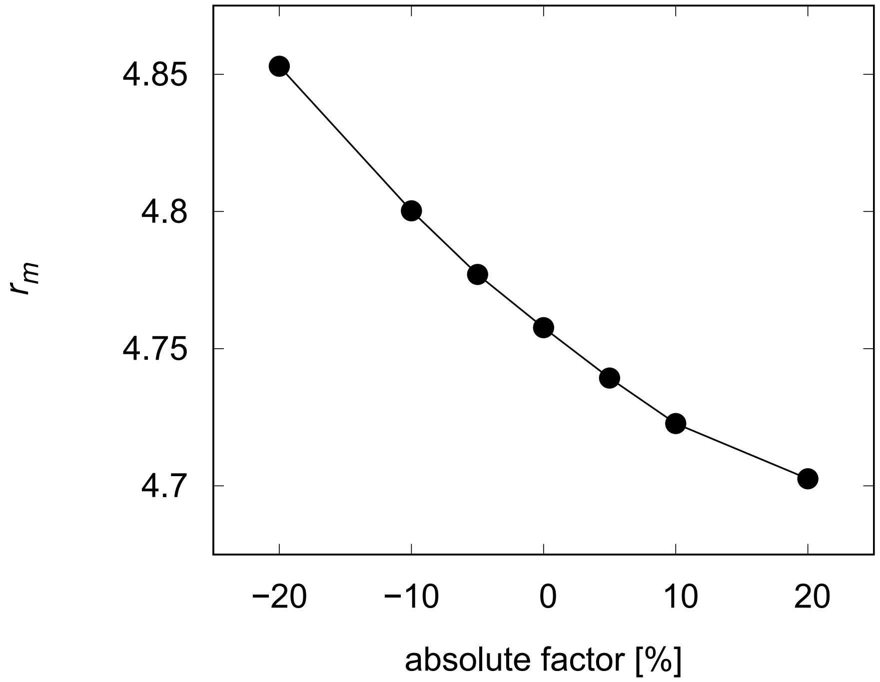

Figure 4.7: Absolute-factor dependence of the matter radius.

lutely shifted cross sections, as shown by Fig. 4.7. Figure 4.8 shows the absolute-factor dependence of χ^2_{min}. The minimum of χ^2_{min} occurs at the absolute factor of 0, supporting the evaluation of the target number using the proton elastic scattering from ^{48}Ca.

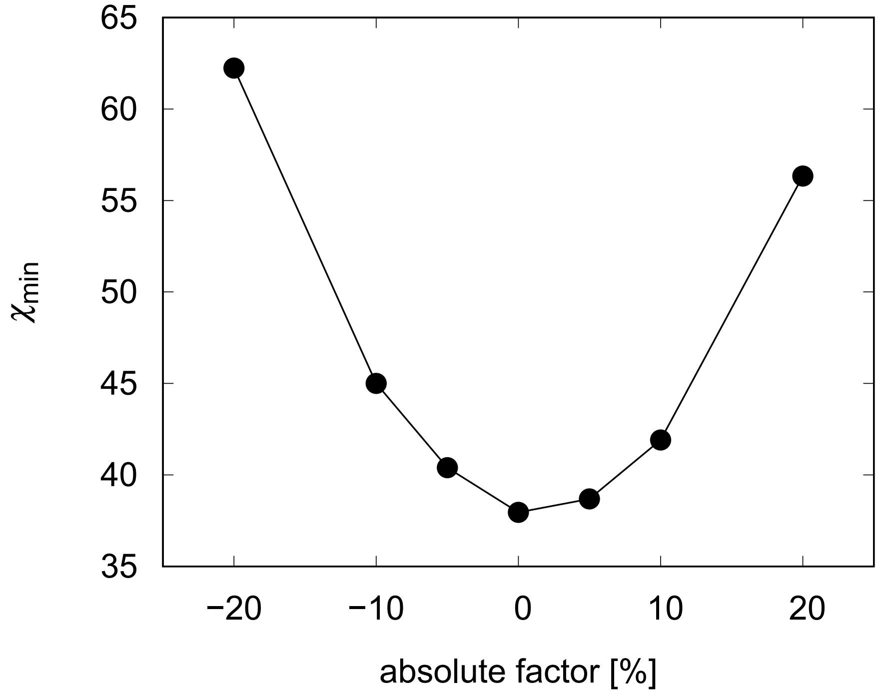

Figure 4.8: Absolute-factor dependence of the mininum χ^2.

Chapter 5

Discussion

In this section, we discuss the obtained cross sections, matter radii, and neutron skin thicknesses compared with the theoretical calculations. While somewhat repetitive, we compared the developed RIA model with the obtained cross sections, together with the phenomenological model using global Dirac optical potentials. For discussion about the structure, we employed not only conventional mean-field calculations, such as Skyrme Hartree-Fock (SHF) and relativistic mean-field (RMF), but also the state-of-the-art *ab initio* in-medium similarity renormalization group (IMSRG) [101] with the chiral EFT nucleon-nucleon (*NN*) and three-nucleon *3N* interactions.

In this work, four chiral EFT interactions are employed: 1.8/2.0(EM7.5) [60], 1.8/2.0(sim7.5) [60], $\mathrm{NNLO}_{\mathrm{sat}}$ [102], and $\Delta\mathrm{NNLO}_{\mathrm{GO}}$ [103]. The details of the calculations are described in Ref. [60]. The interactions reasonably reproduce the binding energies and charge radii across a wide range of nuclei. It should be noticed that the parameter optimizations of 1.8/2.0 (sim7.5), 1.8/2.0 (EM7.5), and $\mathrm{NNLO}_{\mathrm{sat}}$ involve binding energies and charge radii of medium-mass nuclei: ^{16}O for 1.8/2.0 (sim7.5) and 1.8/2.0 (EM7.5), and carbon and oxygen isotopes for $\mathrm{NNLO}_{\mathrm{sat}}$. On the other hand, only data up to $A = 4$ are employed for the parameter optimization for $\Delta\mathrm{NNLO}_{\mathrm{GO}}$.

5.1 Cross section

The phenomenological model using the global Dirac optical potential (GDOP) was developed by Cooper, Hama, and Clark [104, 105]. The nuclear potentials were calibrated using the proton elastic scattering data from the stable nuclei ranging from ^{12}C to ^{208}Pb at 65 to 1040 MeV. Although the GDOP model is not suitable for extracting nuclear density due to not being a microscopic model, it is known to satisfactorily reproduce proton elastic scattering data for stable nuclei. The green line in Fig. 5.1 shows the calculation using the GDOP for ^{132}Sn. While the calculation for ^{132}Sn reproduces the experimental data well for the backward angles, it exhibits a noticeable deviation in shape around the first and second peaks. While the calculation incorporates mass-number dependence, it does not explicitly include isospin dependence. This result, therefore, implies that the model calibrated only with data from stable nuclei may not perform well for the data from nuclei with significant isospin asymmetry, emphasizing the importance of measuring a wide range of unstable nuclei. Here, representative GDOP results are presented, while calculations for other GDOP models are given in Appendix D.

Compared with the GDOP and MH-model calculations, the developed mm-RIA calculation well reproduces the experimental results. As shown in Table 5.1, its minimum χ^2 value is also much smaller than those of the other calculations. Therefore, we can extract information about the nuclear structure by analyzing the cross sections using the mm-RIA calculations.

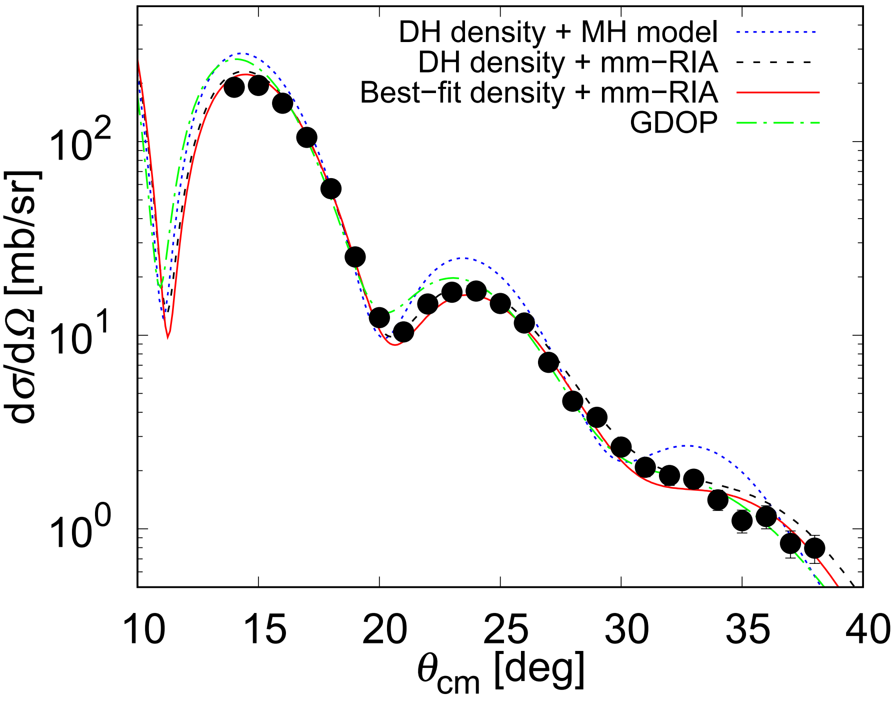

Figure 5.1: Glocal Dirac optical potential calculation [104, 105] (green, dash-dot). The blue dotted, black dashed, and red solid lines are the MH-model [83] with DH density [86], the mm-RIA calculation with the DH density, and the mm-RIA calculation with the best-fit density, respectively.

Table 5.1: Minimum χ^2 values of the calculations.

Framework	χ^2_{min}
GDOP	147.3
MH model + DH density	475.1
mm-RIA + DH density	53.35
mm-RIA + Best-fit density	37.95

The bands in Fig. 5.2 represent the Rutherford ratios of the mm-RIA calculations using the densities from the IMSRG calculations. In general, all the calculations reasonably reproduce the experimental data ($\chi^2 = 50$–150). It is confirmed that the further outward the positions of the valleys around $\theta_{\rm cm} = 20°$ and $\theta_{\rm cm} = 30°$, the smaller the corresponding matter radii; 4.816–4.830 (1.8/2.0 (sim7.5)), 4.816–4.830 (1.8/2.0 (EM7.5)), 4.791–4.824 (NNLO$_{\rm sat}$), and 4.736–4.746 (ΔNNLO$_{\rm GO}$) fm. The calculation using the ΔNNLO$_{\rm GO}$ (cyan band) is in the best agreement with the experimental data and closely follows the calculation using the best-fit density (red line).

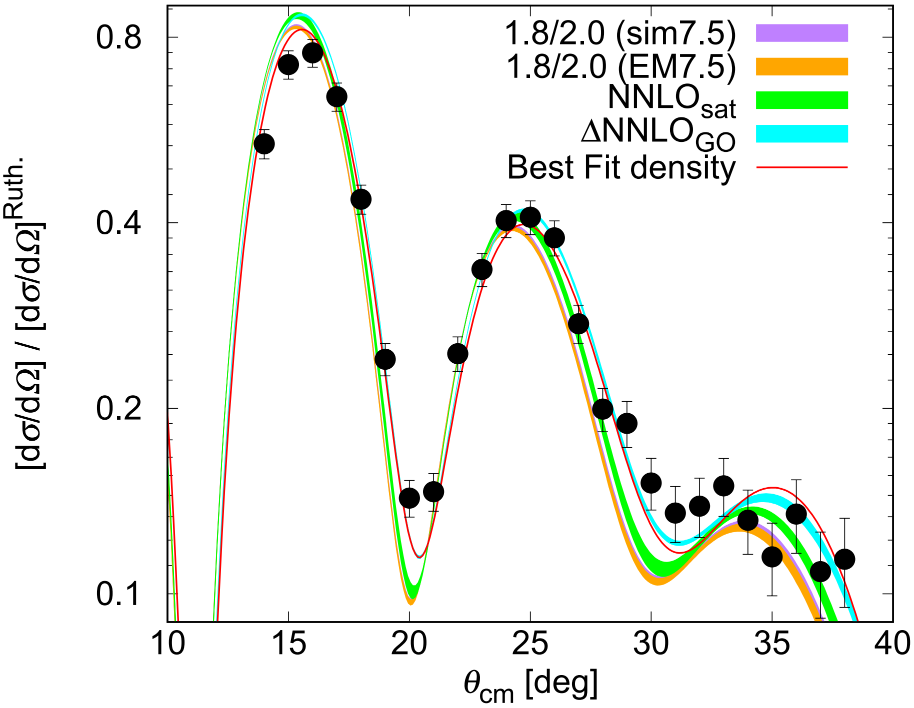

Figure 5.2: Differential cross sections divided by the Rutherford cross section. The red solid line shows the mm-RIA calculation with the best-fit density. The purple, orange, green, and cyan bands are the IMSRG calculations with the 1.8/2.0(sim7.5), 1.8/2.0(EM7.5), ΔNNLO$_{\rm GO}$, and NNLO$_{\rm sat}$ interactions, respectively. It should be noted that the purple and orange bands nearly overlap.

5.2 Matter radius

Figure 5.3 shows the measured and theoretical correlation between the matter and charge radii of ^{132}Sn. The pink circles are the predictions of Skyrme energy density functionals (EDFs) with SLy4, SLy5 [106], SAMi [107], SGII [108], SkM* [109], HFB9 [110], UNEDF0 [111], UNEDF1 [112], and UNEDF2 [113] interactions, and the black diamonds are those of relativistic-mean field (RMF) with FSUGold and NL3 interactions [114, 115, 56]. The values are also summarized in Table 5.2. The matter radius measured in this work is consistent only with that by the ΔNNLO$_{\rm GO}$, but smaller than the other calculations. However, the charge radius of ΔNNLO$_{\rm GO}$ is smaller than the experimental value measured at ISOLDE [35]. Both charge and matter radii of the experimental results shrink compared with the SHF and IMSRG calculations except for ΔNNLO$_{\mathrm{GO}}$, which were calibrated with the properties of the stable nuclei.

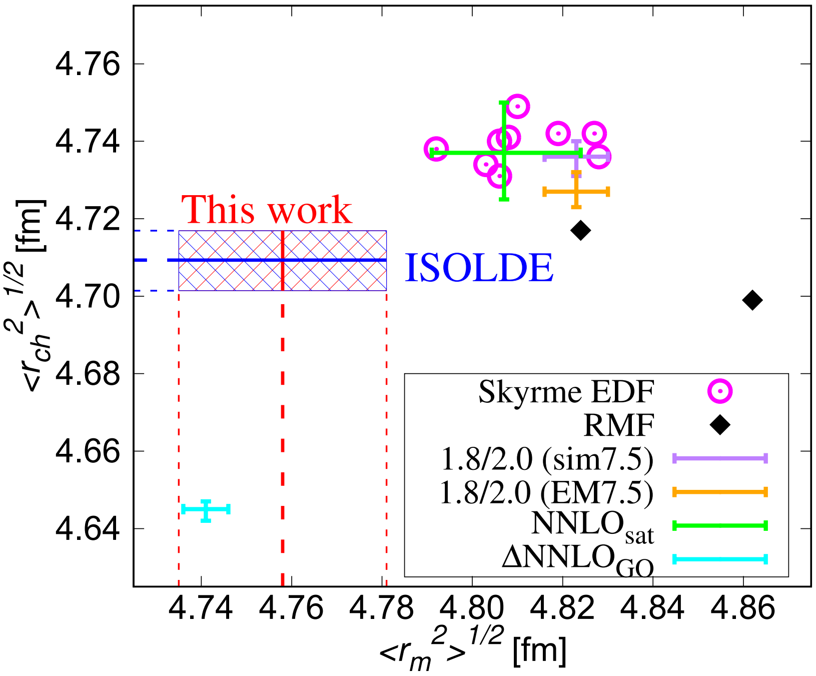

Figure 5.3: Experimental and theoretical values of the charge radius $\langle r_{ch}^2\rangle^{1/2}$ and matter radius $\langle r_m^2\rangle^{1/2}$ of ^{132}Sn. SLy4, SLy5 [106], SAMi [107], SGII [108], SkM* [109], HFB9 [110], UNEDF0 [111], UNEDF1 [112], and UNEDF2 [113] interactions are used for the "Skyrme EDF", and the FSUGold and NL3 [114, 115, 56] interactions are used for the "RMF". The experimental charge radius value of the "ISOLDE" is taken from Ref. [35].

Figure 5.4 shows the matter radii of the Sn isotopes, obtained in this work and in Ref. [29]. The blue solid and dashed lines represent RMF calculations with NL3 and FSUgold parameter sets. The red solid and dashed lines represent SHF calculations with SLy5 and SGII parameter sets. Compared with the radii of the stable nuclei along the calculation trends, the matter radius ^{132}Sn is found to shrink. Such a phenomenon is also confirmed for the charge radii, as shown in Fig. 5.5. Furthermore, similar behaviors were also seen in the Ca isotope chain [42, 43]. Sn isotopes have a very long isotopic chain, which enables us to conduct more detailed investigations of these aspects.

5.3 Neutron skin thickness

Figure 5.6 shows a summary of the neutron skin thickness Δr_{np} of experimental results and theoretical calculations, including the IMSRG, SHF, and RMF calculations. The values are also summarized in Table 5.2. Only the IMSRG (NNLO$_{sat}$), SHF (SGII), and

Table 5.2: Matter radius $\langle r_m^2 \rangle^{1/2}$, charge radius $\langle r_{ch}^2 \rangle^{1/2}$, and neutron skin thickess Δr_{np} for ^{132}Sn.

	$\langle r_m^2 \rangle^{1/2}$ [fm]	$\langle r_{ch}^2 \rangle^{1/2}$ [fm]	Δr_{np} [fm]
Experiment			
This work	$4.758^{+0.023}_{-0.024}$		$0.178^{+0.037}_{-0.050}$
ISOLDE [35]		4.7093(76)	
PDR [6]			0.258(24)
Theory			
IMSRG(1.8/2.0(EM7.5)) [60]	4.731–4.736	4.816–4.830	0.228–0.234
IMSRG(1.8/2.0(sim7.5)) [60]	4.723–4.732	4.816–4.830	0.240–0.246
IMSRG(NNLO$_{\text{sat}}$) [102]	4.725–4.750	4.791–4.824	0.198–0.208
IMSRG(ΔNNLO$_{\text{GO}}$)) [103]	4.642–4.647	4.736–4.746	0.244–0.250
SHF(HFB9) [110]	4.740	4.806	0.219
SHF(SAMi) [107]	4.749	4.810	0.211
SHF(SGII) [108]	4.738	4.792	0.200
SHF(SLy4) [106]	4.741	4.808	0.221
SHF(Sly5) [106]	4.734	4.803	0.225
SHF(SkM*) [109]	4.731	4.806	0.233
SHF(UNEDF0) [111]	4.736	4.828	0.261
SHF(UNEDF1) [112]	4.742	4.827	0.249
SHF(UNEDF2) [113]	4.742	4.819	0.236
RMF(FSUGold) [115]	4.717	4.824	0.271
RMF(NL3) [114]	4.699	4.862	0.346

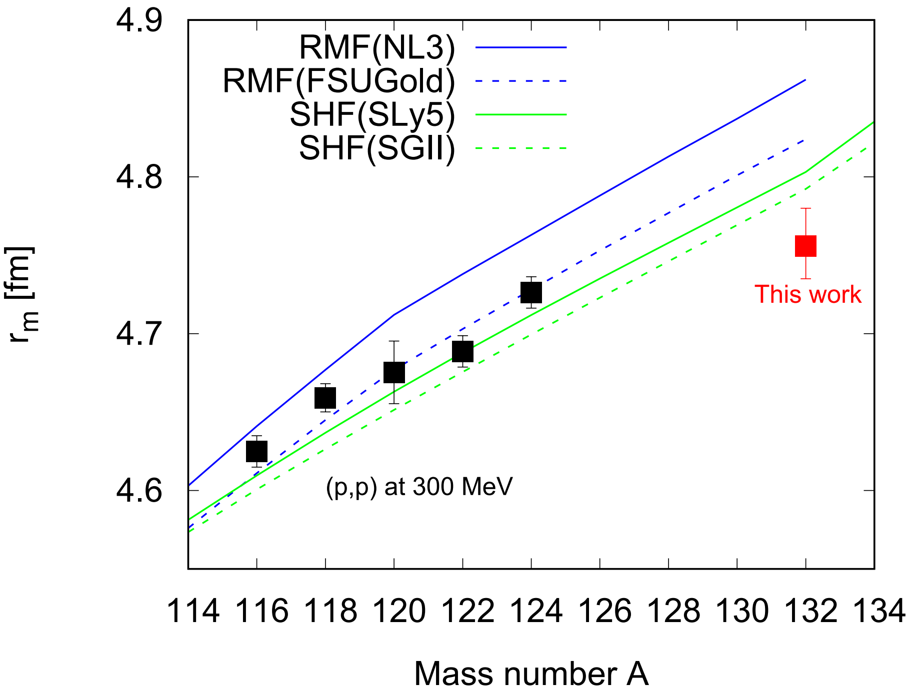

Figure 5.4: Systematic behavior of the rms matter radii of tin isotopes. The blue and green lines show Skyrme Hartree-Fock and relativistic mean-field calculations, respectively. The experimental data for ^{116,118,120,122,124}Sn taken from Ref. [29].

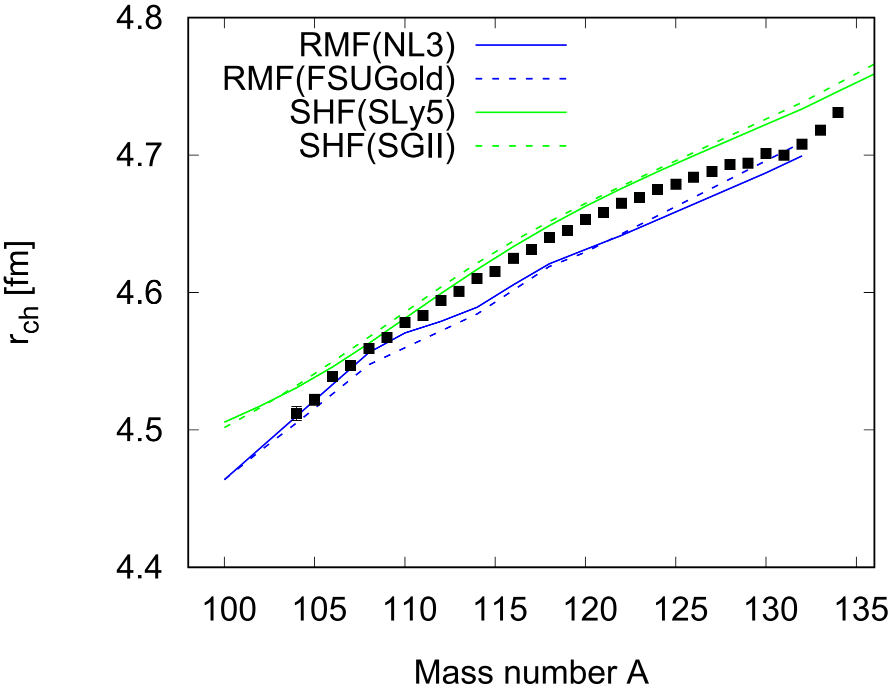

Figure 5.5: Systematic behavior of rms charge radii of tin isotopes. The experimental data taken from Ref. [116].

SHF (SAMi) are consistent with our result, and the others are larger. Our results are smaller than the value deduced from the PDR experiment.

Using the correlation function between the L parameter and the neutron skin thickness Δr_{np} of ^{132}Sn in Ref. [6], as shown in Fig. 1.4, we deduced

$$L = 12.0^{+24.3}_{-32.5}\,\text{MeV} \tag{5.1}$$

from the obtained neutron skin thickness.

The parity-violating elastic scattering measurements, PREX-2 [8] and CREX [28], are one of the most important experiments for determining the parameter L. However, analyses of the PREX-2 and CREX data using the conventional EDFs have led to inconsistent conclusions regarding the extraction of L and Δr_{np}: PREX-2 favors very large values of both L and Δr_{np}, whereas CREX favors much smaller ones, which is referred to as the PREX-CREX puzzle. While our present result favors the values suggested by CREX, further investigations of more isospin-asymmetric systems are necessary to resolve the puzzle.

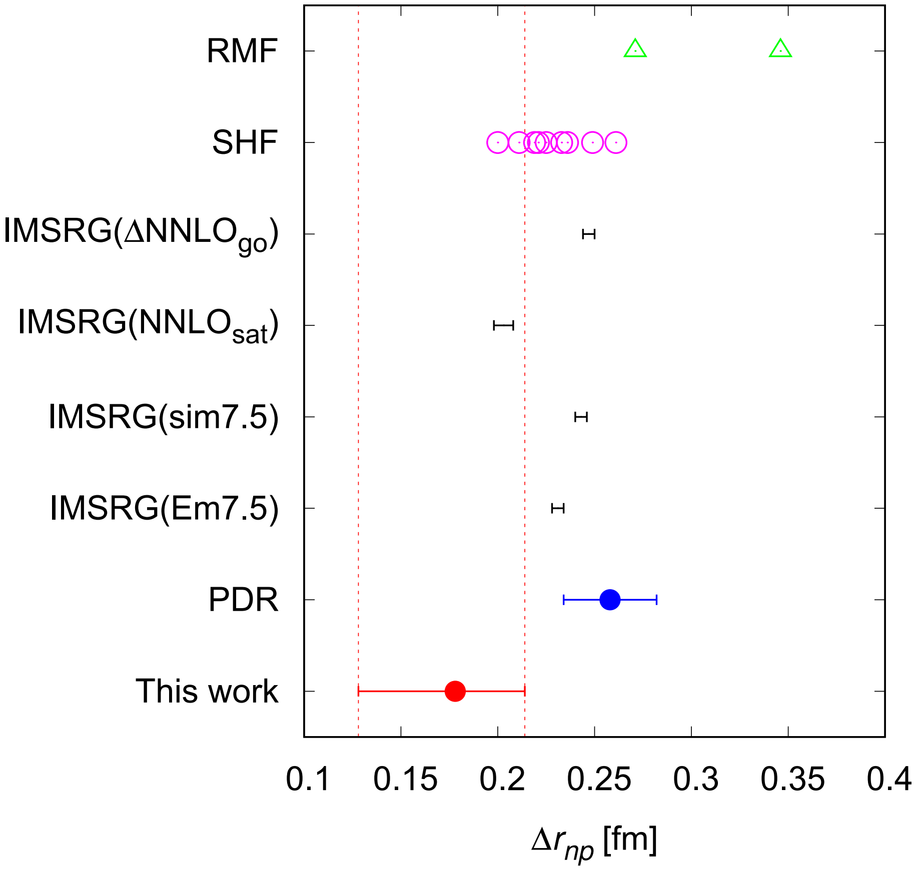

Figure 5.6: Neutron skin thickness Δr_{np} of ^{132}Sn. The blue point represents the value deduced from the PDR experiment.

5.4 Future perspective

5.4.1 Extraction of proton and neutron density distributions of unstable nuclei

In this work, we deduced only the matter distribution of ^{132}Sn since the charge density distributions have not yet been measured. However, we have developed a new method to extract proton and neutron density distributions independently, in which proton elastic scattering measurements at two distinct incident energies are performed. This method was verified by measuring proton elastic scattering from ^{90,92,94}Zr at 197 and 295 MeV [55]. The proton density distributions deduced by the new method are consistent with those obtained by unfolding the charge density distributions. In addition, the neutron radii by the new method are also consistent with those by the conventional method, in which the charge density distributions and proton elastic scattering at a single energy are used.

This new method enables us to measure proton and neutron density distributions of unstable nuclei. Actually, we have already measured proton elastic scattering from ^{132}Sn at 300 MeV/nucleon [117]. A combined analysis of the 200 and 300 MeV data can provide a model-independent density distribution and more accurate proton and neutron radii. Such a model-independent analysis will also enable us to attempt a 2D plotting method of the IS-IV densities. In addition, it will allow us to apply the proton-density-polarization technique by measuring proton elastic scattering for proton-rich side Sn isotopes. As a first step, we are preparing a measurement for the stable nucleus ^{112}Sn at RCNP. Furthermore, we aim to extend these measurements into the region of unstable nuclei.

χ^2 maps for density parameters

By using the present data, we examined the sensitivity of the proton elastic scattering for the proton and neutron densities.

Figures 5.7 show the χ^2 map of $(c_i,\ z_i)$ for ^{9}C, obtained from the analysis of proton elastic scattering at 300 MeV/nucleon using a similar model. When $(c_p,\ z_p)$ were fixed, $(c_n,\ z_n)$ were searched to minimize χ^2, and vice versa. In this case, two solutions were found, enclosed by solid and dashed lines. Furthermore, since the rms radius can be approximately written as

$$\langle r_i^2 \rangle \simeq \frac{3}{5}c_i^2 + \frac{7}{5}\pi^2 z_i^2 \tag{5.2}$$

by using the Sommerfeld expansion [118], it is evident that the elastic probe is sensitive to the radius.

Figures 5.8 show the χ^2 maps obtained in the present study. Unlike the case of ^{9}C, only a single solution exists, and the neutron density distributions can be well constrained. This is considered to be because of the large atomic number, where the Coulomb potential allows a clearer distinction between protons and neutrons. However, due to the presence of a sizable neutron skin, the internal proton density distribution is not strongly constrained. Consequently, the restriction imposed by the charge radius or a measurement at another energy proves particularly effective in extracting the accurate densities.

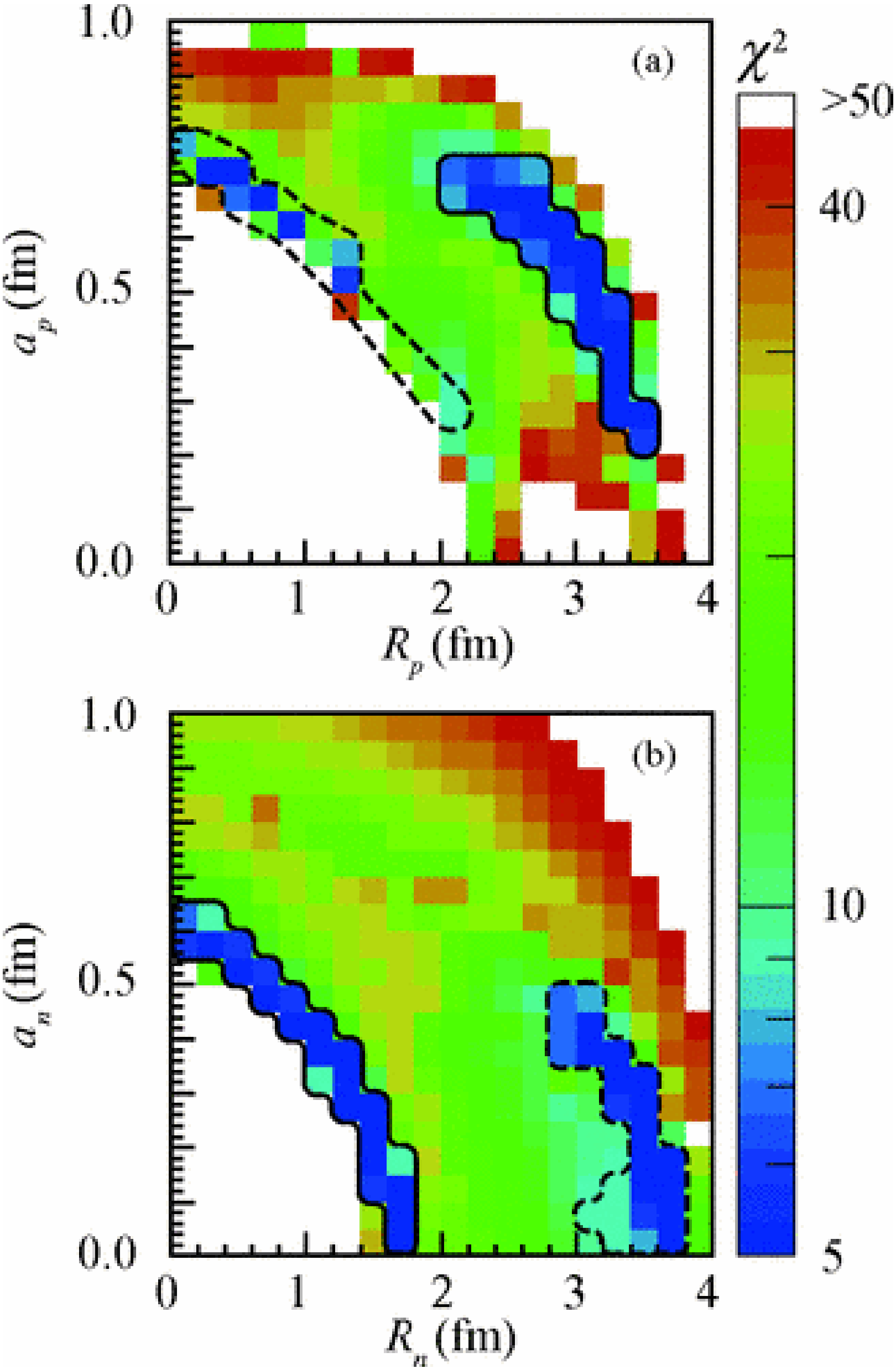

Figure 5.7: Two-dimensional plots of χ^2 of (a) ($c_p = R_p$, $z_p = a_p$) and (b) ($c_n = R_n$, $z_n = a_n$) for ^{9}C via proton elastic scattering at 300 MeV/nucleon. The regions which satisfy $\chi^2 \leq \chi^2_{\text{min}} + \Delta\chi^2$ are enclosed by the solid and dashed curves. Taken from Ref. [54].

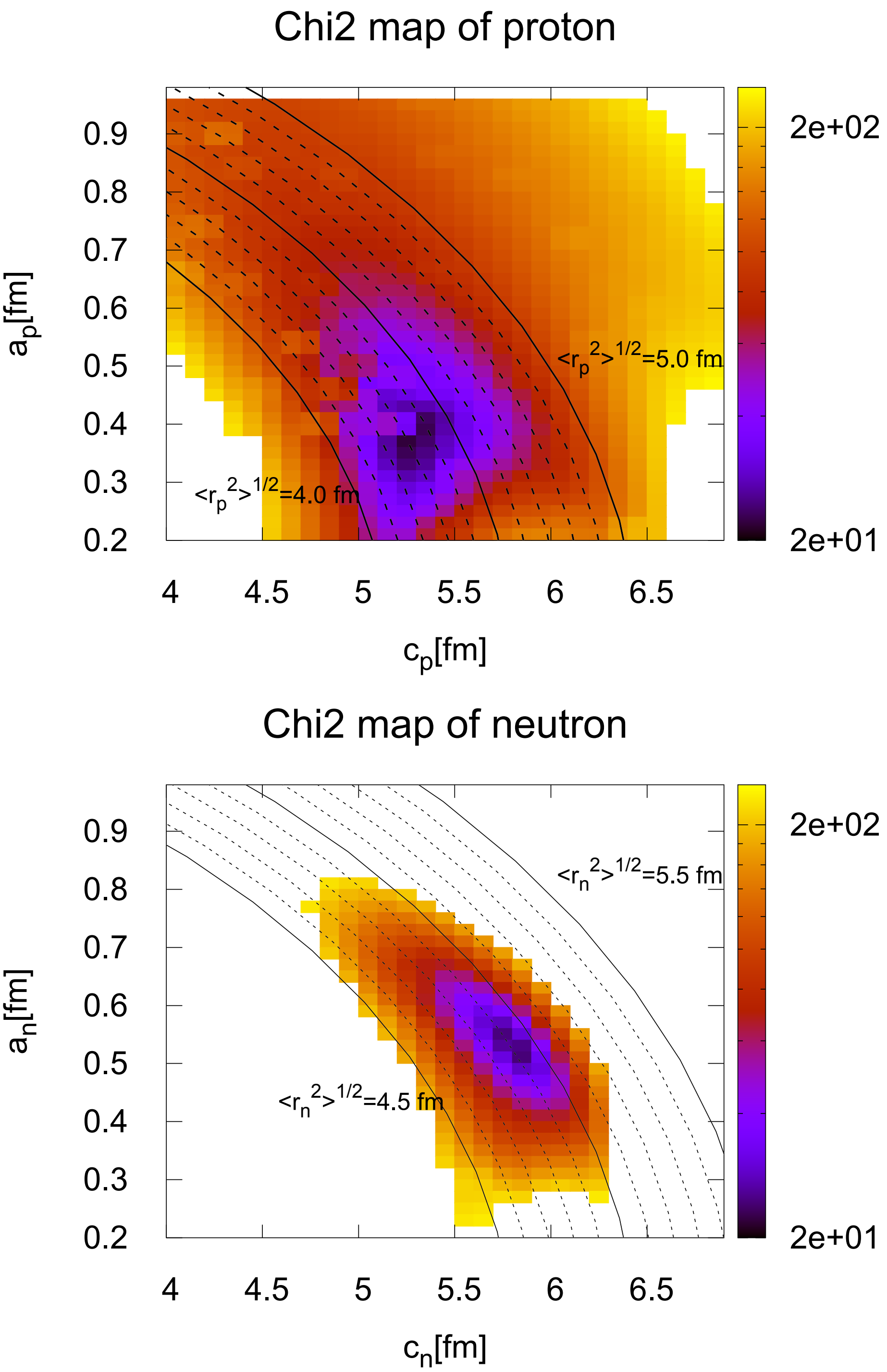

Figure 5.8: Two-dimensional plots of χ^2 of (Upper panel) $(c_p,\, z_p = a_p)$ and (Lower panel) $(c_n,\, z_n = a_n)$ for ^{132}Sn. The solid lines indicate radii of 4.0, 4.5, and 5.0 fm for the proton map and 4.5, 5.0, and 5.5 fm for the neutron map, while the dashed lines correspond to 4.1—4.4 and 4.6—4.9 fm for the proton map and 4.6—4.9 and 5.1-–5.4 fm for the neutron map.

Chapter 6

Summary

In order to determine the density distributions and radii of ^{132}Sn, we measured, for the first time, the angular distribution of the cross sections for proton elastic scattering from ^{132}Sn at 196–210 MeV/nucleon. Precise measurements of the cross sections covering a wide momentum-transfer range are necessary to extract accurate density distributions and radii. To this end, we have developed and employed a new PID method, a solid hydrogen target, and a recoil proton spectrometer, thereby obtaining high-statistical and high-quality data over the momentum transfer-range of 0.80 to 2.1 fm^{-1}. The typical excitation energy resolution is 600 keV (σ), which allows us to clearly identify the elastic events.

The experimental data were analyzed using the RIA calculation with RLF NN interaction. To explain the proton elastic scattering at intermediate energies, medium-modification parameters were introduced into the interactions as phenomenological density-dependent terms. The parameters were calibrated to reproduce the angular disturbances of the experimental observables for polarized proton elastic scattering from ^{58}Ni at 200 MeV.

Using the mm-RIA calculation, we extracted the matter density distribution, where the proton and neutron density distributions were modeled with 2pF functions. The parameters of the proton distribution were constrained to reproduce the charge radius measured at ISOLDE. The obtained rms matter radius is $4.758^{+0.023}_{-0.024}$ fm.

These experimental results are compared with the theoretical calculations, including *ab initio* IMSRG calculations as well as mean-field calculations. The cross sections and matter radius are consistent with those predicted by the IMSRG calculation using $\Delta\mathrm{NNLO}_{\mathrm{GO}}$ interaction. It is found that, however, no theoretical calculations can reproduce both experimental charge and matter radii simultaneously. Regarding the isotopic trend, the matter radius at the magic number $N = 82$ is smaller than the values predicted by the SHF and RMF calculations, a behavior similar to that observed in the Ca isotopes.

The neutron skin thickness was also deduced to be $0.178^{+0.037}_{-0.050}$ fm, which is correspond to $L = 12.0^{+24.3}_{-32.5}$ MeV by using the correlation from the mean-field calcualtions. The value is more consistent with the CREX result than with the PREX result.

Acknowledgement

The present thesis could not have been compiled without the dedicated and kind support of many people. I would like to take this opportunity to express my sincere thanks to them.

First and foremost, I would like to express my deepest gratitude to my supervisor, Prof. Juzo Zenihiro. He not only taught me the knowledge of proton elastic scattering but also provided me with a broad foundation in physics and experimental techniques. His constant encouragement and countless discussions greatly enriched my research. Without his guidance, this thesis would not have been possible.

I am also sincerely grateful to Prof. Tomohiro Uesaka, the head of my current laboratory at RIKEN. He continuously encouraged me and offered numerous insightful suggestions based on his broad expertise.

I would like to thank all members of the ESPRI collaboration. In particular, core members Prof. Harutaka Sakaguchi, Prof. Satoru Terashima, and Prof. Yohei Matsuda provided invaluable guidance and advice not only for this study but also for many experiments and data analyses.

Since the present experiment (RIBF79) was carried out in 2016, I could not participate in the experiment. I am deeply indebted to all members of the RIBF79 collaboration for enabling me to analyze the high-quality data. I am also grateful to the accelerator operators and the BigRIPS team for providing the stable beams.

I would like to thank Prof. Takayuki Miyagi and Dr. Pierre Arthuis for providing the IMSRG calculations and for engaging in fruitful discussions that greatly supported the theoretical aspects of this work. I am also grateful to Prof. Tomoya Naito for providing the SHF calculations and for many stimulating discussions on physics beyond the scope of this study.

I am thankful to members of the Zenihiro-group–Mr. Tomoya Harada, Ms. Shiyo Enyo, Mr. Ryotaro Tsuji, Mr. Kanta Yahiro, Mr. Takayuki Yano, Mr. Tomoya Nakada, and Mr. Makoto Ogura–for making both experiments and daily life enjoyable.

I also wish to express my gratitude to many colleagues at RIKEN since I have been based at RIKEN over the past five years. I would like to appreciate Dr. Hidetada Baba, Prof. Daisuke Suzuki, Prof. Junki Tanaka, Dr. Yuki Kubota, Prof. Shumpei Koyama, Ms. Shoko Takeshige, Mr. Koshi Higuchi, and Mr. Taiki Sugiyama for sharing a fulfilling time with me.

I have participated in many experiments with the Center for Nuclear Study (CNS) people. I am grateful to Prof. Shinsuke Ota, Prof. Nobuaki Imai, Dr. Shin'ichiro Michimasa, Prof. Rin Yokoyama, and Dr. Reiko Kojima for giving me opportunities to join the experiments and for their generous guidance. Prof. Shutato Hanai joined such experiments with me, whose presence remains irreplaceable for me.

My sincere thanks go to all members of the "Experimental Nuclear and Hadronic Physics" (NH) group at Kyoto University. I am indebted to Prof. Tomofumi Nagae, Prof. Megumi Naruki, Prof.Tstuya Murakami, Prof. Toshiyuki Gogami, Prof. Masahiro Dozono, and Prof. Natsuki Tomida for their advice from various perspectives. I also appreciate the students who, even without direct involvement in my research, made discussions and daily life enjoyable. I am especially grateful to Mr. Takeshi Harada for providing many enjoyable opportunities that enriched my research life.

I would like to thank the secretaries–Ms. Yuri Kimura at the NH group and Ms. Emiko Isogai and Ms. Mitsue Yamamoto at Uesaka laboratory in RIKEN–for their dedicated support, which allowed me to fully concentrate on my research.

I appreciate the support from the RIKEN Junior Research Associate Program and JSPS Research Fellowships for Young Scientists.

Finally but not least, I would like to express my deepest gratitude to my family, whose support has sustained me through this journey.

Appendix A

Data table

The experimental values of the differential cross sections for the proton elastic scattering from ^{132}Sn are summarized in the following table.

Table A.1: Differential cross sections for ^{132}Sn(p,p).

θ_{cm} [deg]	$d\sigma/d\Omega$ [mb/sr]	$\Delta(d\sigma/d\Omega)$ [mb/sr]
14	$1.909 \times 10^{+2}$	$0.105 \times 10^{+2}$
15	$1.950 \times 10^{+2}$	$0.103 \times 10^{+2}$
16	$1.576 \times 10^{+2}$	$0.082 \times 10^{+2}$
17	$1.052 \times 10^{+2}$	$0.055 \times 10^{+2}$
18	$5.716 \times 10^{+1}$	$0.309 \times 10^{+1}$
19	$2.563 \times 10^{+1}$	$0.157 \times 10^{+1}$
20	$1.229 \times 10^{+1}$	$0.087 \times 10^{+1}$
21	$1.007 \times 10^{+1}$	$0.075 \times 10^{+1}$
22	$1.447 \times 10^{+1}$	$0.097 \times 10^{+1}$
23	$1.668 \times 10^{+1}$	$0.107 \times 10^{+1}$
24	$1.756 \times 10^{+1}$	$0.111 \times 10^{+1}$
25	$1.496 \times 10^{+1}$	$0.096 \times 10^{+1}$
26	$1.173 \times 10^{+1}$	$0.079 \times 10^{+1}$
27	$7.161 \times 10^{+0}$	$0.544 \times 10^{+0}$
28	$4.416 \times 10^{+0}$	$0.385 \times 10^{+0}$
29	$3.792 \times 10^{+0}$	$0.350 \times 10^{+0}$
30	$2.564 \times 10^{+0}$	$0.271 \times 10^{+0}$
31	$2.275 \times 10^{+0}$	$0,256 \times 10^{+0}$
32	$2.012 \times 10^{+0}$	$0.238 \times 10^{+0}$
33	$1.794 \times 10^{+0}$	$0.217 \times 10^{+0}$
34	$1.397 \times 10^{+0}$	$0.190 \times 10^{+0}$
35	$1.138 \times 10^{+0}$	$0.176 \times 10^{+0}$
36	$1.230 \times 10^{+0}$	$0.184 \times 10^{+0}$
37	8.310×10^{-1}	1.494×10^{-1}
38	9.160×10^{-1}	1.542×10^{-1}

Appendix B

RDC Tracking

B.1 Drift length correction

The drift length of RDC was obtained from the TDC distributions using the stc functions. The trajectory was determined by minimizing the χ^2 value, defined as

$$\chi^2 = \sum_i \left(\frac{f(z_i) - x_i}{1 + A^2} - dl_i \right)^2, \tag{B.1}$$

$$f(z) = X + Az. \tag{B.2}$$

However, the position dependences remained in the residuals $\frac{f(z_i)-x_i}{1+A^2} - dl_i$, as shown in Fig. B.1. To reduce the residuals, we corrected the drift length DT as

$$DT \to DT + f(DT), \tag{B.3}$$

$$f(x) = (p_0 + p_1 x + p_2 x^2)(x + 7)x(x - 7), \tag{B.4}$$

where parameters p_i were calibrated by fitting the 2D spectra of the residuals versus the drift lengths. This correction was iteratively performed until no further improvement was observed. Figure B.2 shows the residuals after each iteration.

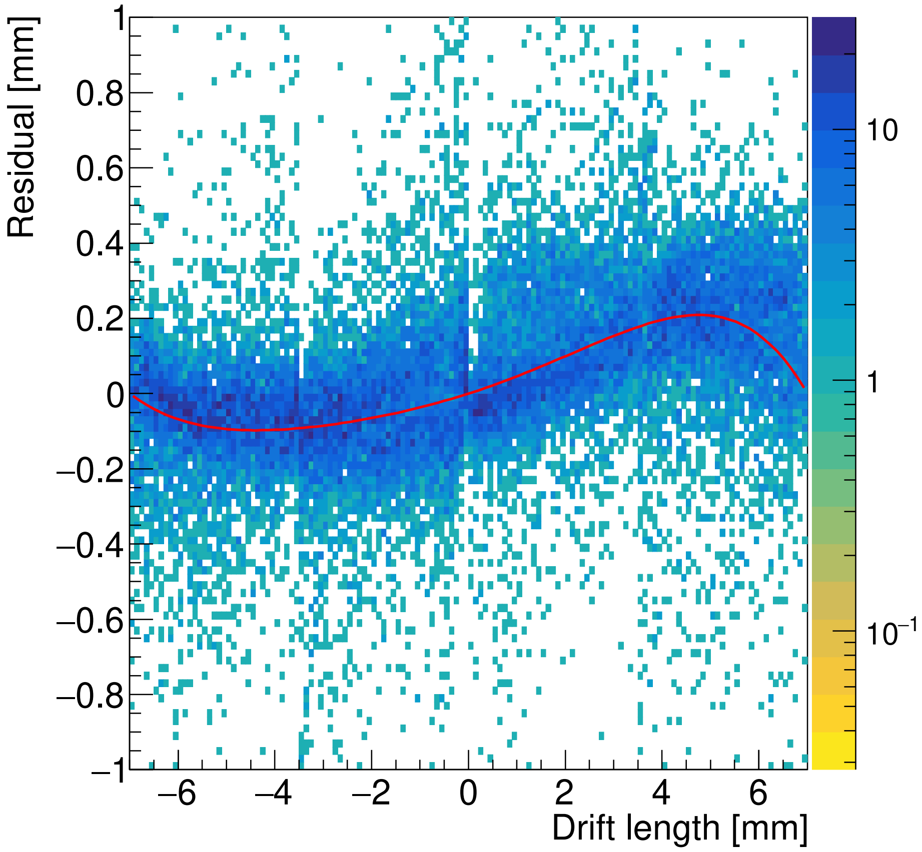

Figure B.1: The correlation between the drift length and residual for the X3 plane before correcting the drift length.

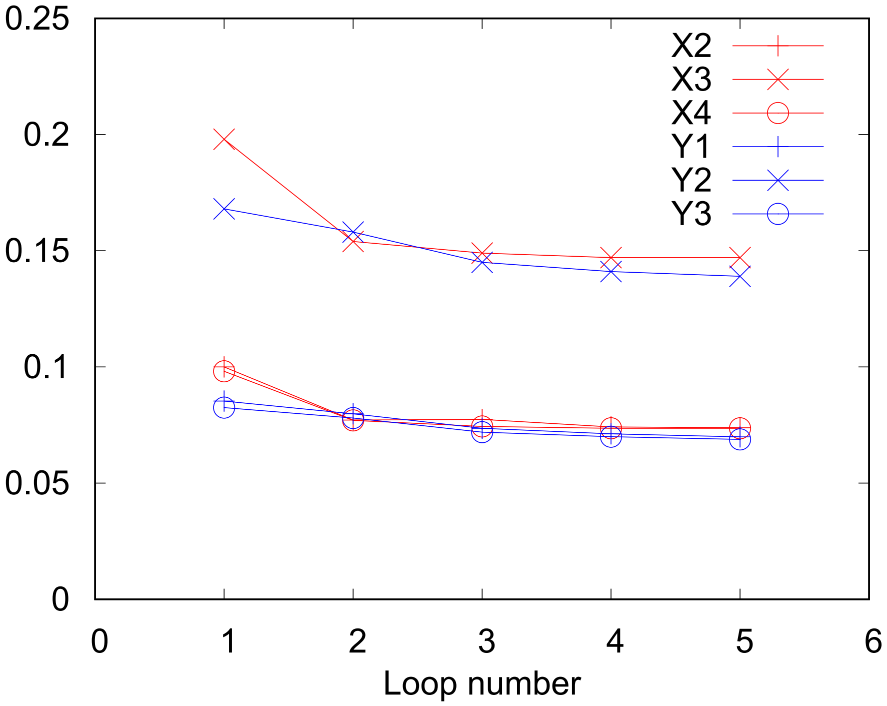

Figure B.2: The residuals after each iteration.

Appendix C

Data reduction for ^{48}Ca

In this appendix, the analysis of ^{48}Ca data is described. Since the procedure for ^{48}Ca was almost the same as that for ^{132}Sn, we present only the results and the difference in the methods.

C.1 Beam analysis

The ^{48}Ca beam was also produced by bombarding the primary ^{238}U beam on the ^{9}Be target.

Figures C.1, C.2, and C.3 present the resulting PID plot, the beam energy distribution, and the beam profile on the SHT for the ^{48}Ca beam, respectively.

C.2 Recoil proton analysis

The recoil particle PID and energy calibration for the ^{48}Ca data were basically performed with the same functions or parameters as the ^{132}Sn data. However, the TOF between the F12pla and $p\Delta E$ was corrected because the timing of the F12pla was affected by the time walk. The correction was performed based on the correlation plots between the TOF and the charge of $p\Delta E$ as shown in Figs. C.4. By selecting the range of $300 < Q_{p\Delta E} < 400$, projecting the spectra onto the x-axis, and comparing the positions of the peaks around $t_{p\Delta E} - t_{12} = 50\,\mathrm{ns}$, as shown in Figs. C.5, the timing correction was determined.

C.3 Excitation energy and count of elastic events

By the same procedure for the ^{132}Sn data, we reconstructed the excitation energies. Figures C.6 show the correlations between the excitation energies E_x and the scattering angle θ_{cm}. The excitation energies using the NaI(Tl) calorimeters are shifted to higher values. This is because the energy calibration was performed without correcting for the position dependence of the NaI(Tl) calorimeters. The black solid lines in Fig. C.6a represent the averaged upper and lower boundaries of the elastic region. This region sufficiently covers

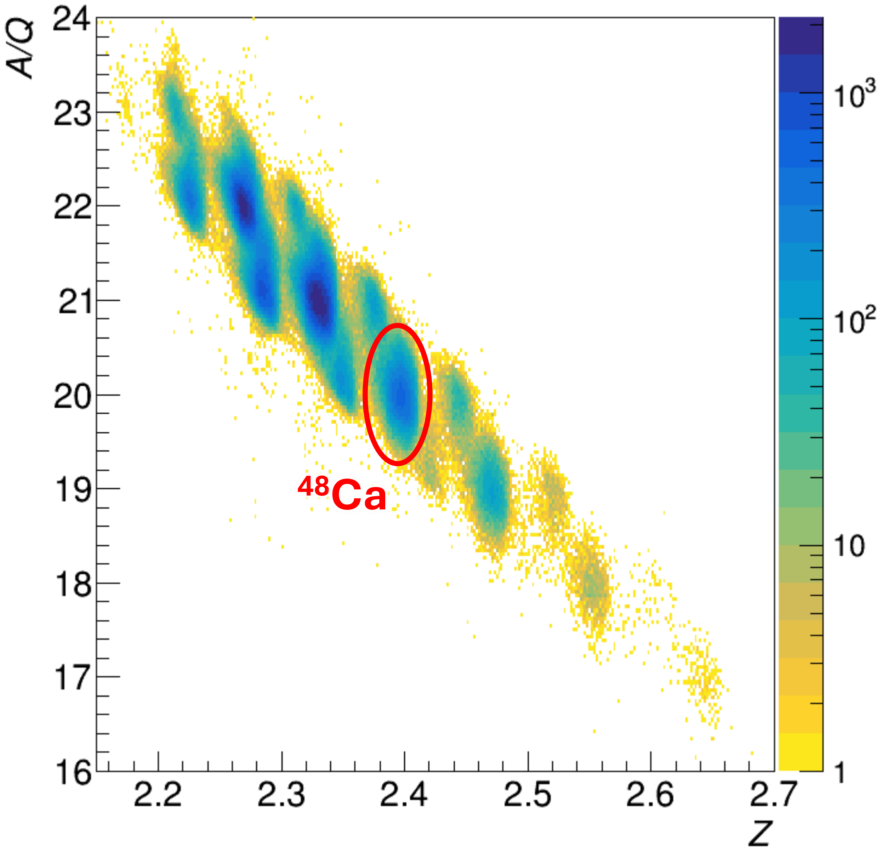

Figure C.1: Beam PID spectrum: 2D hisgram of A/Q versus Z for ^{48}Ca setting.

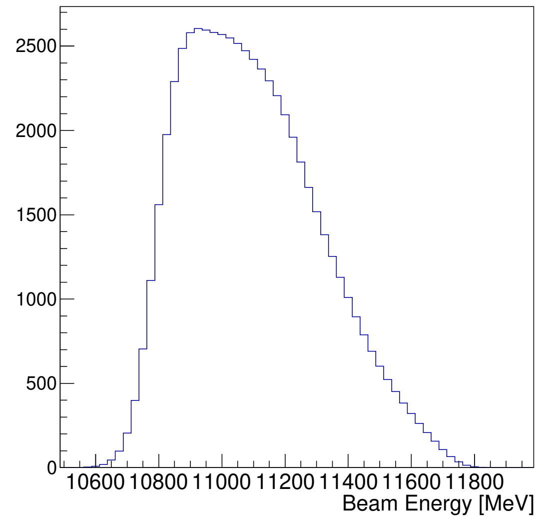

Figure C.2: Beam energy distriubtion of ^{48}Ca on the SHT.

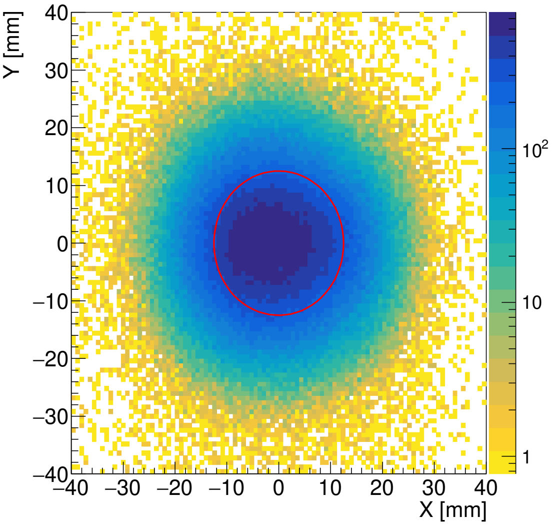

Figure C.3: Beam profile on the target.

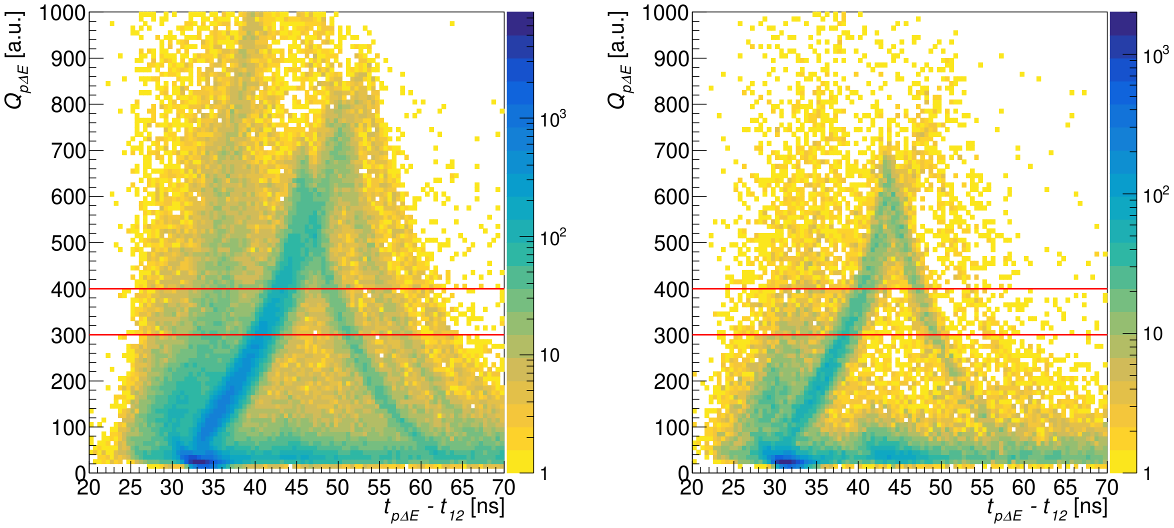

(a) ^{48}Ca

(b) ^{132}Sn

Figure C.4: PID plots for recoil particles using $t_{p\Delta E} - t_{12}$ and $Q_{p\Delta E}$.

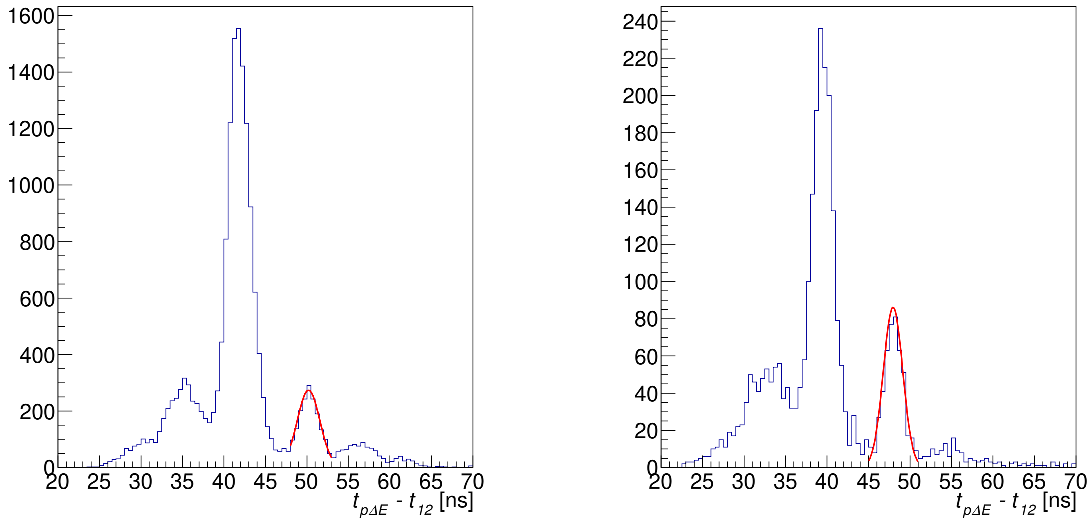

(a) ^{48}Ca (b) ^{132}Sn

Figure C.5: $t_{p\Delta E} - t_{12}$ spectra with the gate of $300 < Q_{p\Delta E} < 400$.

the elastic peak and is well separated from the first excited state at 3.83 MeV. Therefore, the elastic yield is considered to be unaffected by the peak shift.

Figure C.7 shows the distribution of the obtained yields.

C.4 Derivation of differential cross section

The differentail cross sections for ^{48}Ca were calculated using Eq. 3.31. The values used for evaluating ϵ_0 and I_{beam} are summarized in Tables C.1 and C.2, respectively. N_{tgt} is assumed to be 6.76×10^{21}, which corresponds to a $\sqrt{2} \times 1$ mm-thick solod hydrogen.

Table C.1: Values of angle-independent efficiency ϵ_0 and its components for ^{48}Ca setting.

BLDs at F12	71.2%
Detecros at BigRIPS	77.5%
DAQ	78.2%
Angle-independent efficiency ϵ_0	43.2%

Figure C.8 shows the angular distribution of the obtained cross sections. By using this distribution, the target number N_{tgt} was evaluated.

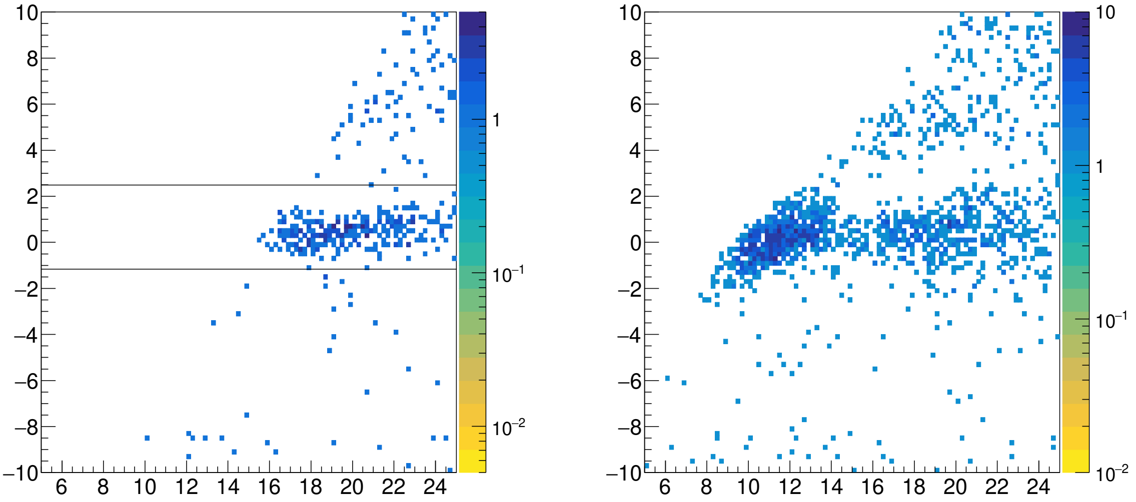

(a) NaI.

(b) TOF.

Figure C.6: Angular dependence of the excitation energy for ^{48}Ca. The solid lines represent the averaged upper and lower boundaries of the elastic region.

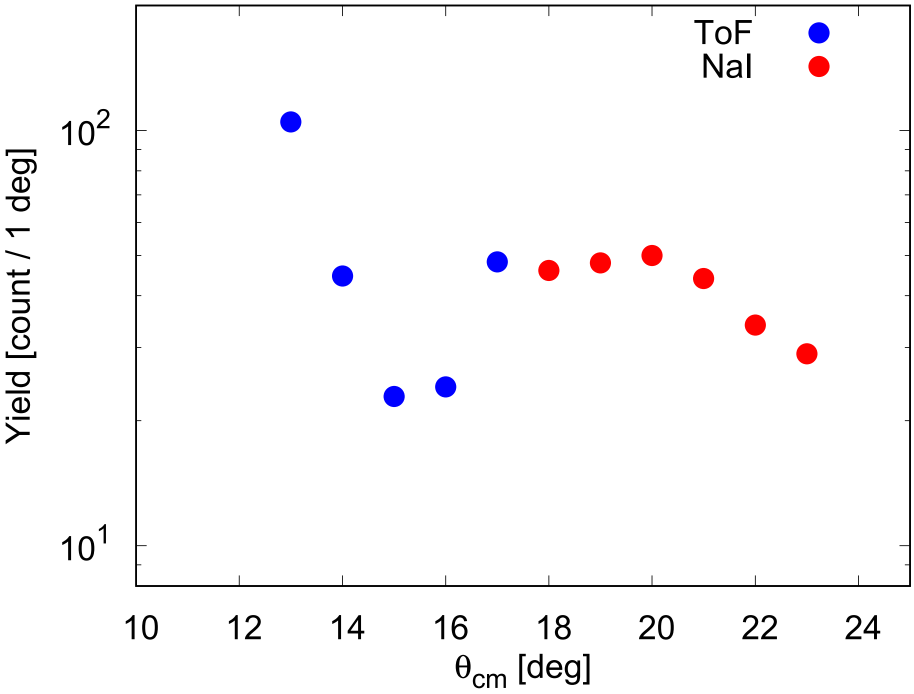

Figure C.7: Angular dependence of elastic yields. The blue and red points are data using TOF and NaI(Tl) for proton energies, respectively.

Table C.2: Number of beam particles (I_{beam}) and values for its calculation for ^{48}Ca.

Counts of F7Dia	1.19×10^{10} [particle]
Scaler count loss	0.69%
Target hit rate	48.1%
Purity of ^{48}Ca	8.74%
Number of beam praticles (I_{beam})	5.05×10^{8} [particle]

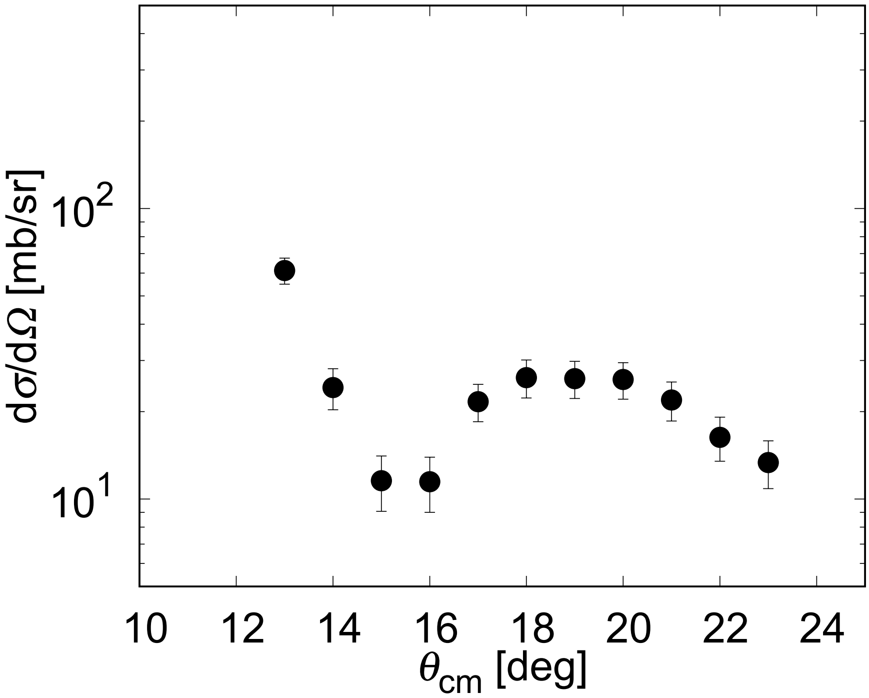

Figure C.8: Obtained differential cross sections for proton elastic scattering from ^{48}Ca.

Appendix D

Global Dirac optical potential

In 1980, Hama, *et al.* presented phenomenological global Dirac optical potential (GDOP) model fits to proton elastic scattering from heavy nuclei (^{40,48}Ca, ^{56}Fi, ^{60}Ni, ^{90}Zr, and ^{208}Pb) at energies between 65 to 1040 MeV. The GDOP calculations reasonably reproduce observables of the proton elastic scattering. In 1993, extended GDOP models were presented that fitted the data from nuclei ranging from ^{12}C to ^{208}Pb, and in 2009, further developments were reported with fits to the data from ^{4}H to ^{208}Pb. The GDOP formulations include energy-dependent and mass-number-dependent terms. Alongside these extensions, refinements of the model were also introduced. Depending on the fitting strategy and model formulation, the 1993 work provided three different calculations, while the 2009 study presented two. In the following, we show the comparisons of the present experimental results with these GDOP calculations.

Figure D.1 shows the Rutherford ratios of the GOOP calculations. The solid and dashed lines are calculations fit to the data from nuclei ranging from ^{12}C to ^{208}Pb and from ^{4}He to ^{208}Pb, respectively. In the main text, we show the calculation of fit 1 with ^{12}C to ^{208}Pb data as the GDOP calculation. The dashed lines deviate from the experimental results at two valleys around $\theta_{\mathrm{cm}} = 20^\circ$ and $\theta_{\mathrm{cm}} = 30^\circ$. No calculations well reproduce the peak height at $\theta_{\mathrm{cm}} = 15^\circ$. These calculations used only the data of stable nuclei for the parameter fit and do not include the explicit isospin-dependent term. Our results imply that a new GDOP model, including such a term, is needed to explain proton elastic scattering from unstable nuclei.

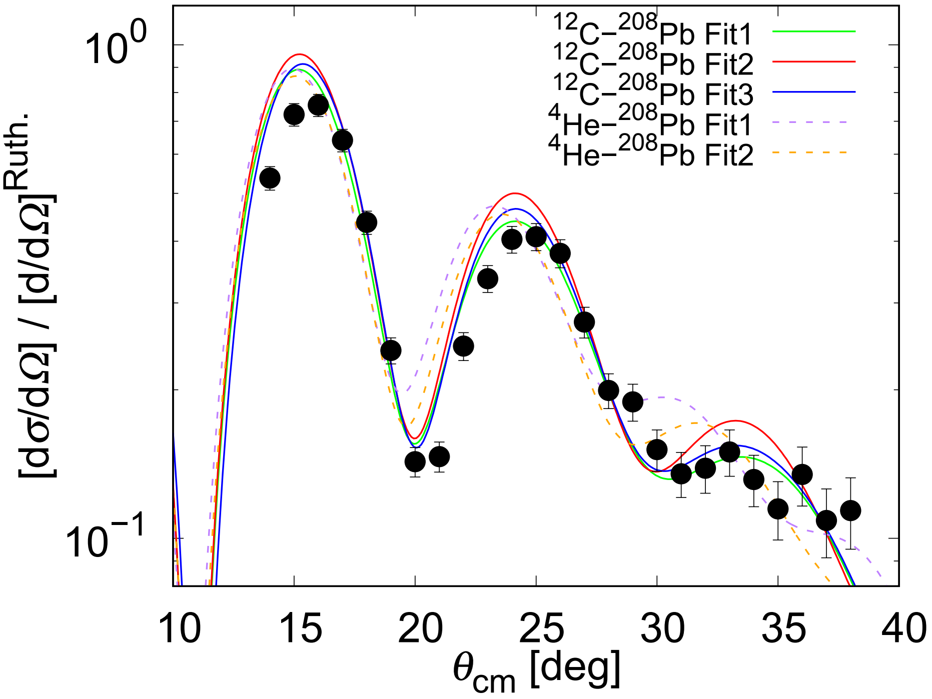

Figure D.1: Differential cross sections divided by the Rutherford cross section. The solid and dashed lines are calculations fit to the data from nuclei ranging from ^{12}C to ^{208}Pb and from ^{4}He to ^{208}Pb, respectively.

Bibliography

[1] Umesh Garg and Gianluca Colò, Progress in Particle and Nuclear Physics, **101**, 55–95 (2018).

[2] C. Fuchs and H. H. Wolter, The European Physical Journal A - Hadrons and Nuclei, **30**(1), 5–21 (2006).

[3] B. P. Abbott et al., Phys. Rev. Lett., **119**, 161101 (2017).

[4] M. Oertel, M. Hempel, T. Klähn, and S. Typel, Rev. Mod. Phys., **89**, 015007 (2017).

[5] Lie-Wen Chen, Che Ming Ko, and Bao-An Li, Phys. Rev. C, **72**, 064309 (2005).

[6] Andrea Carbone, Gianluca Colò, Angela Bracco, Li-Gang Cao, Pier Francesco Bortignon, Franco Camera, and Oliver Wieland, Phys. Rev. C, **81**, 041301 (2010).

[7] S. Abrahamyan et al., Phys. Rev. Lett., **108**, 112502 (2012).

[8] D. Adhikari et al., Phys. Rev. Lett., **126**, 172502 (2021).

[9] A. Krasznahorkay, A. Balanda, J.A. Bordewijk, S. Brandenburg, M.N. Harakeh, N. Kalantar-Nayestanaki, B.M. Nyakó, J. Timár, and A. van der Woude, Nuclear Physics A, **567**(3), 521–540 (1994).

[10] A. Tamii et al., Phys. Rev. Lett., **107**, 062502 (2011).

[11] A. Klimkiewicz et al., Phys. Rev. C, **76**, 051603 (2007).

[12] A. Trzcińska, J. Jastrzębski, P. Lubiński, F. J. Hartmann, R. Schmidt, T. von Egidy, and B. Kłos, Phys. Rev. Lett., **87**, 082501 (2001).

[13] B. Kłos et al., Phys. Rev. C, **76**, 014311 (2007).

[14] B. Alex Brown, G. Shen, G. C. Hillhouse, J. Meng, and A. Trzcińska, Phys. Rev. C, **76**, 034305 (2007).

[15] C. M. Tarbert et al., Phys. Rev. Lett., **112**, 242502 (2014).

[16] G. W. Hoffmann et al., Phys. Rev. C, **21**, 1488–1494 (1980).

[17] V. E. Starodubsky and N. M. Hintz, Phys. Rev. C, **49**, 2118–2135 (1994).

[18] J. Zenihiro et al., Phys. Rev. C, **82**, 044611 (2010).

[19] A. Huck, G. Klotz, A. Knipper, C. Miehé, C. Richard-Serre, G. Walter, A. Poves, H. L. Ravn, and G. Marguier, Phys. Rev. C, **31**, 2226–2237 (1985).

[20] D. Steppenbeck et al., Nature, **502**(7470), 207–210 (2013).

[21] S. Yoshida, H. Sagawa, J. Zenihiro, and T. Uesaka, Phys. Rev. C, **102**, 064307 (2020).

[22] Juzo Zenihiro, Tomohiro Uesaka, Hiroyuki Sagawa, and Satoshi Yoshida, Progress of Theoretical and Experimental Physics, **2021**(2), 023D05 (2021).

[23] X. Roca-Maza, M. Brenna, B. K. Agrawal, P. F. Bortignon, G. Colò, Li-Gang Cao, N. Paar, and D. Vretenar, Phys. Rev. C, **87**, 034301 (2013).

[24] J. Zenihiro et al., Direct determination of the neutron skin thicknesses in ^{40,48}ca from proton elastic scattering at $e_p = 295$ mev (2018), arXiv:1810.11796.

[25] Beat Hahn, D. G. Ravenhall, and Robert Hofstadter, Phys. Rev., **101**, 1131–1142 (1956).

[26] H. De Vries, C.W. De Jager, and C. De Vries, Atomic Data and Nuclear Data Tables, **36**(3), 495–536 (1987).

[27] I. Angeli and K.P. Marinova, Atomic Data and Nuclear Data Tables, **99**(1), 69–95 (2013).

[28] D. Adhikari et al., Phys. Rev. Lett., **129**, 042501 (2022).

[29] S. Terashima et al., Phys. Rev. C, **77**, 024317 (2008).

[30] H. J. Gils, H. Rebel, and E. Friedman, Phys. Rev. C, **29**, 1295–1306 (1984).

[31] B.M. Barnett et al., Physics Letters B, **156**(3), 172–176 (1985).

[32] C. A. Bertulani and C. De Conti, Phys. Rev. C, **81**, 064603 (2010).

[33] L. Ray, Phys. Rev. C, **19**, 1855–1872 (1979).

[34] A. N. Antonov, D. N. Kadrev, M. K. Gaidarov, E. Moya de Guerra, P. Sarriguren, J. M. Udias, V. K. Lukyanov, E. V. Zemlyanaya, and G. Z. Krumova, Phys. Rev. C, **72**, 044307 (2005).

[35] F. Le Blanc et al., Phys. Rev. C, **72**, 034305 (2005).

[36] K. Tsukada et al., Phys. Rev. Lett., **131**, 092502 (2023).

[37] T. Yamaguchi, I. Hachiuma, A. Kitagawa, K. Namihira, S. Sato, T. Suzuki, I. Tanihata, and M. Fukuda, Phys. Rev. Lett., **107**, 032502 (2011).

[38] S. Terashima et al., Progress of Theoretical and Experimental Physics, **2014**(10), 101D02 (2014).

[39] M. Tanaka et al., Phys. Rev. C, **106**, 014617 (2022).

[40] I. Tanihata, H. Hamagaki, O. Hashimoto, Y. Shida, N. Yoshikawa, K. Sugimoto, O. Yamakawa, T. Kobayashi, and N. Takahashi, Phys. Rev. Lett., **55**, 2676–2679 (1985).

[41] R3B Collaboration et al., Acta Physica Polonica B, Proceedings Supplement, **17**(3), 3–A18, Funding Information: The project was supported by the BMBF via Project No. 05P21RDFN2, the Helmholtz Research Academy Hessen for FAIR and the GSI-TU Darm-stadt cooperation. Publisher Copyright: © 2024 Jagiellonian University. (2024).

[42] R. F. Garcia Ruiz et al., Nature Physics, **12**(6), 594–598 (2016).

[43] M. Tanaka et al., Phys. Rev. Lett., **124**, 102501 (2020).

[44] S.R. Neumaier et al., Nuclear Physics A, **712**(3), 247–268 (2002).

[45] A.V. Dobrovolsky et al., Nuclear Physics A, **766**, 1–24 (2006).

[46] S. Ilieva et al., Nuclear Physics A, **875**, 8–28 (2012).

[47] G.A. Korolev et al., Physics Letters B, **780**, 200–204 (2018).

[48] A.V. Dobrovolsky et al., Nuclear Physics A, **1008**, 122154 (2021).

[49] M. von Schmid et al., The European Physical Journal A, **59**(4), 83 (2023).

[50] K. Yue et al., Phys. Rev. C, **100**, 054609 (2019).

[51] J. T. Zhang et al., Phys. Rev. C, **108**, 014614 (2023).

[52] Y. Matsuda et al., Nuclear Instruments and Methods in Physics Research Section A: Accelerators, Spectrometers, Detectors and Associated Equipment, **643**(1), 6–10 (2011).

[53] S Chebotaryov et al., Progress of Theoretical and Experimental Physics, **2018**(5), 053D01 (2018).

[54] Y. Matsuda et al., Phys. Rev. C, **87**, 034614 (2013).

[55] H. Sakaguchi and J. Zenihiro, Progress in Particle and Nuclear Physics, **97**, 1–52 (2017).

[56] J. Piekarewicz, Phys. Rev. C, **73**, 044325 (2006).

[57] P. Arthuis, C. Barbieri, M. Vorabbi, and P. Finelli, Phys. Rev. Lett., **125**(18), 182501 (2020).

[58] T. Miyagi, S. R. Stroberg, P. Navrátil, K. Hebeler, and J. D. Holt, Phys. Rev. C, **105**(1), 014302 (2022).

[59] Baishan Hu et al., Nat. Phys., **18**(10), 1196–1200 (2022).

[60] P. Arthuis, K. Hebeler, and A. Schwenk, Neutron-rich nuclei and neutron skins from chiral low-resolution interactions (2024), arXiv:2401.06675.

[61] H. Okuno, N. Fukunishi, and O. Kamigaito, Progress of Theoretical and Experimental Physics, **2012**(1), 03C002 (2012).

[62] Chihiro Iwamoto et al., Progress of Theoretical and Experimental Physics, **2023**(8), 083H01 (2023).

[63] RIKEN, Facilities at the ribf, `https://www.nishina.riken.jp/facility/RIBFfacility_e.html` (), Accessed on Jan. 28, 2026.

[64] Toshiyuki Kubo, Nuclear Instruments and Methods in Physics Research Section B: Beam Interactions with Materials and Atoms, **204**, 97–113, 14th International Conference on Electromagnetic Isotope Separators and Techniques Related to their Applications (2003).

[65] H. Kumagai, A. Ozawa, N. Fukuda, K. Sümmerer, and I. Tanihata, Nuclear Instruments and Methods in Physics Research Section A: Accelerators, Spectrometers, Detectors and Associated Equipment, **470**(3), 562–570 (2001).

[66] N. Fukuda, T. Kubo, T. Ohnishi, N. Inabe, H. Takeda, D. Kameda, and H. Suzuki, Nuclear Instruments and Methods in Physics Research Section B: Beam Interactions with Materials and Atoms, **317**, 323–332, XVIth International Conference on ElectroMagnetic Isotope Separators and Techniques Related to their Applications, December 2–7, 2012 at Matsue, Japan (2013).

[67] S. Ota et al., RIKEN Accel. Prog. Rep., **49**, 15 (2016).

[68] RIKEN, Bigrips technical information, `https://ribf.riken.jp/BigRIPSInfo/` (), Accessed on Jan. 28, 2026.

[69] H. Miya et al., Nuclear Instruments and Methods in Physics Research Section B: Beam Interactions with Materials and Atoms, **317**, 701–704, XVIth International Conference on ElectroMagnetic Isotope Separators and Techniques Related to their Applications, December 2–7, 2012 at Matsue, Japan (2013).

[70] Y. Matsuda, J. Zenihiro, W. Chao, H. Sakaguchi, J. Tanaka, M. Tsumura, and Nakatsuka. N., RIKEN Accel. Prog. Rep., **48**, 211 (2015).

[71] Y. Matsuda, J. Zenihiro, S. Terashima, and H. Sakaguchi, RIKEN Accel. Prog. Rep., **49**, 170 (2016).

[72] J. Zenihiro, Y. Matsuda, H. Sakaguchi, H. Takeda, Y. Iwao, H. Matsumoto, and M. Itoh, CYRIC annual report, **2005**, 20–26 (2005).

[73] H. Baba, T. Ichihara, T. Ohnishi, S. Takeuchi, K. Yoshida, Y. Watanabe, S. Ota, and S. Shimoura, Nuclear Instruments and Methods in Physics Research Section A: Accelerators, Spectrometers, Detectors and Associated Equipment, **616**(1), 65–68 (2010).

[74] H. Baba, T. Ichihara, T. Ohnishi, K. Yoshida, Y. Watanabe, S. Ota, S. Shimoura, S. Takeuchi, and Y. Togano, RIKEN Accel. Prog. Rep., **48**, 25 (2016).

[75] H. Baba et al., IEEE Transactions on Nuclear Science, **68**(8), 1841–1848 (2021).

[76] H. Baba, T. Ichihara, T. Ohnishi, S. Takeuchi, K. Yoshida, Y. Watanabe, S. Ota, S. Shimoura, and K. Yoshinaga, Nuclear Instruments and Methods in Physics Research Section A: Accelerators, Spectrometers, Detectors and Associated Equipment, **777**, 75–79 (2015).

[77] H. Baba, T. Ichihara, T. Ohnishi, S. Takeuchi, K. Yoshida, Y. Watanabe, S. Ota, and S. Shimoura, RIKEN Accel. Prog. Rep., **44**, 213 (2011).

[78] O.B. Tarasov and D. Bazin, Nuclear Physics A, **746**, 411–414, Proceedings of the Sixth International Conference on Radioactive Nuclear Beams (RNB6) (2004).

[79] Y. Matsuda, H. Sakaguchi, H. Takeda, S. Terashima, J. Zenihito, M. Itoh, K. Ozeki, and T. Kobayashi, CYRIC annual report, **2006**, 15–27 (2006).

[80] C.A. Goulding and J.G. Rogers, Nuclear Instruments and Methods, **153**(2), 511–515 (1978).

[81] A.M. Sourkes, M.S. de Jong, C.A. Goulding, W.T.H. van Oers, E.A. Ginkel, R.F. Carlson, A.J. Cox, and D.J. Margaziotis, Nuclear Instruments and Methods, **143**(3), 589–594 (1977).

[82] C. J. Horowitz, Phys. Rev. C, **31**, 1340–1348 (1985).

[83] D. P. Murdock and C. J. Horowitz, Phys. Rev. C, **35**, 1442–1462 (1987).

[84] D. P. Murdock and C. J. Horowitz, Phys. Rev. C, **35**, 1442–1462 (1987).

[85] J. R. Shepard, J. A. McNeil, and S. J. Wallace, Phys. Rev. Lett., **50**, 1443–1446 (1983).

[86] C.J. Horowitz and Brian D. Serot, Nuclear Physics A, **464**(4), 613–699 (1987).

[87] H. Sakaguchi et al., Phys. Rev. C, **57**, 1749–1755 (1998).

[88] R. G. Sachs, Phys. Rev., **126**, 2256–2260 (1962).

[89] C. J. Horowitz and J. Piekarewicz, Phys. Rev. C, **86**, 045503 (2012).

[90] Peter J. Mohr, David B. Newell, Barry N. Taylor, and Eite Tiesinga, Rev. Mod. Phys., **97**, 025002 (2025).

[91] S. Navas et al., Phys. Rev. D, **110**, 030001 (2024).

[92] C.J. Horowitz and Brian D. Serot, Physics Letters B, **140**(3), 181–186 (1984).

[93] Akihiro Haga, Setsuo Tamenaga, Hiroshi Toki, and Yataro Horikawa, Phys. Rev. C, **70**, 064322 (2004).

[94] S. Shim, B. C. Clark, S. Hama, E. D. Cooper, R. L. Mercer, L. Ray, and G. W. Hoffmann, Phys. Rev. C, **38**, 1968–1970 (1988).

[95] Tetsuo Hatsuda and Su Houng Lee, Phys. Rev. C, **46**, R34–R38 (1992).

[96] L. Ray, G. W. Hoffmann, G. S. Blanpied, W. R. Coker, and R. P. Liljestrand, Phys. Rev. C, **18**, 1756–1760 (1978).

[97] L. Ray, W. Rory Coker, and G. W. Hoffmann, Phys. Rev. C, **18**, 2641–2655 (1978).

[98] F. Hofmann, C. M. Keil, and H. Lenske, Phys. Rev. C, **64**, 034314 (2001).

[99] H. Takeda, Memoirs of the Faculty of Science, Kyoto University. Series of physics, astrophysics, geophysics and chemistry, **44** (2003).

[100] Z. P. Li, G. C. Hillhouse, and J. Meng, Phys. Rev. C, **78**, 014603 (2008).

[101] H. Hergert, S.K. Bogner, T.D. Morris, A. Schwenk, and K. Tsukiyama, Phys. Rep., **621**, 165–222 (2016).

[102] A. Ekström, G. R. Jansen, K. A. Wendt, G. Hagen, T. Papenbrock, B. D. Carlsson, C. Forssén, M. Hjorth-Jensen, P. Navrátil, and W. Nazarewicz, Phys. Rev. C, **91**, 051301 (2015).

[103] W. G. Jiang, A. Ekström, C. Forssén, G. Hagen, G. R. Jansen, and T. Papenbrock, Phys. Rev. C, **102**, 054301 (2020).

[104] E. D. Cooper, S. Hama, B. C. Clark, and R. L. Mercer, Phys. Rev. C, **47**, 297–311 (1993).

[105] E. D. Cooper, S. Hama, and B. C. Clark, Phys. Rev. C, **80**, 034605 (2009).

[106] E. Chabanat, P. Bonche, P. Haensel, J. Meyer, and R. Schaeffer, Nuclear Physics A, **635**(1), 231–256 (1998).

[107] X. Roca-Maza, G. Colò, and H. Sagawa, Phys. Rev. C, **86**, 031306 (2012).

[108] Nguyen Van Giai and H. Sagawa, Physics Letters B, **106**(5), 379–382 (1981).

[109] J. Bartel, P. Quentin, M. Brack, C. Guet, and H.-B. Håkansson, Nuclear Physics A, **386**(1), 79–100 (1982).

[110] S. Goriely, M. Samyn, J.M. Pearson, and M. Onsi, Nuclear Physics A, **750**(2), 425–443 (2005).

[111] M. Kortelainen, T. Lesinski, J. Moré, W. Nazarewicz, J. Sarich, N. Schunck, M. V. Stoitsov, and S. Wild, Phys. Rev. C, **82**, 024313 (2010).

[112] M. Kortelainen, J. McDonnell, W. Nazarewicz, P.-G. Reinhard, J. Sarich, N. Schunck, M. V. Stoitsov, and S. M. Wild, Phys. Rev. C, **85**, 024304 (2012).

[113] M. Kortelainen et al., Phys. Rev. C, **89**, 054314 (2014).

[114] G. A. Lalazissis, J. König, and P. Ring, Phys. Rev. C, **55**, 540–543 (1997).

[115] B. G. Todd-Rutel and J. Piekarewicz, Phys. Rev. Lett., **95**, 122501 (2005).

[116] F. P. Gustafsson et al., Physical Review Letters, **135**(22) (2025).

[117] J. Zenihiro et al., RIKEN Accel. Prog. Rep., **53**, 44 (2020).

[118] A. Sommerfeld, Zeitschrift für Physik, **47**(1), 1–32 (1928).

List of Tables

List of Figures